Improving the Efficiencies of Metal-Insulator-Semiconductor (MIS) Photoelectrodes with Interfacial Design

by

Joseph Quinn

A dissertation submitted in partial fulfillment
of the requirements for the degree of
Doctor of Philosophy
(Chemical Engineering)
in the University of Michigan
2020

Doctoral Committee:

Professor Suljo Linic, Chair
Assistant Professor Bryan Goldsmith
Professor Stephen Maldonado
Assistant Professor Nirala Singh

Joseph P. Quinn

jpq@umich.edu

ORCID iD: 0000-0002-8742-7052

Dedication

To Mom, Dad, MK, Nellie, Jack, and Jenn who I added.

Acknowledgements

I would like to express my heartfelt thanks to all those who helped me make this dissertation possible. My parents for all their love and support during these 20+ years of education and for encouraging my interest in science and engineering. My siblings MK, Nellie, and Jack who are always there when I need them. I'd also like to thank my fiancé Dr. Jenn Jocz and the Jocz family. Thanks, Jenn, for being at my side in the peaks and the troughs, and I'm so glad I chose Michigan.

Thank you group members old and new. I'd particularly like to thank Paul who helped teach me ropes on a project with Steven, Valentina who came in with me and made it the full mile, and John who I've worked with the past 3 years and has greatly contributed to this work. I'd also like to give a special thanks to my advisor Prof Suljo Linic who enabled me to pursue research directions I found most interesting and whose insights were critical to the success of the work.

I'd like to thank the friends I've made throughout this journey. Thank you Phil, Martin, David, Genesis, and Kathy for keeping me sane through the end grad school. There are so many more to thank, but I'm starting to hear the music play me off, so I'll have end it here. Either that or I actually have gone crazy, which is a possibility considering I wrote these acknowledgements last.

Table of Contents

List of Figures

Abstract

Photoelectrochemical systems have the potential to sustainably convert solar energy into chemical energy by splitting water into its constitutive hydrogen and oxygen components. One common photoelectrode system involves the use of a metal-insulator-semiconductor (MIS) structure. An efficient MIS photoelectrode uses a semiconductor with an ideal band gap to absorb sunlight, a metallic catalyst with high electrocatalytic activity, and a stable insulator which prevents the degradation of the otherwise unstable semiconducting material. The amount of photovoltage generated by the system is highly dependent on the physical characteristics of the interface. Conventionally, photovoltage has been optimized by maximizing the "barrier height" (interfacial electric field) of the system, while minimizing the thickness of the insulator to reduce resistance. This approach requires the use of high work function metals for photoanodes and low work function metals for photocathodes in order to maximize the barrier height. This greatly limits the number of viable materials in MIS systems since the metal layers must also possess high electrocatalytic activity and stability.

This work shows that the tuning of insulator thickness can be leveraged to allow systems that suffer from moderate barrier heights to achieve high photovoltages. This was done by designing insulators that minimize the semiconductor-to-metal interfacial flux of majority charge carriers (leading to recombination), without creating an overly large impediment for the flux of minority carriers needed to drive the reaction. The effect was demonstrated experimentally with a photoanode consisting of n-type silicon, a hafnium oxide insulator, and a Ni electrocatalyst. This result shows that metals with non-ideal work function properties but optimal electrocatalytic

activity can still achieve high photovoltages and greatly increases the number of viable materials for use in MIS systems.

Another strategy that has expanded the phase space of viable materials for MIS systems involves the introduction of bilayer metals. This approach uses one metal layer to set the barrier height of the system, and another metal layer to provide stable electrocatalytic sites. In this work bilayer metal MIS systems were used to examine (1) how insulator thickness tuning affects various barrier height systems, and (2) the potential additive benefits of a design approach that combines insulator thickness tuning with bilayer metals. This was demonstrated experimentally using pSi-HfO_2-Al-Pt and pSi-HfO_2-Ti-Pt photocathode systems. The relevant interfacial mechanisms were captured using a comprehensive model that can be used to predict MIS performance.

Chapter 1

Background and Motivation

1.1 Hydrogen Production in Photoelectrochemical Systems

A global reduction in greenhouse gas emissions is critical to mitigate the effects of climate change[1]. Figure 1.1 shows that US emissions can be roughly divided into three categories: industry, electrical generation, and transportation.

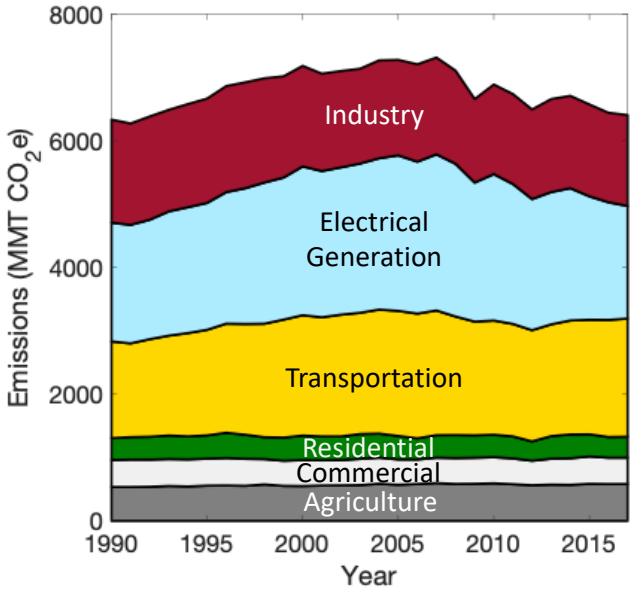

Figure 1.1 | US emissions of CO_2 equivalents from 1990-2016. These emissions are generated by various sources including industry, electrical generation, transportation, residential, commercial, and agriculture.[1]

Most renewable energy technologies are tailored toward reducing emissions in one of these specific sectors. For example, wind and solar power can reduce emissions in electrical generation, and battery-electric vehicles can reduce emissions for transportation. A renewable energy

technology that could potentially reduce emissions in all of these categories would be the generation of clean, renewable hydrogen. In the chemical industry molecular hydrogen is an important chemical reagent in numerous industrial processes including hydrocracking, the Haber-Bosch process, and the Fischer-Tropsch process. Today the ~10 million tons of hydrogen produced annually in the US[2] is created from conventional methods such as steam reforming, partial oxidation, and the water-gas shift, all of which generate CO_2 as a byproduct. A cheap, clean source of hydrogen could benefit the chemical industry by reducing emissions for the processes listed above and could also introduce new chemical processes such as CO_2 hydrogenation (capturing CO_2 to make chemical products). Hydrogen could also benefit electricity generation as a form of large-scale energy storage[3]. Lastly, a clean source of hydrogen could also reduce emissions in the transportation sector by generating fuel for hydrogen fuel cell vehicles[4], which have a non-carbon, H_2O exhaust.

One method that could lead a clean route to hydrogen generation is electrolysis, where a voltage is applied to electrodes in solution to split water into its constitutive hydrogen and oxygen components.[3,5] Though this process has been around for centuries virtually no hydrogen today is produced industrially from electrolysis. A primary reason for this is that electrolysis is very energetically demanding. Thermodynamically, it requires −1.23V to split water given the half reactions listed below:

		Voltage vs RHE (Reversible Hydrogen Electrode)
Hydrogen Evolution Reaction (HER)	$2H^+ + 2e^- \rightarrow H_2$	0.00 V
Oxygen Evolution Reaction (OER)	$2H_2O \rightarrow O_2 + 2H^+ + 2e^-$	−1.23 V
Overall Reaction	$2H_2O \rightarrow O_2 + H_2$	−1.23 V

To reach ~2A/cm2 (a current density for electrolysis at an economy of scale[6]) a significant amount of overpotential, or voltage in addition to 1.23V is required. Because of this requirement an industrial electrolysis process is estimated to cost ~$4/kg hydrogen[5], which is well above the DOE target of $2/kg hydrogen by 2020[7]. One potential way to reduce the external voltage requirement (and cost) of this process is to generate the required voltage with solar energy in a photoelectrochemical cell (PEC).

Photoelectrochemical water splitting is a process where solar radiation is used to provide the necessary energy to split water.[8–12] The most commonly used system for this process involves a semiconductor light absorber coupled to an electrocatalyst. The role of the semiconductor is to absorb light to generate highly energetic charge carriers (electrons and holes), which are used to drive the water splitting half reactions. Electrons (e-) are used to evolve hydrogen, and holes (h+) are used to evolve oxygen. The electrocatalyst provides chemically active sites for the chemical transformation.

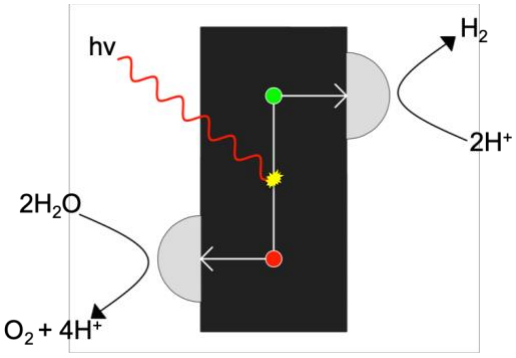

Figure 1.2 | General process solar-to-hydrogen conversion in a photoelectrochemical cell. A photoelectrochemical cell involves a semiconductor to absorb incoming solar photons to form an electron-hole pair. Electrons migrate to the cathode, where they react on an electrocatalyst to form hydrogen. Holes migrate to the anode with an electrocatalyst to evolve oxygen.

As depicted in the schematic in Fig 1.2, in order for the solar-to-hydrogen (STH) conversion to take place the following steps must occur:

1. Photons must be absorbed by the semiconductor and excite charge carriers.

2. Charge carriers must be transported to the surface of the electrocatalyst and have enough potential (photovoltage) to drive the water splitting half reactions.
3. A chemical transformation must take place on an electrocatalytic site.

Theoretically this reaction can be driven by visible light (energy range 3.2–1.6eV), but energetic losses throughout this process make the solar-to-hydrogen (STH) conversion difficult. Improvements in conversion efficiency are necessary in order to lower hydrogen production cost and achieve economic viability. The following section details the various criteria that impact hydrogen production costs and where improvements can be made in this conversion process to improve economic viability.

1.2 Performance Improvements Required to Achieve Economic Viability

The widespread use of photoelectrochemical water splitting ultimately depends on hydrogen production cost. An analysis of how various aspects (reactor design, material cost, efficiency, lifetime, etc.) can affect hydrogen production cost is a critical step for (1) determining whether or not it is possible for this technology to achieve economic viability, and (2) focusing research efforts to improve performance in these areas. For this purpose, there have been several techno-economic analyses to determine what performance criteria have the most impact on economic viability. One such study was organized by the Department of Energy with researchers from academia, industry, and national labs to perform a techno-economic analysis to determine the sensitivity of several design parameters on overall hydrogen production cost. Since there are no photoelectrochemical reactors used in industry today, Pinaud et al.[13] and James et al.[14] performed an economic analysis for various hypothetical reactor designs. The photoelectrochemical reactor systems they studied involved two design schemes: particulate systems and planar systems. The cost analysis was performed by (1) determining the type of

equipment required for each of these systems, (2) determining the equipment size and specifications required to operate a plant with a production rate of 1000kg H_2 per day (yearly average), and (3) estimating the cost of the equipment based on similar systems used in industry. With this cost analysis the authors can determine how various performance criteria affect the total H_2 production cost of each reactor system. The hypothetical photoelectrochemical reactor systems are described below.

Particulate systems: In particulate systems nanoparticles absorb light to generate electron-hole pairs, which react on chemically active sites on the nanoparticle. These involve large open baths of electrolyte with suspensions of nanoparticle absorbers. The product gases (both hydrogen and oxygen together) are collected in "baggies" that rise as gas is evolved.

Planar Systems: These systems involve the use of planar solar absorbers, similar to most photovoltaic cells used today. A major benefit of this type of system is that it is a much more developed technology compared to nanoparticle absorbers, though they are more expensive to fabricate (~\$3/m_2 vs ~\$100/m_2)[13]. Separating the product gases is easier for planar systems and can be done buoyantly. The schematics of both systems are shown in Fig 1.3a-b.

Pinaud et al.[13] and James et al.[14] performed a sensitivity analysis where hydrogen cost was modeled for a baseline performance (black line in Fig 1.3c-d) with a specific STH conversion efficiency, electrode price, and lifetime depending on reactor type, These criteria were then varied to see to what degree they affected overall production costs.

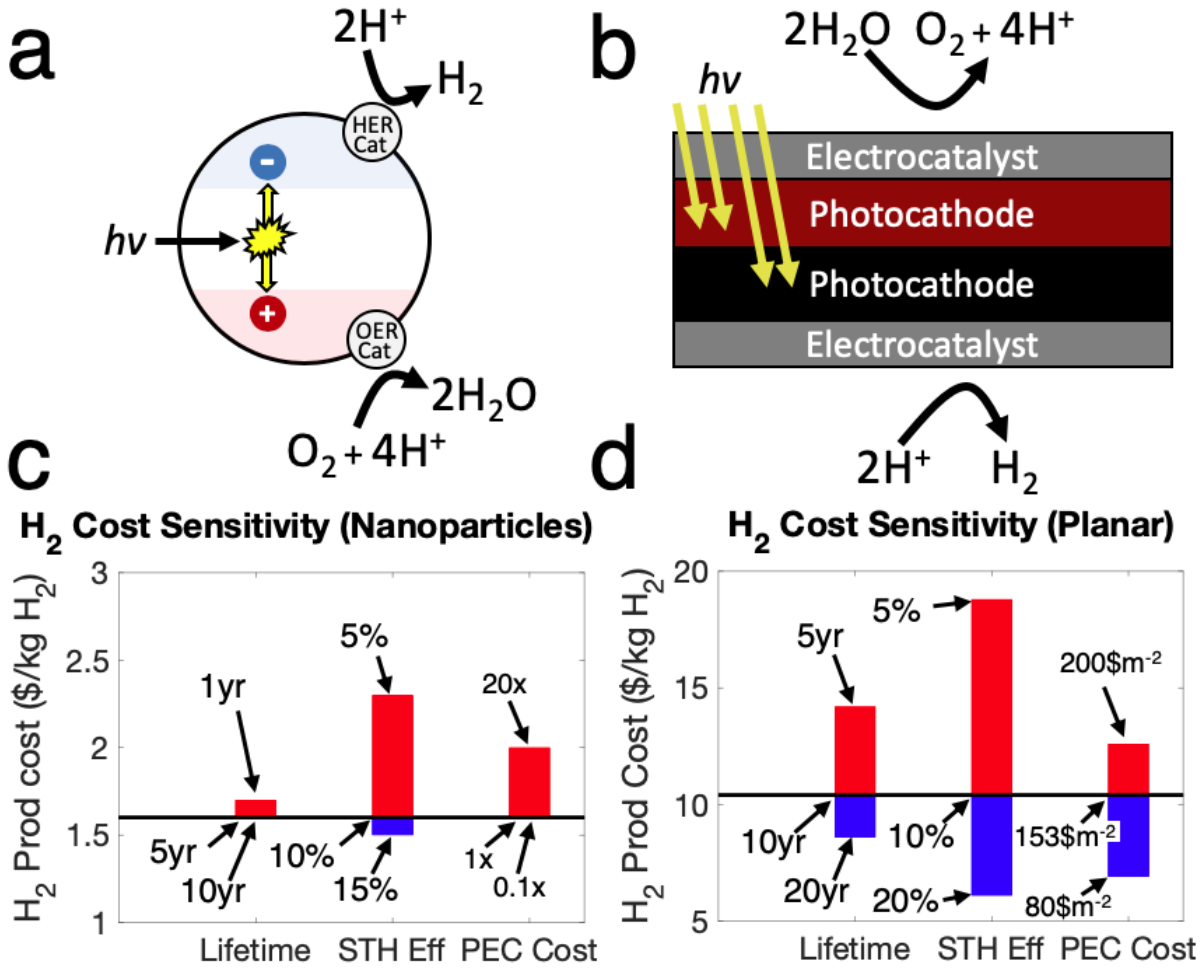

Figure 1.3 | Schematics of photoelectrochemical reactor types and a sensitivity analysis for hydrogen production. a) Schematic of a nanoparticulate solar absorber and attached electrocatalysts. b) Schematic of a planar reactor system. c-d) Sensitivity analysis to determine the how various performance criteria impact overall hydrogen production cost. The black line in c-d represents a baseline H_2 production cost by estimating the following criteria based on the reactor type: lifetime, the photoelectrochemical cell (PEC) cost, and the STH efficiency. The effects of raising (blue bars) or lowering (red bars) the estimates of these criteria on H_2 production cost was determined in a sensitivity analysis. The STH conversion efficiency has the largest impact on overall cost. Figures adapted from Pinaud et al[13].

The results of this analysis are in Fig 1.3c-d, which show that (1) reactor design and (2) solar-to-hydrogen conversion efficiencies per area have by far the largest effect on overall production costs. Improving STH efficiency leads to a large increase in H_2 production without increasing most of the capital costs. While improving STH efficiency may require more expensive

photoelectrodes, the cost of pumps, compressors, baggies, labor, and installation are constants dependent on reactor size (unrelated to electrode cost). Thus, these static costs are effectively reduced by improving STH efficiency. The sensitivity study also shows that if STH efficiencies can be improved to the 10-15% range, it may be feasible to reach the DOE hydrogen production goal of $2/kg especially for the particulate systems. This may begin to make hydrogen produced via electrochemical water splitting roughly competitive with gasoline as a transportation fuel (1kg H_2 has roughly the same energy content as 1 gallon of gasoline). The foremost conclusions of this research were that (1) it is possible for hydrogen produced via photoelectrochemical water splitting to be economically viable, and (2) the viability will depend on improving solar-to-hydrogen conversion efficiency per area and reactor design.

1.3 Improving Solar-to-Hydrogen Conversion Efficiency per Area

The previous section suggests that for a given reactor system improving solar-to-hydrogen conversion efficiency per area has the highest impact in improving the economic viability of photoelectrochemical water splitting. To improve conversion efficiency on a per area basis, the system must maximize its use of incoming radiation, i.e., maximizing the number of photons that are converted into electron-hole pairs with the requisite energy to split water as shown in Fig 1.4.

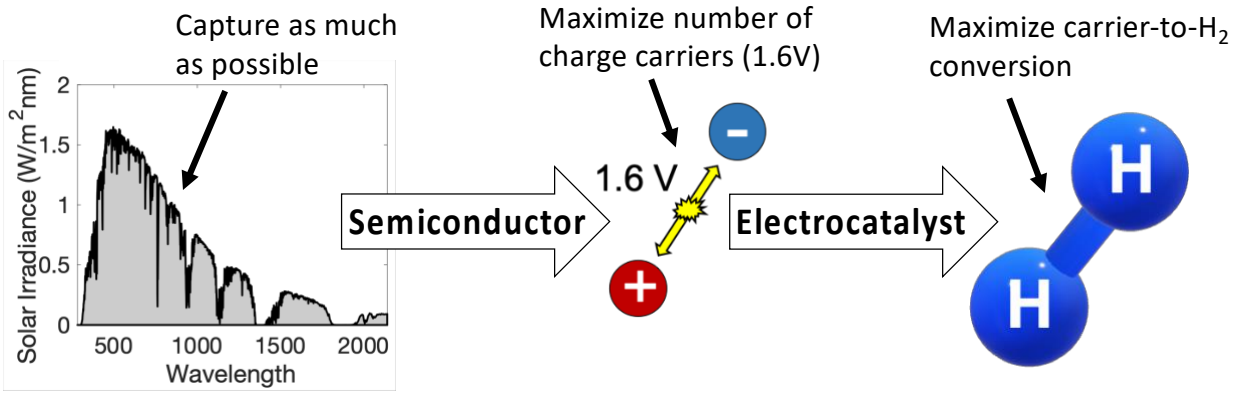

Figure 1.4 | Maximizing solar-to-hydrogen conversion involves improving the efficiencies of each step of the conversion process. The semiconductor must increase the amount of solar absorption in order to maximize the number of charge carriers generated. The charge carriers must migrate to the photocatalyst surface and have enough energy (1.23V + ~0.4V overpotential = ~1.6V) to split water. An electrocatalyst is then required to efficiently convert these carriers into the H_2 product.

One challenge with the first step of this process is that incoming photons do not have a single energy level that could be efficiently absorbed with a single semiconductor, rather, incoming photons have a wide spectrum of energy levels. Any attempt to absorb a wide energy spectrum of photons with a single semiconductor inevitably leads to a set of losses, which create the "Shockley-Quiesser limit"[15]. This loss is caused by the semiconductor band gap, which is the magnitude of energy required to excite charge carriers. Semiconductors cannot create electron-hole pairs with photons whose energy is lower than that of the band gap energy, causing the lower portion of the solar spectrum to be lost as shown in Fig 1.5a. Semiconductors also cannot efficiently use photons with energies much greater than the band gap, since these photons will create highly energetic charge carriers that will quickly thermally relax down to the band gap energy of the semiconductor, also shown in Fig 1.5a. The implications of this effect are that high band gap semiconductors can more effectively use high energy photons, but low band gap semiconductors can capture a larger portion of incoming wavelengths. The Shockley-Queisser limit greatly reduces the solar-to-hydrogen conversion efficiency for photoelectrochemical cells.

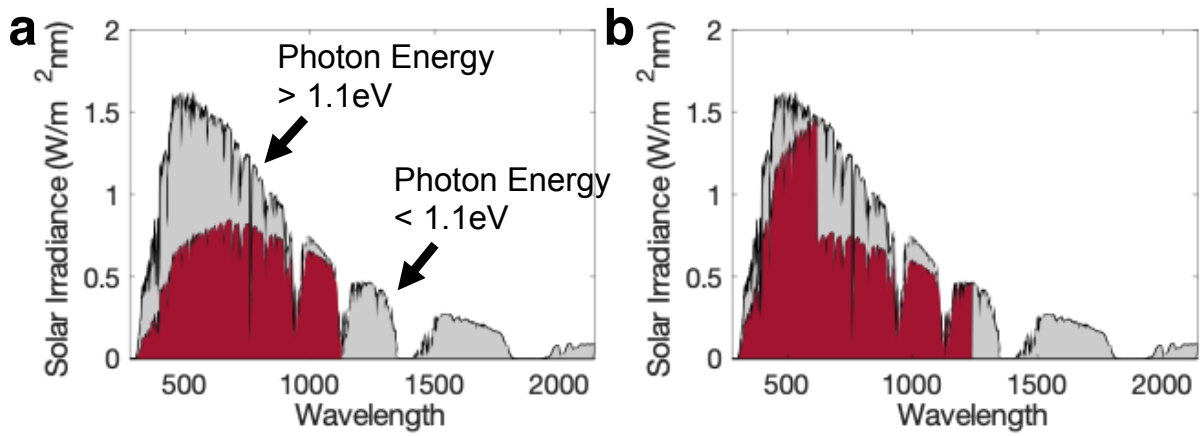

Figure 1.5 | Captured solar spectrum for various band gap semiconductors. The graphs are a visual representation of the amount of light that can be absorbed by a semiconductor given its band gap. a) Solar spectrum captured by low band gap semiconductor of 1.1eV (similar to Si). b) Solar spectrum captured by a tandem system band gaps of 2eV and 1eV. Calculations are based on the 1.5 AM solar spectrum data[16].

STH efficiency can be improved by developing systems that can capture more of the solar spectrum. One way to do this is to implement the use of a tandem semiconductor system[17–20]. This type of system involves using two semiconductors, generally using one to absorb high energy photons and another to absorb low energy photons (Fig 1.5b). By using two semiconductors their captured solar irradiance overlaps to utilize much more of the solar spectrum and improve STH conversion efficiency. There have been several sensitivity analyses that have been performed in order to determine what type of semiconductor band gaps would be necessary to maximize efficiencies in a tandem system. Seitz et al.[21] showed that to maximize efficiencies one semiconductor should have a band gap of ~2eV and a second semiconductor should have a band gap of ~1eV. While semiconductors in this 1-2eV band gap range have often been used in the photovoltaic industry, traditionally water-splitting systems have used metal oxide semiconductors such as TiO_2 with much higher band gaps[10]. The reason for this is that these large band gap semiconductors are often more stable in the harshly oxidative conditions of a photoelectrochemical cell.

In order for a semiconductor to be stable within an aqueous electrolyte in water splitting conditions, it must be able to perform the water oxidation reaction and hydrogen evolution reaction before the semiconductor itself oxidizes or reduces. This is shown in the following figure adapted from Chen et al[22]. The solid black and red lines are the potentials where the semiconductor itself oxidizes or reduces respectively. If these lines lie within the dashed lines (the water oxidation and reduction lines) than the semiconductor is unstable.

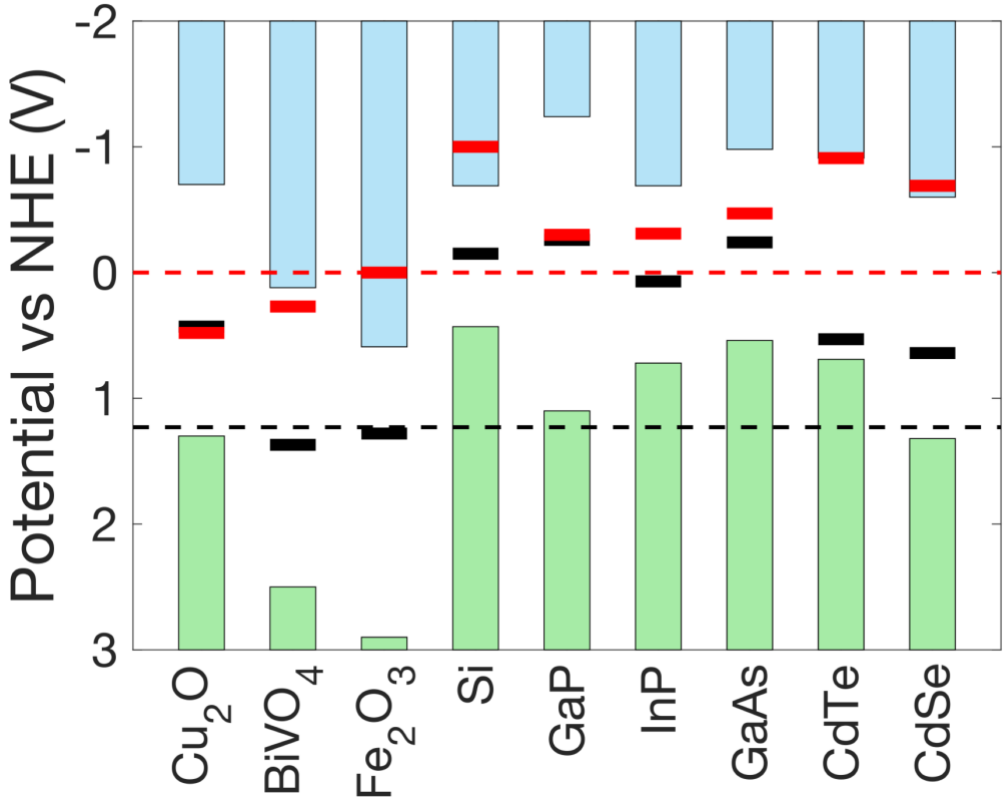

Figure 1.6 | Band gaps and stability data of various semiconductors systems. The semiconductor band gaps are the distance between green valence bands and blue conduction bands. In an aqueous environment the black and red lines are the potential at which the semiconducting material will oxidize or reduce respectively (losing its material integrity). If the solid black and red lines lie within the dashed lines (water oxidation/reduction potentials) then the semiconductors are unstable in solution since they will self-oxidize/reduce before water does. Figure adapted from Chen et al.[22]

To maximize efficiencies water splitting systems require semiconductors with band gaps near the 1-2eV range, such as Si[23–28], $BiVO_4$[19,29–31], Fe_2O_3[32,32,33], GaAs[34], Cu_2O[35,35,36], etc. It is

apparent, however, from Fig 1.6 that many of these semiconductors with band gaps close to this range will self-oxidize or self-reduce before they can be used to perform the water splitting half reactions. In order for these semiconductors to be used they must be protected from the a highly oxidative/corrosive environment of an electrochemical cell. Recently there has been intense research efforts to develop protection strategies for this type of semiconductors. Reviews of these protection strategies can be found in Refs. 37–40. In general, protection strategies isolate the underlying semiconductor from the electrolyte using a thin metal or metal oxide material.

The major challenges of protection layer technologies are to (1) ensure the long-term stability of the photoelectrode material, (2) limit parasitic optical absorption of the protective/electrocatalytic materials on the semiconductor surface, and (3) integrate the protection strategy in such a way that the underlying semiconductor can generate charge carriers with enough energy to drive the electrochemical half reactions. This third challenge requires each semiconductor of a tandem system to generate as much photovoltage as possible in order to reach the requisite potential to split water. There have been several photoelectrochemical design strategies proposed to address this challenge. One commonly used strategy involves the formation of a p-n junction at the semiconductor surface[37–39,41–45]. A stable metal or metal oxide material coats the surface of the p-n junction to isolate the semiconductor from the electrolyte. Another strategy involves the formation of a semiconductor heterojunction, where photovoltage is generated between two different materials. An example of this is a study that coated the surface of a n-type semiconductor with a sol-gel deposited Ni oxide, which both protects the semiconductor and acts as an electrocatalyst[46]. Each of these strategies have important advantages and limitations e.g. p-n junctions can generate high photovoltage, but are expensive and limited to easily-doped

semiconductors, meanwhile, the top layer of a heterojunction must be stable, transparent, and catalytically active lest they require a more complicated interfacial geometry.

1.4 Protective MIS Structures

The protection strategy that will be the focus of this dissertation is a metal-insulator-semiconductor (MIS) structure, which has been used in a variety of recent work to protect the semiconductor from the corrosive electrolyte environment[24,34,35,40,41,47–54]. These systems involve the use of a semiconductor absorber covered by a thin insulator, which is stable in an electrochemical environment. Examples of insulator-protected photoelectrodes employ a Si semiconductor covered with an Al_2O_3[55–58], TiO_2[24,50,57,59–61], ZrO_2[51], $SrTiO_3$[25], or (in this work) HfO_2[62,63] protective layer onto which a metal electrocatalyst was deposited. The metal layer serves a dual purpose of setting the junction characteristics (discussed in Ch. 2) and providing highly electroactive sites to perform the water splitting half reactions. Major advantages of MIS systems are the flexibility for use with a variety of semiconductors, and the simple electrode architecture relative to other strategies that require additional processing such as p-n junction fabrication. While MIS systems have been studied extensively in photovoltaic applications[64–67], recently they have received renewed attention in photoelectrochemical applications where insulator layers are necessary to improve stability. The use of MIS structures in water-splitting systems subjects them to several additional constraints such as stability concerns and the necessity of providing electrocatalytic sites for the water splitting half reactions. Considerable research effort is needed to understand and optimize optical absorption, photovoltage generation, electrocatalytic activity, and stability of MIS systems for this application. This work focuses on the design of a MIS interface in order to optimize efficiencies in these areas.

Chapter 2

Physical Characteristics of Metal-Insulator-Semiconductor Interfaces

2.1 Interfacial Characteristics of a MIS interface

The previous chapter discusses the need to develop tandem photoelectrochemical systems using semiconductors in the 1-2eV band gap range in order to maximize solar absorption. For this system to operate successfully it must (1) remain stable in solution and (2) have each semiconductor combine to have enough photovoltage to drive the overall reaction. MIS structures are of interest in this application because they have the potential to address both of these challenges. The stability of the materials can be addressed by the choice of insulator and electrocatalyst materials, whereas photovoltage can be produced via the Schottky barrier at a MIS interface. A comprehensive understanding of the interfacial characteristics that govern the performance of MIS systems is necessary to design electrodes that maximize photovoltage. This has made MIS interfaces the subject of extensive research effort. This section will outline the interfacial mechanisms critical to generate photovoltage in these systems.

2.2 Band Bending with a Schottky Barrier

The electronic band structure of semiconductors gives them unique properties in comparison to metals and insulators[68]. These properties have precipitated their widespread use in applications ranging from solar cells to transistors. A semiconductor band structure has filled and unfilled energy levels called the valence and conduction band, respectively. The difference

between these energy bands is called the band gap of the material. While this structure is similar to insulators that have filled valence bands and empty conduction bands, the conduction bands of a semiconductor are partially filled (populated thermally). The degree to which the conduction/valence bands are filled depend on a property known as the Fermi level, which is the electron energy level (electron electrochemical potential) of the material. This property can be tuned by doping the semiconductor with electron donors or electron accepters, which can shift the Fermi level upwards to make electron-rich n-type semiconductors or downwards to make hole-rich p-type semiconductors. In n-type semiconductors electrons are the majority charge carrier and holes are the minority charge carrier, while the opposite is true for p-type semiconductors.

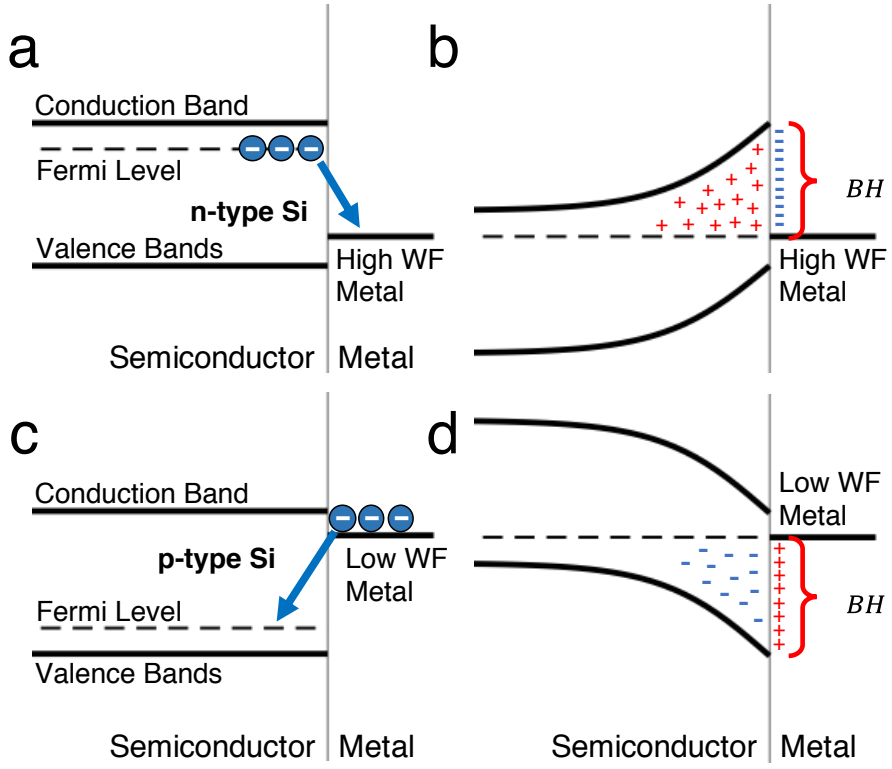

Figure 2.1 | Band diagrams for semiconductors coupled to a metal. The initial differences in the Fermi levels of the two materials causes charge transfer to occur at the interface. The charge transfer leads to a build-up of an electric field and the semiconductor bands to bend. (a-b) Band diagrams of a n-type semiconductor coupled to a high work function metal (a) before and (b)

after equilibration. ϕ_{BH} is the barrier height (BH) of the system. (c-d) Band diagrams of a p-type semiconductor coupled to a low work function metal (a) before and (b) after equilibration.

The Fermi level of a semiconductor becomes critical when the semiconductor is placed into direct contact with a metal. A metal has its own intrinsic Fermi level, which is related to the work function of the material. This difference in electron electrochemical potential will create a driving force for charge transfer to occur across this interface until the Fermi levels equilibrate. For an n-type semiconductor (high Fermi level) in contact with a high work function metal (low Fermi level) as shown in Fig 2.1a, electrons will transfer from the semiconductor to the metal, which causes electrons accumulate within the metal. Since charges can move freely in a metal, these electrons are localized directly at the metal surface. To maintain neutrality positive charge accumulates in the semiconductor, which has a lower concentration of free charge carriers in comparison to a metal. This lower concentration of free carriers causes the positive charges in the semiconductor to be accumulated in the "space charge" region of the semiconductor roughly on the order of 10nm deep into the semiconductor[69], rather than directly at the interface (like the metal). The accumulation of positive charges near the semiconductor surface creates an electric field in the semiconductor and causes semiconductor bands to bend so that the Fermi levels of the metal and semiconductor are equilibrated as shown in Fig 2.1b[69–71]. The situation where an n-type semiconductor is coupled to a high work function metal creates an "inversion layer" where positive charges accumulate towards the surface of the n-type semiconductor (making the surface of the semiconductor have similar properties to a p-type semiconductor). This type of interface is called a Schottky barrier and is central to the generation of photovoltage under photo-illumination. An inversion layer can also be created by a p-type semiconductor coupled to a low work function metal, as shown in Fig 2.1c-d.

2.3 Generating Photovoltage under Illumination

Absorbed light creates electron-hole pairs near the surface of the semiconductor, creating a large population energized minority charge carriers. The electric field created by a the Schottky barrier will cause minority carriers to move towards the interface and majority carriers away from the interface. The electrochemical potential of these energized minority charge carriers can be described with its own minority carrier Fermi level as shown in Fig 2.2a. In an electrochemical cell if the potential of the highly energetic minority carriers is higher (for oxidation) than the equilibrium potential of the electrochemical half reaction, than the current will start to flow as the reaction occurs. This is in contrast to a typical electrochemical reaction (no illumination) where applied potential, V_{app} in Fig 2.2b, alone is used to drive the reaction. The photovoltage provided by the semiconductor decreases the amount of applied potential required for a given reaction. The photovoltage can be defined as the difference between the majority and minority charge carrier Fermi levels.

For a photoelectrode to perform unassisted water splitting, the system must provide ~1.6V in photovoltage (1.23V due to thermodynamics + ~0.4V for electrocatalytic overpotential). To achieve this goal there has been research in both (1) reducing the total amount of photovoltage required by improving electrocatalytic activity thus reducing overpotential, and (2) maximizing the amount of photovoltage the system can produce. While there is a significant amount of research directed at reducing the required electrocatalytic overpotential for both HER[72–75] and OER[76–82] (the latter of which requires large overpotentials), the development of systems that can maximize the photovoltage the semiconductor can provide is critical for the development of functional water splitting systems. The next section will outline how a semiconductor produces photovoltage and various factors that affect the amount generated.

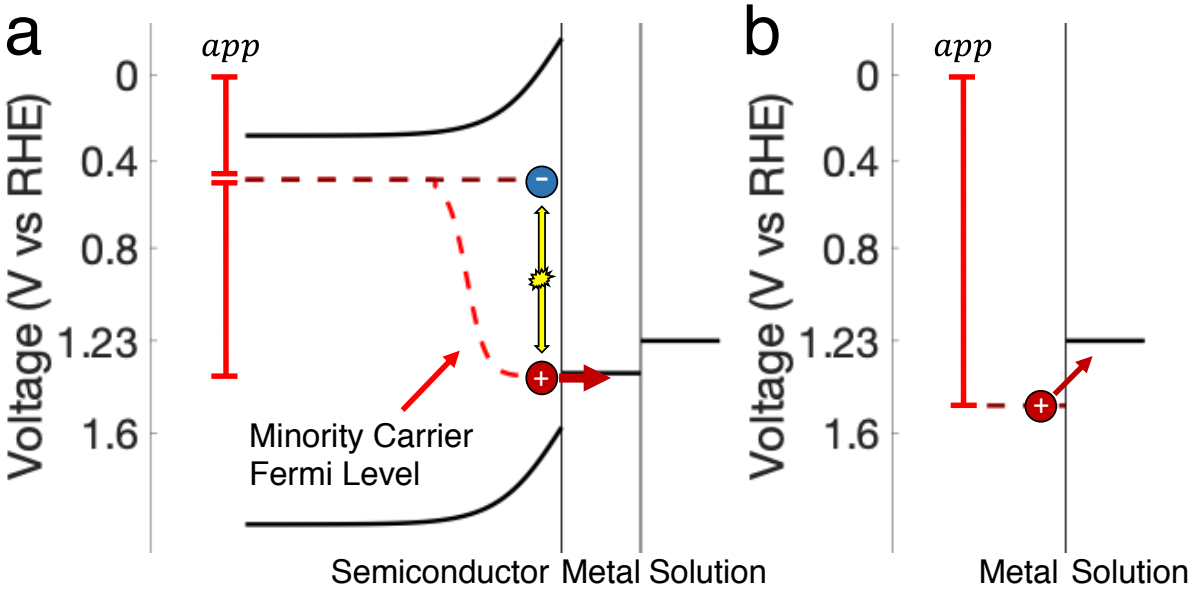

Figure 2.2 | Band diagrams of an photoelectrochemical and electrochemical system. (a) The photoelectrochemical system uses a semiconductor to produce highly energetic minority charge carriers described with its own quasi-Fermi level. These carriers allow the semiconductor to produce photovoltage (Pv) and require less applied voltage (V_{app}) to perform electrochemical reactions. (b) Electrochemical system uses applied voltage alone to generate charge carriers with enough potential to perform the redox reaction.

2.4 Factors that Affect Photovoltage

There are various physical characteristics of Schottky barriers that can influence the amount of generated photovoltage. This section will discuss some of these parameters, which need to be considered in order to develop high performance systems.

Band Gap

The maximum photovoltage a semiconductor can produce is directly dependent on the semiconductors band gap. Well performing semiconductors will provide ~0.4-0.6V below their band gap[21]. One way for a system to provide the necessary ~1.6V is to use very high band gap semiconductors. However, this strategy is fundamentally limited since higher band gap semiconductors will absorb less of the solar spectrum. This leads to a tradeoff between the photovoltage the system can provide and the magnitude of the current it generates—,i.e., less

absorbed photons leads to less electron-hole pairs and ultimately less current. There are several sensitivity analyses that discuss how to optimize the current-photovoltage tradeoff, which determined that the 1-2eV band gap range is ideal for a tandem system[21,83], as discussed in Ch 1.

Barrier Height

One extremely important parameter is called the barrier height of the system, which, for an n-type system, is calculated as the difference between the isolated semiconductor valence band edge and the metal Fermi level. The barrier height is related to the amount of initial band bending in the system caused by the inherent differences in the Fermi levels of the two materials. The barrier height is related to the magnitude of the electric field at the semiconductor surface (how much the bands are bent) and is marked by ϕ_{BH} in Fig 2.1 b and d. This electric field is the driving force for minority carriers to move towards the interface and majority carriers away from the interface. If the barrier height is small the driving force for majority carriers isn't sufficient to shuttle charge carriers away from the interface. Majority carriers can leak across the interface and recombine with minority carriers in the metal, ultimately leading to a loss in photovoltage. This phenomenon is captured by the "ideal diode equation" shown below[84].

$$J = J_{ph} - AT^2 \exp\left(\frac{-q\phi_{BH}}{kT}\right)\left[\exp\left(\frac{qV_{semi}\eta}{kT}\right) - 1\right]$$

EQ 2.1

J is the diode current and J_{ph} is the photocurrent (minority carriers moving across the interface). The second term on the right side of the equation represents majority carriers that can potentially leak across the interface. A is the Richardson constant, V_{semi} is the voltage applied to the semiconductor, and η is an ideality factor. As shown the equation, increasing the barrier height creates an exponential reduction in the majority carrier leakage current. This can cause a large reduction in the amount of recombination in the system, increasing photovoltage. The

choice of semiconductor and metal materials with large inherent differences in the electronic Fermi levels is critical to maximize the system barrier height.

Surface States

While an ideal Schottky barrier has a barrier height dependent on the relative Fermi level positions of the semiconductor and metal, various factors cause experimental systems to deviate from this behavior. One phenomenon that can cause this deviation are the formation of electronic surface states between the semiconductor and metal. The surface states can be caused by semiconductor dangling bonds, "metal induced gap states", vacancies, the formation of silicides/oxides, etc. A large number of electronic states will cause the semiconductor to equilibrate or be "pinned" to the energy of the surface states rather than the overlying metal. This phenomenon is called "Fermi level pinning" and can cause system to have a much lower barrier height than would be expected for a given semiconductor-metal system, thus diminishing generated photovoltage[85,86].

Insulator Layer

The addition of the insulator layer in an MIS system causes critical changes to the energy band diagram. The changes caused by moving from a metal-semiconductor (MS) to an MIS structure are outlined in the next section.

2.5 How Insulators Affect Energy Band Diagrams

The insulator of a metal-insulator-semiconductor structure has significant effects on several properties of system. A comprehensive understanding of these effects is necessary for the development of MIS water splitting systems.

Charge Carrier Fluxes

Insulators have much wider band gaps than the semiconductors, which creates a barrier for both electrons and holes between the semiconductor and the metal. This band structure often necessitates tunneling in order for charge carriers to move from the semiconductor to the electrocatalyst.

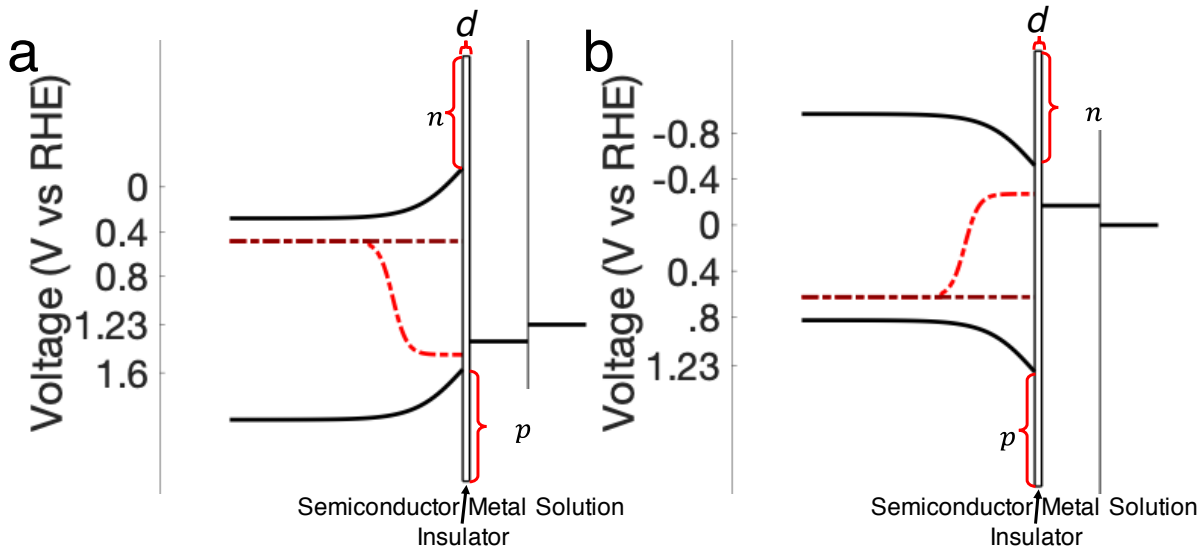

Figure 2.3 | Band diagrams for metal-insulator-semiconductor (MIS) structures under illumination. (a) represents an n-type semiconductor and (b) represents a p-type semiconductor. The insulator creates a barrier for both majority and minority carriers to cross the interface. The decrease in charge carrier flux across the interface depends on the insulator thickness (d) as well as the size of the energetic barrier for electrons (ϕ_n) and holes (ϕ_p).

Direct tunneling through an insulator layer creates a "tunneling probability" for electrons and holes to move from the semiconductor to the metal, which can be approximated with the following equations[68].

$$T_n \approx \exp\left(-\propto_t d\sqrt{\phi_n}\right) \qquad \text{EQ 2.2}$$

$$T_p \approx \exp\left(-\propto_t d\sqrt{\phi_p}\right) \qquad \text{EQ 2.3}$$

Where T_n and T_p is the tunneling probability for electrons and holes respectively, $\propto_t$ is a constant that is a function of the electron effective mass in the insulator, d is the insulator thickness, and ϕ_n and ϕ_p is the energetic barrier for electrons and holes. The thickness of the insulator can exponentially decrease the tunneling probability, which can cause large changes in the flux of charge carriers across the semiconductor-metal interface.

Barrier Height Variation

In some semiconductor-insulator-metal systems, electronic states within the insulator have caused changes to the system barrier height, where the junction height is set by the mid-gap states in the insulating material (rather than the overlying metal). The insulator's effect on the barrier height can be both dependent on the type of insulator as well as processing conditions during deposition. Different groups depositing the same insulator with small changes to the processing conditions have caused large differences in the properties of the synthesized material[60,61].

Surface State Passivation

In addition to changes in the flux of charge carriers and barrier height, insulators can also passivate surface states at the semiconductor surface that would otherwise lead to Fermi level pinning. Insulator-based surface passivation with insulating materials has been shown to improve efficiencies in both solar cells[87–89] and water splitting systems[60,61,90,91].

2.6 Conclusions

This chapter discussed the critical role of MIS interfaces in the generation of photovoltage for a given semiconductor. MIS interfaces can form Schottky junctions, which are created by inherent differences in the electronic Fermi level of the semiconductor and metal. These junctions can be leveraged to generate photovoltage under illumination. There are multiple

design parameters in metal-semiconductor based junctions (discussed in Sec. 2.4), which must be optimized to maximize the amount of generated photovoltage. The insulator layer adds additional complexities (discussed in Sec. 2.5) that also require consideration. A holistic understanding of MIS interfaces, which incorporate the multiple design parameters governing performance is critical for the development of high performing systems. The next chapter will discuss the development of comprehensive models of photoelectrochemical MIS systems to guide the design of highly efficiently experimental systems.

Chapter 3

Modeling the Interfacial Mechanisms of an MIS Interface

3.1 Introduction to MIS modeling

The development of computational models of MIS systems that capture the various interfacial mechanisms that govern performance can be used to guide the design of highly efficient systems. A comprehensive model must integrate optical absorption, photovoltage generation/charge separation, and electrocatalytic kinetics in order to fully capture a photoelectrochemical process. A model basis that can incorporate the physical parameters of the semiconductor, insulator, and electrocatalyst (which can be tuned in experimental systems) are particularly useful for efficiency optimization. The following chapter describes the development of such a model system, as well as the insights it provides about the underlying physical mechanisms that can be leveraged to maximize efficiencies.

3.2 Simple Models Capturing the Behavior of Metal-Semiconductor Interfaces

Simple models that can capture the basics principles of photoelectrochemical systems are a useful starting point for model development. The purpose of these models is to capture the current-voltage relationship, $J(V)$, for a photoelectrode, which captures the performance of the system. The current density (J) measures the electrochemical reaction rate (4e- are generated during water oxidation and 2e- are required in hydrogen evolution. The applied potential, V, is related to the photovoltage. High performing photoanodes will maximize positive current at

minimum positive applied potential (Fig 3.1a), and high performing photocathodes will maximize negative current at minimum negative applied potential (Fig 3.1b).

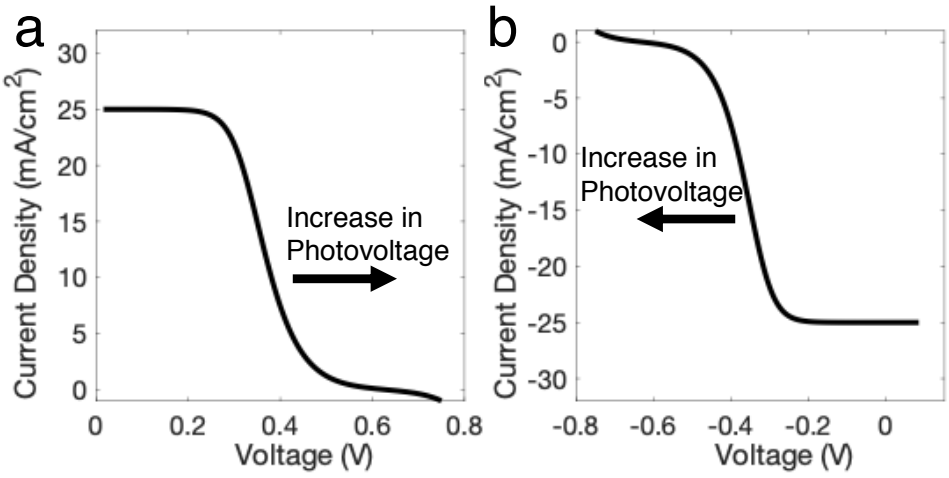

Figure 3.1 | General current voltage relationship of a photoelectrochemical system. (a) represents a photoanode, while (b) represents a photocathode. Photoanodes provide photovoltage by enabling oxidation reactions to occur at less oxidative (positive) potentials, while photocathodes allow reduction reactions to occur at less reductive (negative) potentials.

The simplest model that captures the basic behavior of a photoelectrochemical system combines the Butler-Volmer equation with the ideal diode equation. The direct combination of these equations assumes that the potential required by the electrocatalyst (kinetic overpotential to reach a specific current) appears as a voltage drop at the metal/solution interface and does not influence band bending within the semiconductor. This assumption means that the voltage drops in the semiconductor and metal can be captured using an in-series description that separately calculates the current-voltage relationship for these components. This assumption holds for electrocatalytic metal films and can well-approximate electrocatalytic surface nanoparticles[84], but there are reported situations in porous electrocatalysts where the overpotential voltage-drop occurs spatially throughout the electrocatalyst (not just at the metal surface) and the approximation breaks down[92–94]. The in-series description of the system means that the following equations hold:

$$J_{tot}(V_{tot}) = J_{cat}(V_{cat}) = J_{semi}(V_{semi}) \quad \text{EQ 3.1}$$

$$V_{tot} = V_{cat} + V_{semi} \quad \text{EQ 3.2}$$

where the total current (J_{tot}) is equal to the current passing through the semiconductor (J_{cat}) and the electrocatalyst (J_{semi}). The total voltage (V_{tot}) is the summation of the voltage required by the electrocatalsyt (V_{cat}) and the semiconductor (V_{semi}). The in-series description allows J_{cat}, and V_{cat} to be described simply via the Butler-Volmer equation, which is a well understood equation to calculate electrochemical kinetics:

$$J_{cat} = J_{ocat}\left[\exp\left(\frac{z\beta F V_{cat}}{RT}\right) - \exp\left(\frac{-z\beta F V_{cat}}{RT}\right)\right] \quad \text{EQ 3.3}$$

where J_{ocat} is the electrocatalyst exchange current, z is the number of electrons, and β is the symmetry factor, and F is Faraday's constant.

One way the $J_{semi}(V_{semi})$ relationship can be approximated is with the ideal diode equation, which was described in Sec 2.4. A model that uses a combination of the ideal diode equation and the Butler-Volmer equation to describe $J_{semi}(V_{semi})$ and $J_{cat}(V_{cat})$ respectively is able to capture the basic behavior of an photoelectrochemical system, and was used to calculate the curves shown in Fig 3.1.

The ideal diode equation, however, provides an incomplete description of the individual majority and minority carrier fluxes in MIS systems. Essentially the ideal-diode equation assumes that there is always a high flux of minority carriers (J_{ph}) crossing the diode under illumination and current is governed by majority carriers leaking through the interfacial barrier and recombining with minority carriers. Non-ideal deviations from this behavior such as alternate recombination pathways are accounted for in η, which is difficult to relate to physical

parameters of the system particularly for multiple non-idealities. Additionally, in MIS systems the flux of minority carriers is dependent on the thickness of the insulator (which they must tunnel through), the size of the energetic barrier (ϕ_n in Fig 2.3) the barrier height, and the applied voltage. A more complex $J_{semi}(V_{semi})$ relationship that accounts for how various physical parameters of the semiconductor-insulator-metal interface can change individual charge carrier fluxes is useful to determine how performance can be optimized in MIS systems.

3.3 Comprehensive Modeling of MIS Interfaces

A comprehensive, predictive model of an MIS system that shows the impact of physical parameters on efficiency can assist the design process for experimental systems. This type of model must be able to accurately describe the changes in the flux of charge carriers caused by the insulator. It would also be useful to develop a model that enables band diagram calculations, (examples of band diagrams are shown in Fig 2.3) in order to determine the underlying mechanisms that enhance/reduce performance. To achieve these objectives a comprehensive mathematical model was developed that describes the underlying physical processes taking place on layered MIS photoelectrocatalysts. The model has been described in Refs. 62,63 and originally based upon work in Ref. 93. The purpose of the model is to provide a more accurate description of $J_{semi}(V_{semi})$ in comparison to the ideal diode equation. Additionally, band diagrams can be calculated if the potential and charge carrier concentrations are determined as a function of depth in the semiconductor. These profiles will be defined as $\phi(x)$, $n(x)$, and $p(x)$ for the potential, electron concentration, and hole concentration respectively. Band diagrams can be determined from these profiles because the bending in the semiconductor bands and the individual charge carrier Fermi levels can be determined from EQ 3.4 and EQ 3.5:

$$E_C = E_C^0 - \phi(x); E_V = E_V^0 - \phi(x) \qquad \text{EQ 3.4}$$

$$E_{f,n} = k_b T \ \ln\frac{n(x)}{N_C} + E_C; E_{f,p} = E_V - k_b T \ \ln\frac{p(x)}{N_V} \quad \text{EQ 3.5}$$

where E_C and E_V the semiconductor conduction and valence bands, E_C^0 and E_V^0 are the isolated semiconductor conduction and valence bands (before equilibration), $E_{f,n}$ and $E_{f,p}$ are the electron and hole fermi levels, and N_C and N_V are the density of states in the conduction and valence band.

In this work $J_{semi}(V_{semi})$ as well as $\phi(x)$, $n(x)$, and $p(x)$ are calculated using a combination of charge carrier continuity equations and Poisson's equation. The charge carrier continuity equations track where the charge carriers are going throughout the system and are provided in EQ 3.8 and 3.9. They have an absorption term for the formation of electron/hole pairs, a radiative recombination term, and a diffusion term.

$$\Phi\alpha e^{-\alpha x} + B(\bar{n}\bar{p} - np) + (\phi' p + p')' = \frac{dp}{dt} = 0 \quad \text{EQ 3.8}$$

$$\Phi\alpha e^{-\alpha x} + B(\bar{n}\bar{p} - np) + (-\phi' p + n')' = \frac{dn}{dt} = 0 \quad \text{EQ 3.9}$$

where is ϕ is the potential, B is a recombination coefficient, $\bar{n}$ and $\bar{p}$ the bulk hole and electron concentrations, Φ is the incoming photon flux, α is the optical absorption coefficient. The differentials are with respect to depth within the semiconductor. The potential of the semiconductor, ϕ, is solved with Poisson's equation (EQ 3.10), which is the governing equation for electrostatics in the system.

$$\phi'' = n - p + 1 \quad \text{EQ 3.10}$$

The model solves these differential equations using finite differences at nodes across the interface with increasing depth (x) so that the charge carrier concentrations at each point (x_n) is dependent on absorption and recombination at that point and the charge carrier fluxes from neighboring points (x_{n-1}, x_{n+1}).

To solve these differential equations boundary conditions are required. One of the boundary conditions to consider is in the bulk of the semiconductor at x_N, where the charge carrier concentrations are equal the bulk semiconductor concentrations: $n(x_N) = n_{bulk}$, $p(x_N) = p_{bulk}$. The potential at this boundary, $\phi(x_N)$, is a function of the applied voltage (V_{semi}).

The other boundary condition at x_1 is at the interface of the semiconductor and electrocatalyst. This boundary condition is particularly important since the flux of carriers across the interface corresponds to electrochemical current, thus reaction rate. This boundary condition for the charge carrier continuity equation can be described using the following equations[63,65,68,93]:

$$J_p = k_p T_p (p_s - \bar{p}_s); J_n = k_n T_n (n_s - \bar{n}_s) \quad \text{EQ 3.11}$$

In this equation J_n and J_p are the interfacial electron and hole currents respectively. The net current is $J_p - J_n$. k_n and k_p are the charge transfer rate coefficients for electrons and holes (these depend on the density of states in the semiconductor and metal) and are assumed to be the same value in this system as is generally the case[63,93]. The tunneling probabilities T_n and T_p are defined in EQ 2.2 and 2.3 and depend on the insulator barrier/thickness. n_s and p_s are the electron and hole concentrations of the semiconductor surface at a specified illumination/applied potential, while $\bar{n}_s$ and $\bar{p}_s$ represent the surface carrier concentrations in equilibrium in dark. These concentrations depend on the initial barrier between the semiconductor and metal in dark equilibrium conditions and are described in EQ 3.12.

$$\bar{n}_s = n_{bulk} exp\left[\frac{-q(\phi_m - \phi_s)}{k_b T}\right];\ \bar{p}_s = p_{bulk} exp\left[\frac{q(\phi_m - \phi_s)}{k_b T}\right] \qquad \text{EQ 3.12}$$

ϕ_m is the work function of the metal, and ϕ_s is the isolated semiconductor's Fermi level. Noteworthy is that EQ 3.12 essentially captures the change in barrier height as the function of the metal work function.

A schematic of how these equations fit into the model is presented in Fig 3.2. By solving these differential equations at nodes throughout the semiconductor (with more nodes at semiconductor surface), a solution to the differential equations can be calculated that determines $\phi(x)$, $n(x)$, and $p(x)$. This is done for both Poisson's equation and the charge carrier continuity equations. Since the solutions are interdependent, iteration is used to converge on a solution for the charge carrier and potential profiles.

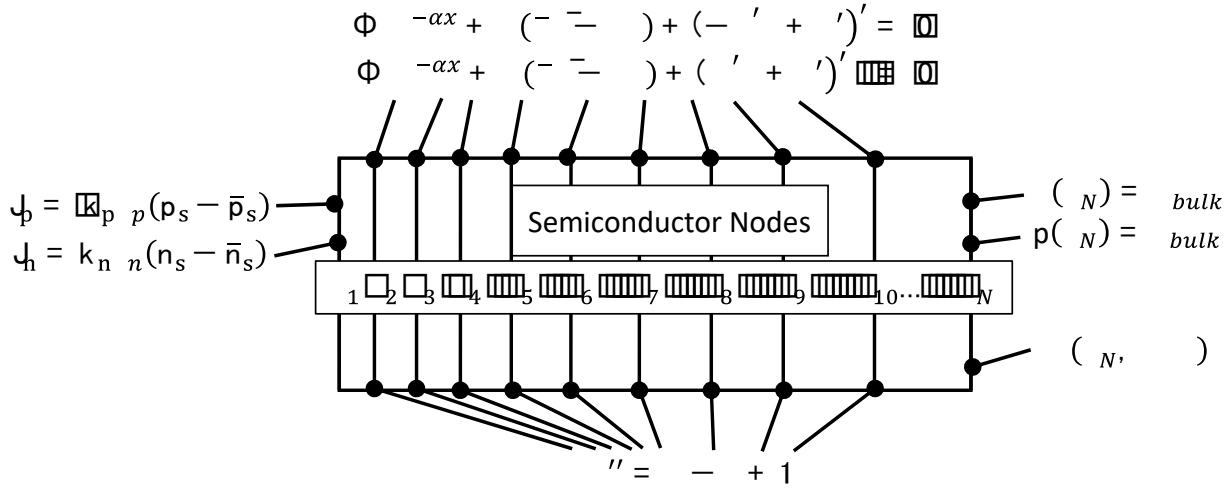

Figure 3.2| Schematic of how the Poisson's equation and charge carrier continuity equations fit into the model. These differential equations are solved at nodes at the semiconductor interface in order to determine $\phi(x)$, $n(x)$, and $p(x)$. These profiles can then be used to calculate band diagrams and current voltage relationship (performance).

3.4 Results with Comprehensive Model

A converged solution of the model is able to calculate $\phi(x)$, $n(x)$, and $p(x)$. Example profiles of a p-type semiconductor at reducing potentials are shown in Fig 3.3. The majority

carriers show a clear depletion region close to the interface, which is typical of an inversion layer.

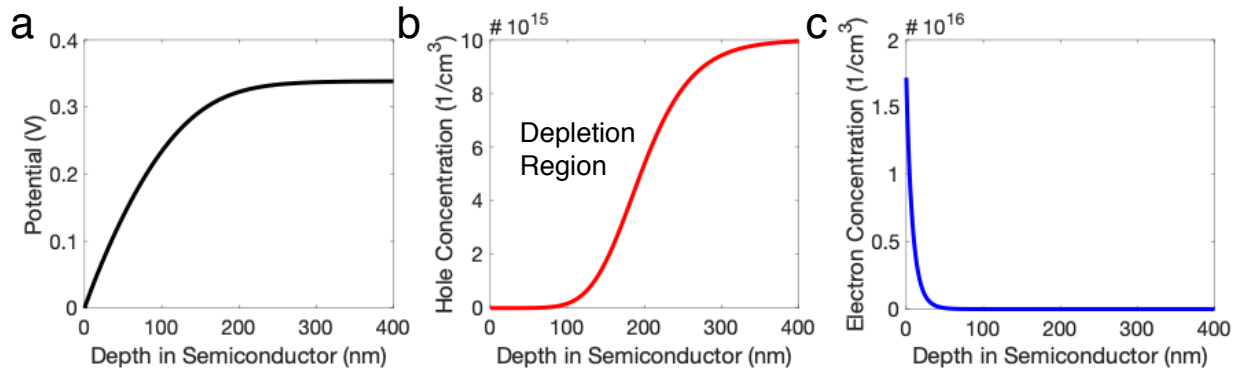

Figure 3.3 | Potential, electron concentration, hole concentrations as a function of depth in a semiconductor. (a) represents the potential profile, (b) represents the majority carrier holes concentration profile, and (c) represents the minority carrier electron profile. These profiles are calculated for a p-type silicon like semiconductor under illumination. The hole concentration shows a clear depletion region caused by the rectifying barrier. The minority carrier, electrons, are shuttled to the semiconductor surface.

These profiles can be used to calculate the current crossing the semiconductor (J_{semi}) by plugging in $n(x_s)$ and $p(x_s)$ to the interfacial flux equations listed in EQ 3.11. This provides the $J_{semi}(V_{semi})$ relationship needed to calculate the overall $J_{cathode}(V_{tot})$. An example $J_{cathode}(V_{tot})$ is provided in Fig 3.4 along with a corresponding band diagram the can be calculated from $\phi(x)$, $n(x)$, and $p(x)$.

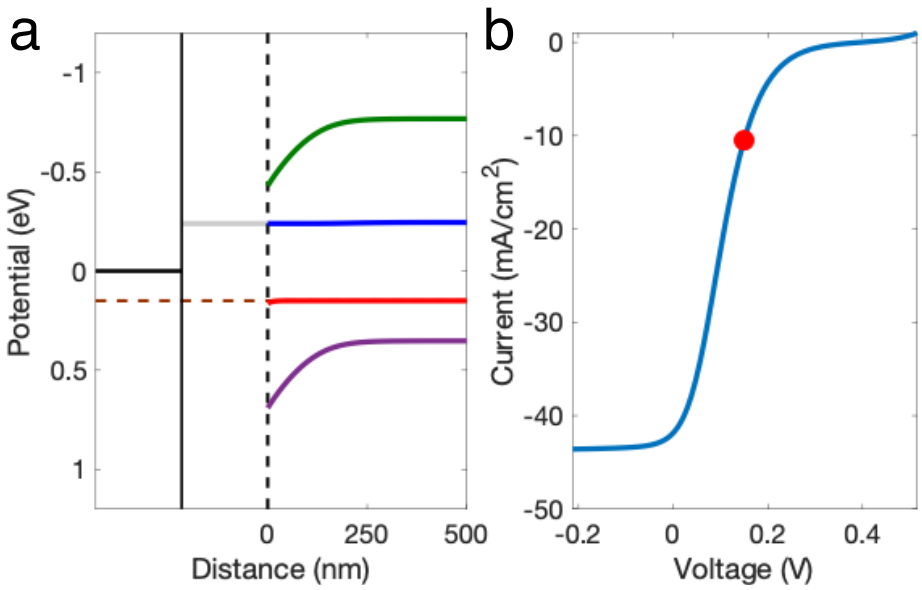

Figure 3.4 | Band diagrams and current voltage relationship calculated by the model for a p-type silicon-like semiconductor. (a) represents a band diagram and (b) represents a modeled current voltage relationship of a photocathode. The red dot in (b) represents -10mA/cm2, which was the current point where the band diagram in (a) was calculated. The green and violet lines are the conduction and valence bands, the blue and red lines represent the electron and hole quasi-Fermi levels, the horizontal black line is the potential of the redox couple in solution, the brown dashed line is the applied potential (with respect to the potential of the redox couple in solution), and the grey line is the electrocatalyst potential. The vertical dashed line marks the insulator layer at the semiconductor-metal boundary.

3.5 Conclusions

The benefit of the model is that multiple physical parameters of the semiconductor can be tuned in order to determine their effect on overall performance. Example tunable variables include the: semiconductor band gap/band positions, electrocatalyst activity, electrocatalyst work function, insulator thickness, insulator energetic barriers, absorption coefficient, etc. The physical parameters and necessary constants used in the model are tabulated below for reference along with a short description. By analyzing the effects of varying design parameters, the model can be leveraged to identify and optimize the most important tunable experimental parameters that affect performance.

Table 3.1 | Modeled Design Parameter Inputs into the Model System

Variable	Description	Value
J_{ocat}	Electrocatalyst exchange current (mA/cm2)	1
E_{vsHER}	Semiconductor valence band edge relative to HER (V)	-0.73
Bg	Semiconductor bandgap (eV)	1.12
ϕ_m	Workfunction of electrocatalyst	4.0-4.4eV
E_{sol}	Redox potential of the solution (eV)	0
N_c	Density of states in the semiconductor for electrons (cm-3)	2.8×10^{19}
N_c	Density of states in the semiconductor for holes (cm-3)	2.65×10^{19}
d	Doping density of the majority charge carrier (cm-3)	1×10^{16}
p_{bulk} or n_{bulk}	Bulk concentration of the majority charge carrier concentration (cm-3) can be electrons or holes for nSi or pSi	1×10^{16}
ϵ	Dielectric constant of the semiconductor	11.9
ϵ_0	Vacuum permittivity (C/Vcm)	8.85×10^{-14}
q	Charge of an electron (C)	1.6×10^{-19}
k_b	Boltzmann constant (J/K)	1.38×10^{-23}
$k_{b,ev}$	Boltzmann constant (eV/K)	8.62×10^{-5}
T	Temperature (K)	298.15
B	Recombination rate coefficient (cm^3S^{-1})	1×10^{-15}
α	Semiconductor optical absorption coefficient (cm^-1)	1×10^5
v_n	Mobility of electrons (cm^2/Vs)	1450
v_p	Mobility of holes (cm^2/Vs)	500
ind	Number of nodes in the semiconductor that will be used in the finite difference calculation for potential and charge carrier conc.	4000
ref	The factor of how much light is not reflected by the semiconductor surface	1

Chapter 4

Tuning the Insulator for Nanoscopic Control of Charge Carrier Fluxes to Improve Photovoltage

4.1 Introduction

A previous chapter discusses the basic physical mechanisms that govern a photoelectrochemical process (Ch. 2). Chapter 3 shows how these systems can be modeled to optimize design parameters that affect device performance. Chapter 4 will discuss an example of a system where an experimentally relevant design parameter—in this case insulator thickness—was tuned in order to improve efficiencies. The model discussed in Ch. 3 was used to elucidate the physical mechanisms that govern performance and guide the design of future experimental systems.

4.2 Improving Efficiencies in Experimental Systems

To maximize efficiencies of experimental photoelectrochemical systems strategies must be developed to (1) increase the total amount of absorbed solar irradiance by the semiconductor[83,95], (2) improve the ability of the semiconductor to harness the absorbed light (improving the quantum efficiency[72,96–98] and photovoltage), and (3) increase the activity of the attached electrocatalyst[12]. Chapter 1 discusses how addressing the first of these challenges is heavily dependent on the choice of the semiconductors, which need to have a band gap of between 1 and 2eV to achieve optimal efficiencies for dual semiconductor systems[83,95]. Almost all semiconductors with the band gaps in this range (Si, GaAs, CdTe, etc.) are not stable under relevant photocatalytic conditions[37]. The

main problem is that under anodic reaction conditions (the O_2 evolving electrodes), these materials are more readily oxidized and therefore degraded than the water reactant. The lack of stability of ideal solar absorbers has been the motivation for the development of MIS structures for photoelectrochemical applications, which use protective oxide layers to enhance stability. Previous reports of experimentally demonstrated insulator-protected photoelectrodes often include a Si semiconductor covered with an Al_2O_3[55–58] and TiO_2[24,50,57,59–61] protective layer onto which a metal electrocatalyst was deposited. In these systems, the choice of the semiconductor, protective layer and electrocatalyst materials impacts the overall efficiencies. In general, it has been recognized that electrocatalysts, in addition to excellent electrocatalytic activity need to have a work function such that the inherent electrocatalyst/semiconductor barrier height is high[8]. This means that for the water oxidation half-reaction (i.e., oxygen evolution reaction, OER), costly noble metal electrocatalysts with high work functions, such as Ir (work function of 5.4-5.8 eV[99]) are desired. For electrocatalysts with acceptable water oxidation activities but poor work function characteristics, such as Ni[100,101] (surface anodized) or NiO_x[27,55] (the work function of Ni is ~5.15 eV[102]), more elaborate structures have been used to achieve high efficiencies. These strategies include (1) forming a bimetallic layer with one metal setting the barrier height of the system and another functioning as the electrocatalyst[58,103], and (2) fabricating a p-n semiconductor junction beneath the insulator layer[37,50,59]. While these strategies can yield efficient photocatalyst systems, the fabrication complexity may increase costs. Additionally, these strategies are not easily implemented in some semiconductor systems, such as Cu_2O[104], that are not conducive to forming efficient p-n heterojunctions.

It has also been argued that in addition to the interface engineering required to optimize the semiconductor-electrocatalyst barrier height discussed above, the insulating protective layer

should be as thin as possible[50]. The reason for this is that the transfer of photo-excited minority charge carriers should not be impeded by the insulating layer. Another study has shown an optimized photovoltage for moderate insulator thicknesses[58]. Both of these studies involved the use of high barrier nSi-Pt or nSi-Ir junctions in order to suppress thermionic emission, which leads to recombination and a loss in photovoltage.

The results discussed in this chapter show that by tuning the thickness of the insulating layer, even systems with moderate inherent barrier heights can achieve high efficiencies. This work demonstrates that the thickness of the insulating protective layer is an important parameter that can be tuned to optimize the behavior of MIS photocatalyst systems, i.e., the thinnest protective layers do not necessarily produce the optimal performance. This is shown by the way of a concrete example that employed the use of n-type Si, a Ni electrocatalyst, and a HfO_2 protective layer as the MIS system for photocatalytic water oxidation. It has been shown previously that the n-Si/Ni system exhibits a moderate barrier height, which limits the photovoltage and therefore the performance[16]. By tuning the thickness of the HfO_2 protective layer the performance of this system is maximized, generating a photovoltage that is 403 mV larger than the n-Si/Ni system without the protective layer and comparable to the highest reported for the similar systems that employ Ir electrocatalysts[60]. This strategy provides an additional way to optimize the performance of MIS photocatalysts, which can be used in place of the above-mentioned p-n junction fabrication strategies. The experimental findings were substantiated with a comprehensive model (discussed in Ch. 3) that elucidates the underlying mechanisms behind photovoltage improvement.

4.3 Experimental Methods for nSi/HfO_2/Ni MIS Fabrication

Layered Ni/HfO_2/Si MIS photoanodes were fabricated as a platform for examining the effects of insulator thickness on photoelectrochemical performance. Moderately doped n-Si (ρ =

1-10 Ω cm) (Silicon Valley Microelectronics) and p-Si (ρ = 1-3 Ω cm) (Silicon Resource Company) was cleaned with Nano-Strip (a commercial piranha solution) for 10 minutes at 60^{o}C and dipped in buffered hydrofluoric acid for 1 minute. Thin (1-3nm) HfO_2 layers were deposited via atomic layer deposition (ALD) on the Si wafers using an Oxford Instruments OpAL Atomic Layer Deposition System. In this process the ALD chamber is pumped down to 25mT and preheated to 275^{o}C. The substrate is exposed to a number of ALD cycles in order to deposit the HfO_2 layer by layer. An ALD cycle consists of (1) a precursor dose of Tetrakis(ethylmethylamino)hafnium (TEMAH) for 800ms followed by a purge, and (2) a dose of H_2O followed by a purge. The pulses were performed at ~250mT. ALD cycles can deposit thin conformal layers of insulating material and the insulator thickness can be increased by increasing the number of ALD cycles. After the ALD process a 7nm Ni layer was deposited on the HfO_2-coated wafers at a rate of 1Å/s at a base pressure of $2x10^{-6}$ Torr using electron beam evaporation. The wafers were diced into 13x13mm squares with a dicing saw.

After fabricating nSi/HfO_2/Ni samples with a varying number ALD cycles (insulator thicknesses), the samples were characterized via scanning transmission electron microscopy (STEM). In order to image cross sections of the samples focused ion milling was performed on a FEI Nova 200 nanolab SEM/FIB. Ion milling was performed in order to cut a cross section out of the sample. An omniprobe was lowered to the sample surface and attached to the sample via a Pt weld. The sample cross section was cut out and attached to a copper TEM half grid with another Pt weld. Ion milling was then used to thin the cross section for TEM imaging. Ultra-high resolution STEM imaging was performed with a 22 cycle sample on a JEOL 3100R05 Double Cs Corrected TEM/STEM to provide a high resolution image of the amorphous ALD layer. Geometric

characterization data in Fig. 4.1 show that the synthesis yields a layered structure consisting of a monocrystalline semiconductor, an amorphous insulator, and a metallic electrocatalyst.

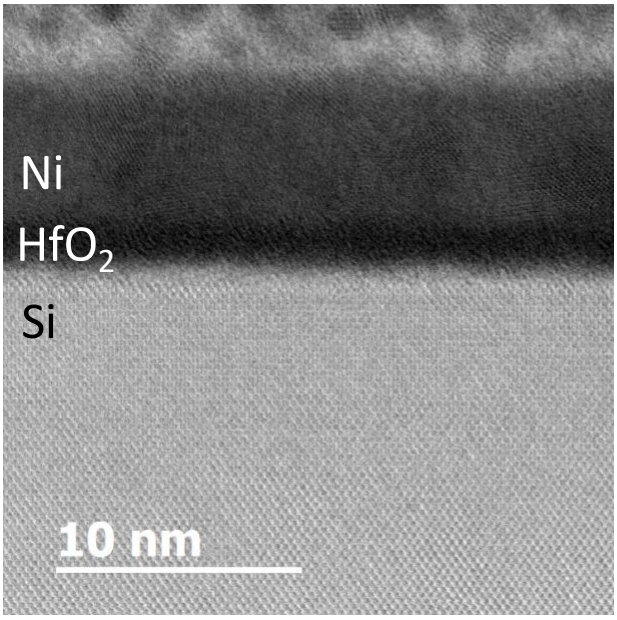

Figure 4.1 | High Resolution Bright Field Image of the n-Si/22cycle HfO_2/7nm Ni sample. Ultra-high resolution STEM imaging was performed with a 22 cycle sample to provide a high resolution image of the amorphous insulator layer.

A JEOL 2100 probe-corrected analytical electron microscope with an accelerating voltage of 100kV was used for insulator thickness measurements and elemental composition characterization, for which STEM and energy-dispersive X-ray spectroscopy (EDS) were used respectively. Figure 4.2a-d show cross-sectional dark field scanning transmission electron micrographs (STEM) of the MIS samples with different HfO_2 thickness. The data in Fig. 4.2e show the energy-dispersive X-ray spectroscopy (EDS) elemental line scan of a representative cross-sectional sample with clearly identifiable components of the layered nanostructures and defined boundaries between the different materials. Insulator thicknesses were measured using IMAGEJ software as the distance between the semiconductor and the HfO_2/Ni boundary (marked by a change in contrast/grain structure). The boundary was verified with EDS elemental mapping and EDS line scans.

Data in Fig. 4.2f show the measured thickness of the HfO_2 layers in the MIS samples as a function of the number of the ALD cycles used in the fabrication process. The data show that on average one ALD step results in 0.1 nm of deposited HfO_2. STEM images of the cross-sectional samples of the layered MIS materials demonstrated that the HfO_2 thickness was uniform for all of the imaged samples. Several additional cross sections were performed at different areas for samples containing the thinnest insulator layer, and there were no detectable pinholes in any of the imaged samples as shown in Fig 4.2. We note that several papers in water splitting literature have reported atomic layer deposition (ALD) of insulator layers in the 1-3 nm range, and no evidence of pinholes has been found for atomic layer deposited TiO_2[24,78] and Al_2O_3[56,58,91]. In fact, ALD is a widely-recognized method to deposit pinhole-free, conformal layers with sub-nanometer precision[105,106]. While attempts were made to completely remove possible SiO_2 layers from the Si semiconductors, it is conceivable that very thin layers of SiO_2 persisted. If they existed their impact on the MIS performance would be uniform across different MIS samples.

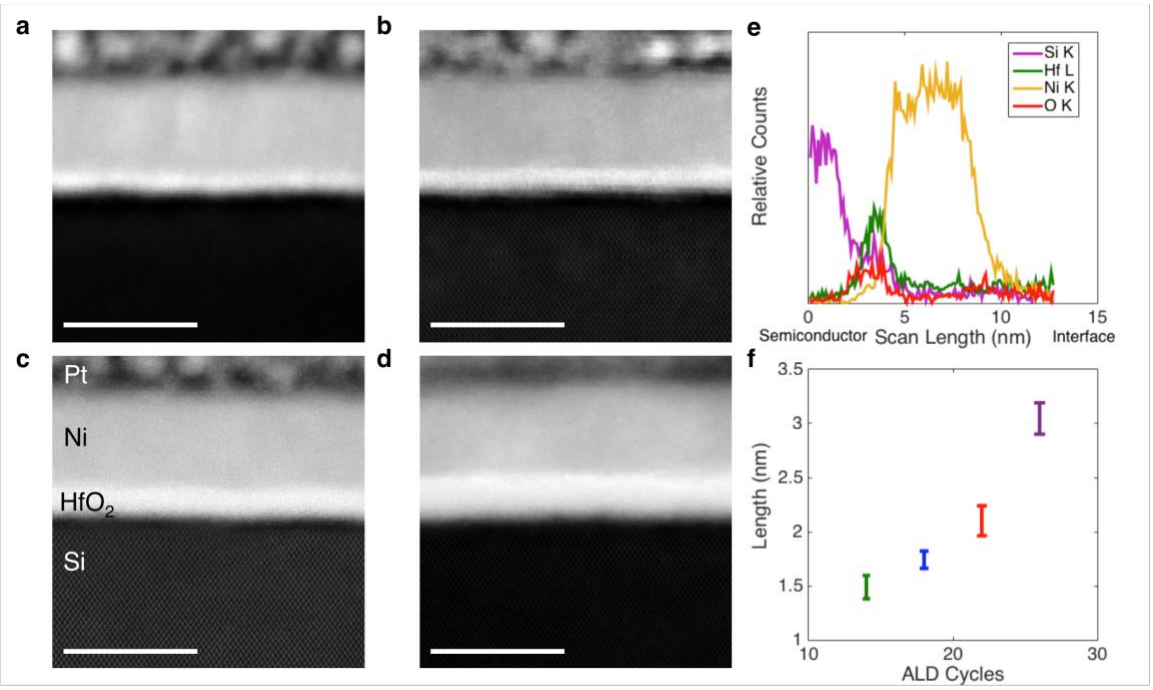

Figure 4.2 | Characterization of n-Si/HfO_2/Ni samples. Cross-sectional STEM images for (**a**) 14 cycles HfO_2, (**b**) 18 cycles HfO_2, (**c**) 22 cycles HfO_2, and (**d**) 26 cycles HfO_2. The layers are labeled in (**c**), and the scale bar represents 10nm. The Pt layer was deposited to protect the Ni layer during cross sectional preparation. (**e**) The energy-dispersive X-ray spectroscopy (EDS) line scan of the n-Si/22c HfO_2/Ni cross-sectional sample. (**f**) HfO_2 thicknesses as a function of the number of the HfO_2 ALD cycles measured from the STEM images. The error bars represent one standard deviation based on ten different points across a sample.

P-type silicon, hafnium oxide, and nickel island samples were also fabricated. Electrocatalytic islands rather than films were used for stability testing. One of the benefits of MIS systems as photoanodes is that the insulator layer can act as both the protective layer as well as govern the energetics of the interface. While studies often examine metal films, which are useful to analyze the interface, their use as the primary protective material would also lead to large parasitic absorption (and could only be used in the bottom absorber of a tandem system[39]). An MIS structure with metal islands rather than metal films reduces parasitic absorption of the electrocatalyst layer. We note that the oxide-metal interfaces of the island structures could also affect electrocatalytic activity and barrier height[107–109]. These structures are characterized by a large direct contact area between the electrolyte and the insulating layer, requiring the insulating material to be stable in highly oxidative, and alkaline environments. Thus far in MIS systems with metal island structures only thick TiO_2 has been shown to protect Si[59] in alkaline environments. In order to determine the viability of HfO_2 as a protective layer, noting that this material has not been used previously as a protective layer, samples consisting of Si, HfO_2, and Ni islands were fabricated (the Ni islands were 3 μm diameter and 5 nm thickness).

For these samples the HfO_2 layer was deposited in the same procedure as the one described above. The HfO_2-coated silicon was then spin coated in a photoresist, SPR 220 (Dow), and baked at 115^{o}C for 90 seconds. The wafers were exposed to light through a mask with a GCA AS200 AutoStep and developed in order to make 3μm diameter holes in the photoresist layer. The wafer

was then subject to an O_2 plasma descum to remove any remaining photoresist residue in the holes. The Ni evaporation procedure was the same as described above. After Ni deposition the wafers were dipped in acetone to lift off the photoresist. A scanning electron micrograph of the nSi/HfO_2/Ni island sample is shown in Fig. 4.3 showing Ni islands with a diameter of 3μm and a 5nm thickness.

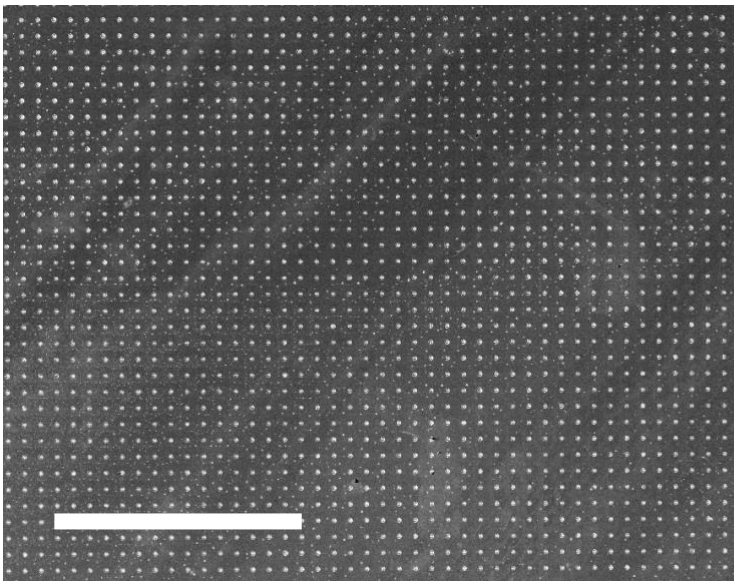

Figure 4.3 | Scanning electron micrograph of the n-Si/HfO_2/Ni island samples. The scale bar represents 300μm. (the Ni islands were 3 μm diameter and 5 nm thickness).

4.4 Electrochemical Methods for nSi/HfO_2/Ni Samples

To evaluate the performance of these materials in the water oxidation reaction, cyclic voltammetry (CV) measurements were performed in a three-electrode setup in 1M KOH. The samples were illuminated with a ~100 mW/cm_2 halogen lamp (mimicking sunlight), the intensity of which was measured with a thermopile detector. P-type control samples were measured in dark. The back contacts of the samples were scratched with a diamond scribe to remove the native oxide and a gallium-indium eutectic was applied to ensure ohmic contact. The back contacts were then pressed against a copper plate. The samples were housed in a 3D printed electrode and exposed to

the light source via a 0.264 cm_2 aperture. An O-ring pressed to the sample surface prevented electrolyte from leaking to the back contact. A Pt counter electrode, and an Hg/HgO reference electrode were used. The scan rate was 100mV/s. Oxygen was bubbled into the electrolyte throughout the experiments. The electrodes were cycled 10 times before measurements to ensure current stability. The following equation was used in order to convert potential from the Hg/HgO reference to RHE at pH 14:

$$V_{RHE} = V_{Hg/HgO} + 0.118 + .0591 \times pH$$

EQ 4.1

Cyclic voltammograms were also performed in a ferri/ferrocyanide solution. The electrolyte was made up of 10mM potassium hexacyanoferrate(II) trihydrate, 10mM potassium hexacyanoferrate(III) (EMD Millipore), and 1M KCl (Fischer Scientific). A Ag/AgCl reference electrode was used.

4.5 Results for the nSi/HfO_2/Ni Photoanodes with Varying Insulator Thickness

Data in Fig. 4.4a show the measured current (reaction rate) as the function of voltage (the potential of majority charge carriers with respect to reversible hydrogen electrode). In these experiments the redox waves prior to the onset of water oxidation correspond to the Ni^{+2}/Ni^{+3} oxidation peak (thick Ni electrocatalysts have been shown to form a non-penetrating surface oxide[100,101]). The data show that the performance improves considerably from 0 to 22 HfO_2 ALD cycles (0 to 2.1 nm) and declines for larger thickness. Data in the inset in Fig 4.4a show the measured HfO_2 thickness-dependent photovoltage for various MIS samples. The photovoltage was defined as the difference between the voltage measured at a current of 1 mA/cm_2 for the illuminated samples and the voltage for the p-Si/Ni control system. The data shows that the photovoltage obtained for the n-Si/Ni system without the HfO_2 protective layer is very low (~76

mV), corroborating the low work function of Ni and a very poor n-Si/Ni barrier height. On the other hand, the photovoltage significantly improves with the introduction of the HfO_2 protective layer, reaching a maximum of 479 mV for the 2.1 nm HfO_2 layer and then dropping for the larger HfO_2 thicknesses. This observed volcano behavior of the photovoltage for the MIS samples as a function of the protective layer thickness suggests that there is an optimal thickness of the insulating layers and that the highest performance is not achieved by the minimum oxide layer thickness. The photovoltage measured for the HfO_2 thickness of 2.1 nm is the highest reported for a thick Ni electrocatalyst on Si[100,101].

To further characterize the behavior of these MIS photocatalyst systems, the samples were tested as photocatalysts for the ferro/ferricyanide redox reaction. This redox reaction is a one-electron transfer process that exhibits no overpotential losses, and therefore it can be used to deconvolute photovoltage generated by the system from the electrochemical overpotential losses, which are significant for the OER kinetics on Ni. Data in Fig. 4.4b show the current-voltage response of the photocatalysts in 10 mM ferri/ferrocyanide and 1M KCl under the 100 mW/cm^2 broadband light source illumination. For this reaction photovoltage is defined as the difference in $E_{1/2}$ between the n-Si/x-HfO_2/Ni and the p-Si/Ni samples, where $E_{1/2}$ is the midpoint voltage between the oxidation and reduction peak potentials. The data is consistent with the OER results indicating that the photovoltage improves significantly as the HfO_2 thickness is increased from 0 to 2.1 nm and declines for larger HfO_2 thickness.

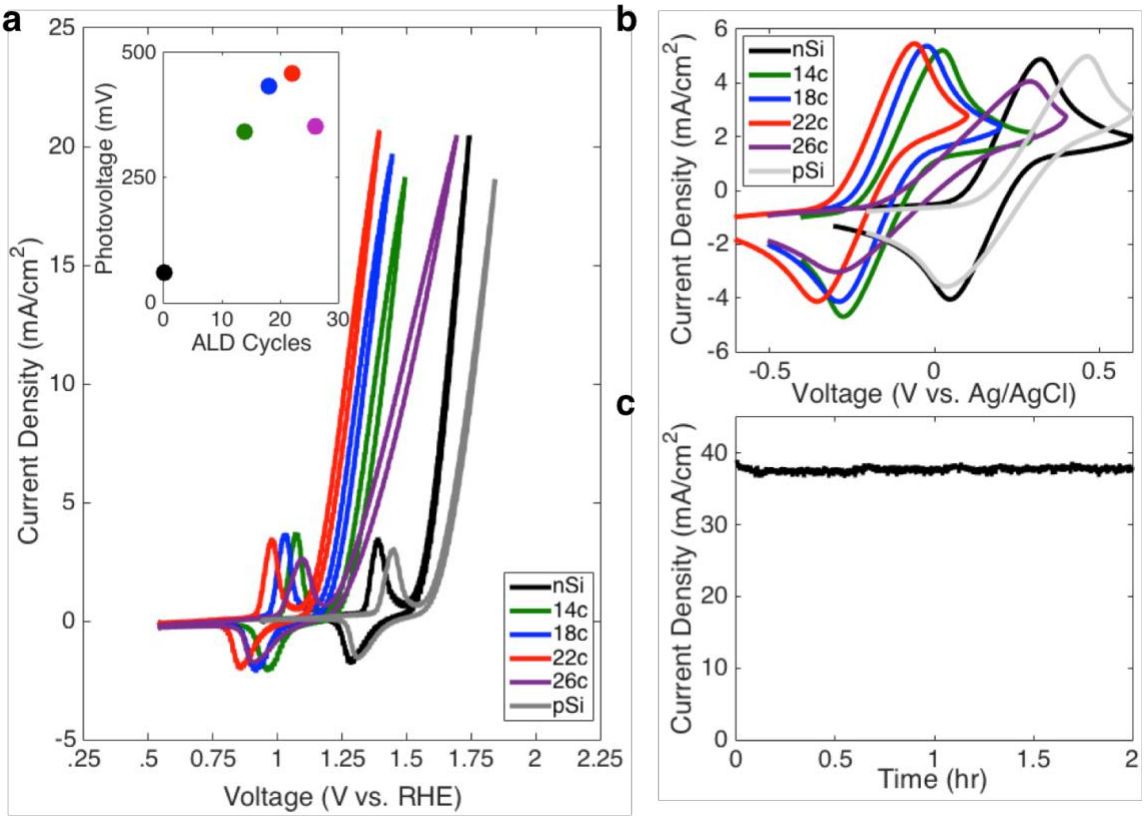

Figure 4.4 | Electrochemical performance of the n-Si/x-HfO_2/7nm Ni samples. a) Current voltage response upon illumination in 1M KOH for increasing HfO_2 thickness. The inset shows the measured photovoltage at 1 mA/cm_2 as a function of the HfO_2 ALD cycle number. From 0-22 ALD cycles (0 – 2.1 nm HfO_2) photovoltage improves, but it decreases for larger HfO_2 thickness. **b**) Cyclic voltammograms performed under illumination in 10mM ferri/ferrocyanide and 1M KCl corroborates that photovoltage is optimized for moderate HfO_2 thickness. **c**) Chronoamperogram for an n-Si/22 cycle HfO_2/Ni island sample shows that the HfO_2 protected n-Si is stable in 1M KOH at a potential of 1.8V vs RHE for 2 hours of operation.

Stability tests were performed with the nSi/HfO_2/Ni island samples using chronoamperometry measurements. The tests were performed with electrocatalytic islands rather than films to determine if the thin HfO_2 insulator was sufficient to behave as a protection layer in MIS systems. Chronoamperometry data in Fig. 4.4c obtained in the photo-limiting current regime (1.8 V vs RHE) show that the current is stable for over 2 hours of continuous operation, indicating that the HfO_2 layer provides a high degree of protection. This is not surprising considering the demonstrated stability of this material under highly oxidizing conditions[110]. The demonstrated

stability also indicates that there are no significant pinholes in the HfO_2 layer, as pinholes would enable direct contact between the electrolyte and the Si resulting in immediate degradation.

4.5 Modeling Insights into the Role of Increasing Insulator Thickness

The data in Fig. 4.4 show that the thickness of the insulating HfO_2 layer can be tuned to maximize the performance of the MIS photocatalysts. To shed light on the observed behavior of the Si/HfO_2/Ni layered photocatalysts, the mathematical model discussed in Ch. 3 was used to model the performance of these systems as a function of the thickness of the insulating layers. In short, numerical methods are used to solve Poisson's equation and charge carrier continuity equations for both charge carriers iteratively to determine potential and charge carrier concentration profiles across an illuminated semiconductor. The Butler-Volmer equation is used to model the rate of the electrocatalytic reaction on Ni. The rate of charge transfer between the Si semiconductor and Ni catalysts through the insulating HfO_2 layer represents a boundary condition to the continuity equation. This important physical parameter was originally described EQ 3.11 and is provided below for reference:

$$J = k_p T_p (p_s - \bar{p}_s) - k_n T_n (n_s - \bar{n}_s) \qquad \text{EQ 3.11}$$

The tunneling probability T_t (assuming a symmetric barrier $T_t = T_n = T_p$) describes the probability that the charge carriers tunnel through the insulator layer and is provided in EQ 4.2.

$$T_t \approx \exp\left(-\propto_t d\sqrt{\phi_t}\right) \qquad \text{EQ 4.2}$$

It has been established that charge transfer rates for tunneling through an oxide insulator—previous studies have shown that HfO_2 transfers charge via a tunneling mechanism—are proportional to tunneling probability as shown in Equation 3.11 and 4.2[68].

The tunneling barrier, ϕ_t, describes as the difference between the band edges of the semiconductor and insulator layer. Zhu et al. experimentally determined a value of ϕ_t for a metal-

HfO_2-Si MIS system to be 1.1 eV[111]. With this value of the tunneling barrier, the tunneling probabilities vary by a few orders of magnitude for the HfO_2 thicknesses explored experimentally in this study. In our simulations, charge transfer rate coefficients of k_n, k_p = 1×10-12 mAcm was taken as a baseline, which corresponds to fast transfer with no insulator[93]. In order to introduce the insulator layer, tunneling probabilities of 1, 1×10-2, 1×10-4, 1×10-6, and 1×10-8 were used. These values correspond to insulator thicknesses of 0nm, 1.3nm, 2.5nm, 3.8nm, and 5.1nm, which can be calculated via Equation 6 by setting $\propto_t = 0.34\text{eV}^{-1/2}\text{Å}^{-1}$ and $\phi_t = 1.1\text{eV}$. This insulator thickness range is similar to the range of HfO_2 thicknesses fabricated experimentally.

Data in Fig. 4.5a shows the calculated current-voltage behavior of the system as a function of the tunneling probability, which as discussed above modifies charge transfer rates. The data in Fig. 4.5a supports the experimental results, showing that the performance of the system is a strong function of the tunneling probability and therefore the thickness of the protective insulating layer with intermediate tunneling probabilities (charge transfer rates) leading to the optimal performance.

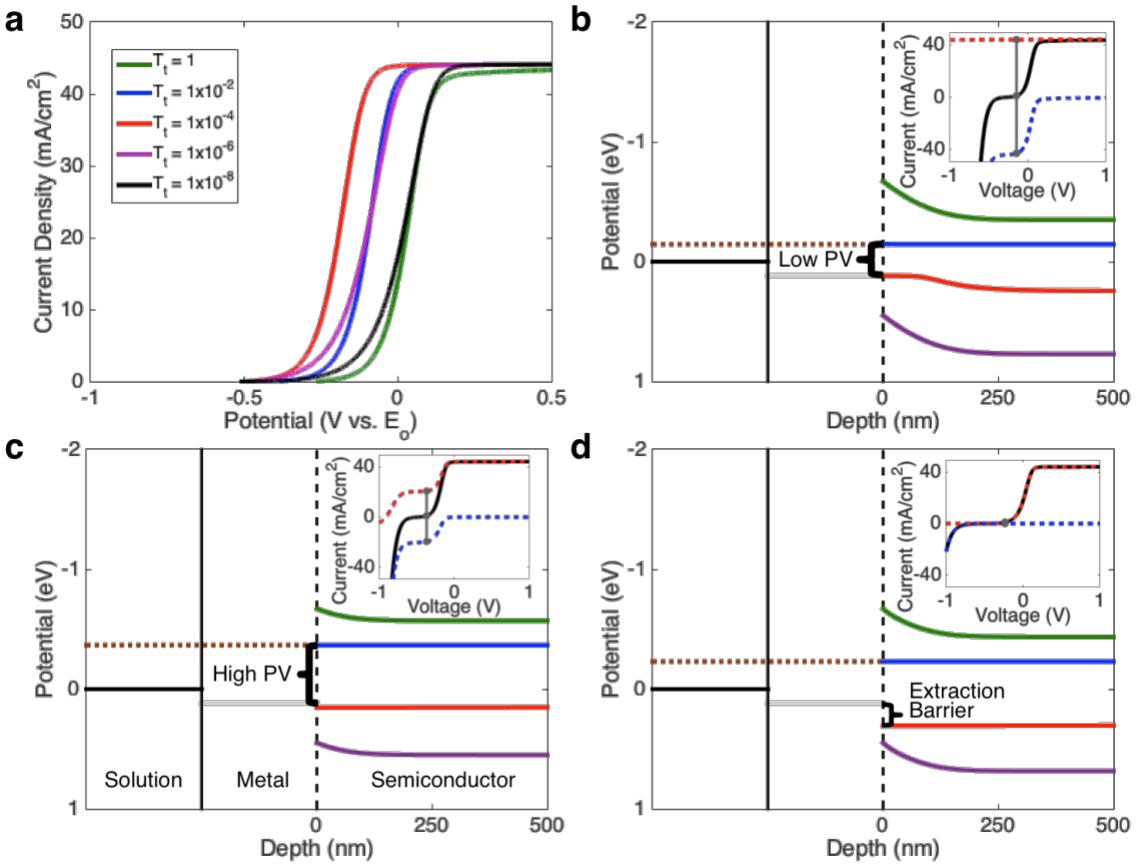

Figure 4.5 | Model results for variable tunneling probabilities. a) Modeled current voltage response shows optimized performance for moderate tunneling probabilities, and therefore charge transfer rates. The potential is measured vs the solution potential E_o, **b-d**) Calculated band diagrams at 1 mA/cm2 for high ($T_t = 1$), moderate ($T_t = 1\times10^{-4}$), and low ($T_t = 1\times10^{-8}$) tunneling probabilities. The green and violet lines are the conduction and valence bands, the blue and red lines represent the electron and hole quasi-Fermi levels, the horizontal black line is the potential of the redox couple in solution, the brown dashed line is the applied potential (with respect to the potential of the redox couple in solution), and the grey line is the electrocatalyst potential. The vertical dashed line marks the insulator layer at the semiconductor-metal boundary. The insets represent the individual charge carrier fluxes as a function of applied potential for each tunneling probability. The blue and red dashed lines represent the electron and hole currents respectively. The black line marks the net current. The gray dot represents the point at 1mA/cm2 net current, where the band diagrams are calculated. The gray vertical lines highlight electron and hole flux overlap leading to recombination, with longer lines indicating higher electron/hole recombination currents.

Analysis of the computed band diagrams in Fig 4.5b-d sheds light on the underlying reasons for the observed thickness-dependent performance of these materials. The representative band diagrams were computed for a current of 1mA/cm2, and therefore a constant voltage of the

Ni electrocatalyst. In the limit of very high tunneling probabilities (Fig. 4.5b), which is consistent with a nonexistent or very low HfO_2 thickness, under illumination the minority charge carriers are rapidly exchanged between the semiconductor and electrocatalyst. This leads to the equilibration in the potential of the minority charge carriers at the semiconductor surface and the electrocatalyst potential. Due to the inherently low barrier height of the Ni/n-Si junction, characterized by similar Fermi level positions, under the conditions of high tunneling probability there is also a significant leakage of the majority charge carriers into the metal electrocatalyst, leading to fast parasitic charge recombination in the metal. As a consequence, these losses lead to low photovoltage and therefore poor performance.

This situation can be improved by designing systems with inherently lower charge transfer rates (Fig. 4.5c). One way to accomplish this is to introduce thin insulating layers between the semiconductor and metal electrocatalyst. While decreasing the tunneling probability decreases the rate of both minority and majority charge carriers, it is possible to have a situation where the minority charge carriers are still at the equilibrium potential (or close to it) with the electrocatalyst (i.e., the exchange rate on the minority charge carriers with the electrocatalyst is still relatively fast), while the leakage current of the majority charge carriers to the electrocatalyst is significantly lowered. This is an ideal scenario as it leads to minimal charge carrier recombination rates and efficient conversion of the minority charge carriers into the reaction rate. After this point, any further decreases to the tunneling probability do not increase the photovoltage (Fig. 4.5d), but rather lead to voltage losses due to the presence of the barrier for the extraction of the minority charge carriers from the semiconductor to the electrocatalyst.

Another way to describe the experimental observations is to focus on the fluxes of majority and minority charge carriers across the semiconductor/metal interfaces (shown as the function of

the applied potential in the insets in Fig. 4.5b-d. At identical current densities (for example, 1 mA/cm2), the net charge carrier fluxes (flux of holes – flux of electrons) through the insulator to the catalyst are identical. However, if the fluxes of individual majority and minority carrier currents are high (much higher than the net reaction rate) there will be large recombination currents in the metal, resulting in low photovoltage. By decreasing both charge carrier currents, the recombination current in the metal can be reduced without sacrificing the total net current. If the tunneling probabilities are decreased too much, the minority charge carrier currents become very small, which means external voltage must be applied in order to achieve the same net current.

This analysis suggests that by engineering nanostructures that can control the fluxes of charge carriers from the semiconductor to the electrocatalyst, the performance of these layered photocatalyst materials can be improved. In this particular case, this was accomplished by tuning the thickness of the insulating protective layer between the electrocatalyst and semiconductor. The enhanced photovoltage can further be explained in terms of a conventional description of a semiconductor/electrocatalyst system, which is often based on using an ideal diode approximation to describe the behavior of a semiconductor light absorber. The illuminated ideal diode equation can be expanded to account for MIS junctions by applying the tunneling probability term[65].

$$J(V) = J_{ph} - J_s exp\left(-\propto_t d\sqrt{\phi_t}\right)\left\{exp\left(\frac{-qV}{kT}\right) - 1\right\};\ J_s = AT^2 exp\left(\frac{-q\phi}{kT}\right) \quad \text{EQ 4.3}$$

In this equation J_s is the reverse saturation current, and the other variables are similar to those used in Equation 2.1. For the case of J(V) = 0, and in the limit of $J_{ph} >> J_s$, Equation 4.3 can be solved for the open circuit voltage (V_{oc}) which is essentially a measure of photovoltage at zero net current.

$$-V_{oc} \approx \frac{kT}{q} ln \frac{J_{ph}}{AT^2} + \phi + \frac{kT}{q} \propto_t d\sqrt{\phi_t} \quad \text{EQ 4.4}$$

Equation 4.4 suggests that, for a given barrier height and photo-limited current density, there should be a linear correlation between the open circuit voltage (i.e., the photovoltage) and the thickness of the insulator layer. Data in Fig. 4.4a and b (including the insets) show the measured photovoltage as a function of the thickness of the HfO_2 layer. The measured linear relationship between the photovoltage and the HfO_2 thickness clearly support our thesis that the photovoltage is tuned by tuning the thickness of the insulator. Notably, Equation 4.3 and 4.4 do not apply for very thick insulator structures since the low tunneling probability results in significant additional losses in potential which are required to force the minority charge carriers through the insulator. These losses are not captured in the ideal diode equation and they are the reasons for the declining performance of the materials for the HfO_2 layers thicker than ~2.1 nm (>22 ALD cycles).

A way to test if insulator thickness tuning is essentially adjusting the open circuit voltage is to measure the flux of majority charge carriers in dark as a function of applied potential. In this case, if the insulator thickness is increased, then lower applied potentials (higher energy of electrons) are required to cross over the barrier into the solution. This effect can be seen from Equation 4.3 by removing the J_{ph} term (i.e., dark operation). This was tested experimentally by monitoring the reduction of the 50/50 ferri/ferrocyanide solution under dark conditions. The measurements were performed in a vigorously stirred solution to avoid the limitations due to the transfer of the reactants from the solution to the surface of the photocatalyst. The CV data in Fig 4.6 show that for larger thicknesses of HfO_2, more negative potentials (higher energy electrons) are required to induce the reduction reaction, which is consistent with the hypothesis.

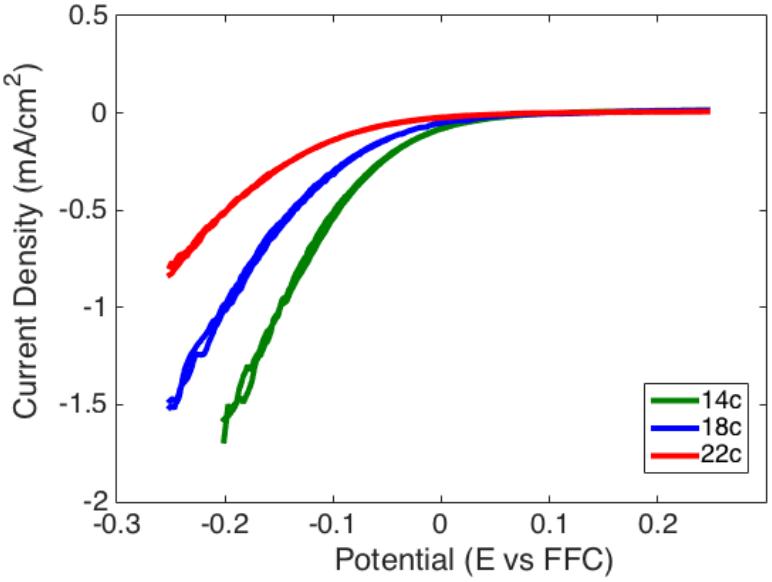

Figure 4.6 | Majority carrier currents for increasing insulator thickness. Current voltage response of the n-Si/HfO_2/Ni electrodes in a vigorously stirred solution of 50/50 ferri/ferrocyanide (FFC) for increasing ALD cycle number. These measurements were performed in dark, causing majority carriers (electrons) to perform the cathodic reaction. For increasing number of ALD cycles (insulator thickness 0 – 2.1 nm HfO_2), more negative potentials are required to induce the FFC reduction reaction indicating that the flux of majority carriers is impeded by the increase in insulator thickness.

4.6 Conclusion

The analysis suggests that by engineering insulating layers between a semiconductor and an electrocatalyst not only improves the stability of photocatalytic systems in water oxidation but also improves the photovoltage obtained by these systems. This was demonstrated by the insulator-induced tuning of the fluxes of charge carriers from the semiconductor to the electrocatalyst, which can minimize charge carrier recombination rates. The observed behavior should apply for all MIS systems characterized by relatively poor inherent barrier heights (low work function difference between the semiconductor and electrocatalyst or poor electronic properties of semiconductor/electrocatalyst interface) that employ insulators that conduct charge carriers via the tunneling mechanism. This strategy can be used to expand the phase space of potentially useful

semiconductor-electrocatalyst pairings for photocatalytic transformations by allowing for the use of active electrocatalysts with poor work function characteristics or for the use of semiconductors that are not conducive for p-n junction fabrication. The MIS systems that have large inherent semiconductor/electrocatalyst barrier heights will not benefit from this approach and these should observe declining photovoltage for increasing insulator thickness as reported previously for the nSi-TiO_2-Ir system[50].

Chapter 5

Determining the Effect of Insulator Tuning on Various Barrier Height Systems Using Bilayer Metals

5.1 Introduction

Maximizing overall solar-to-hydrogen conversion in photoelectrochemical systems involves improving the efficiencies in each of the following steps: (1) absorption of photons by the semiconductor to form electron-hole pairs, (2) migration of charge carriers with enough potential (photovoltage) for the water splitting half reactions, and (3) chemical transformations on electrocatalytic sites. Chapter 1 discusses how the step 1 (solar absorption) can be improved with the use of tandem (dual) semiconductors to capture a larger portion of the solar spectrum compared to single absorber systems[21,83]. Ideal semiconductors for this application have band gaps in the 1-2eV range, which are often unstable in solution and require protection. Protection layer strategies such as the design of MIS structures enables the use of ideal semiconductors to maximize absorption, but additional engineering is required to maximize efficiencies in steps 2 and 3 listed above (maximizing photovoltage and electrocatalytic activity).

For a semiconductor/electrocatalyst system to generate high photovoltage, a high interfacial built-in potential difference between a semiconductor and the attached electrocatalyst is required. This built-in potential is fundamentally governed by the inherent differences in the electronic Fermi levels between the semiconductor and metal (semiconductor Fermi level and metal work function). The built-in potential (V_{bi} in Fig 5.1a) creates an interfacial electric field,

leading to a potential barrier (the barrier height, ϕ_{BH} in Fig 5.1b) for the flow of majority carriers across the interface. Under illumination, this electric field drives energized minority carriers towards the electrocatalyst and majority carriers in the opposite direction, therefore preventing their parasitic recombination. While, in principal, the barrier height is calculated as the difference between the isolated semiconductor valence band edge and the metal Fermi level, various studies have shown that the presence of surface states at the interface causes experimentally measured barrier heights to be significantly lower, thus diminishing generated photovoltage[85,86]. Additionally, many semiconductor-electrocatalyst pairs suffer from an inherently low difference in the respective Fermi level positions and therefore form low barrier heights.

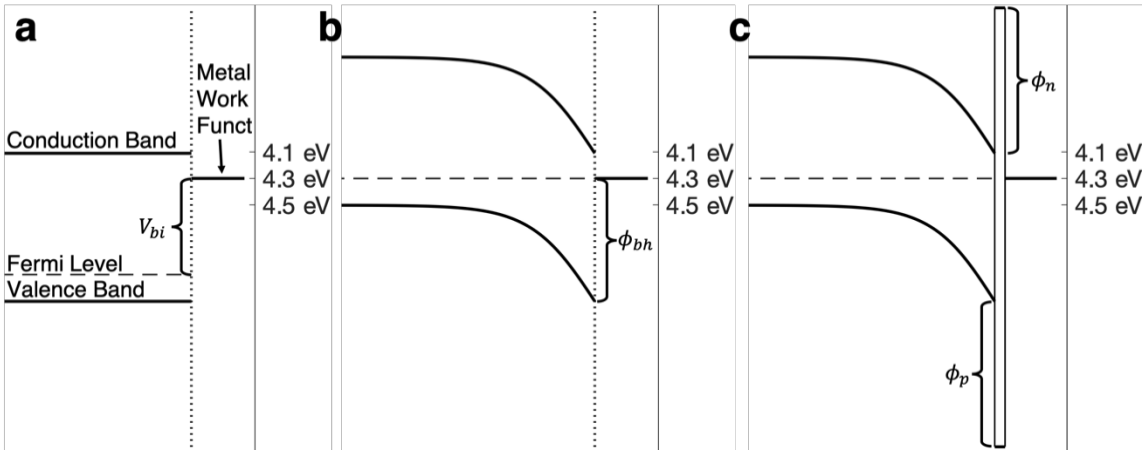

Figure 5.1 | Semiconductor energy band diagrams. a) Schematic of an energy band diagram for a non-interacting p-type semiconductor (silicon) and a low work function metal (4.3eV). **b**) Band diagram schematic of p-type silicon coupled to a low work function metal at equilibrium under no illumination, the potential barrier for majority carriers is called the barrier height ϕ_{BH} and is dependent on the metal work function. **c**) Band diagram of an equilibrated MIS interface. The insulator creates an energetic barrier for electrons and holes (ϕ_n and ϕ_p).

There are multiple approaches proposed to address the problem of a poor barrier height between an electrocatalyst and semiconductor. Methods include the fabrication of a p-n junction within the semiconductor beneath the electrocatalyst layer, which generates large electric fields in the semiconductor that forces the separation of charge carriers[37–39,41–45]. Another approach is to

introduce two metal layers at the semiconductor electrocatalyst junction. In this system the inner metal layer, that is in direct contact with a semiconductor, sets the interfacial built-in potential and has the desired work function while the outer layer serves as an active electrocatalyst[25,56,103,112].

The previous chapter showed another method of improving the performance of a poor barrier system by modulating the thicknesses of a tunnel insulator in an MIS structure. By tuning the thickness of the insulator layer, it was possible to control the flux of charge carriers from the semiconductor to the electrocatalyst and by doing so minimize recombination losses and optimize the generated photovoltage, i.e., the insulator improved the photovoltage of the system that had an inherently poor semiconductor/electrocatalyst barrier height by reducing recombination. In this approach, the insulator changes the semiconductor band energetics by creating an additional barrier for both electrons and holes as shown in Fig 5.1c.

In this chapter experimental and modeling work was performed in order to quantify the extent to which photovoltage can be improved by insulator thickness tuning for various barrier height systems. This was investigated experimentally to determine if insulator thickness tuning could allow a poor barrier system to achieve a performance similar to a high barrier system. The experimental analysis was performed by a way of a concrete example of the H_2 evolution reaction (HER) on an illuminated pSi semiconductor covered with thin layers of the HfO_2 insulator and an additional metal bilayer (Al-Pt and Ti-Pt). In these systems HfO_2 acts as a tunnel insulator, Al and Ti are metals with different work functions that control the inherent interfacial barrier height while Pt is an excellent HER electrocatalyst. Based on the tabulated work function values, Al (work function of ~4.06-4.26eV[113]) is expected to form a higher barrier with pSi compared to Ti (work function of ~4.33eV[114]). By modulating the insulator thickness a photovoltage of 514mV for Ti-Pt and 517mV for Al-Pt samples was achieved, which is among the highest reported for p-type

silicon (pSi)[37]. Insulator tuning was critical to enable the performance of the poor barrier system (pSi-HfO_2-Ti-Pt) to approach that of the higher barrier system (pSi-HfO_2-Al-Pt). The underlying physical mechanisms of the systems were investigated with the comprehensive mathematical model discussed in Ch. 3. The modeling results lead a number of general conclusions that quantify the expected impact of insulator thickness on the performance of the MIS photoelectrocatalysts.

5.2 Fabrication Methods for the pSi-HfO_2-Al-Pt and pSi-HfO_2-Ti-Pt Samples

The experimental system consisted of pSi covered with an HfO_2 insulator layer of varying thickness, which transports charge between semiconductor and electrocatalyst via a tunneling mechanism[111,115]. The HfO_2 was deposited with atomic layer deposition (ALD) and the thickness was varied by modifying the number of ALD cycles. Prior to atomic layer deposition, 10-20 Ω-cm pSi wafers (Silicon Valley Microelectronics) were cleaned in Nano-Strip (a commercial Piranha solution) and dipped for 2 min in BHF to remove the native oxide layer. Cleaned wafers were taken directly to a Cambridge Nanotech Fiji Atomic Layer Deposition tool and placed under vacuum. In the ALD process the wafers were heated to 250C_o for 900s. Tetrakis(dimethylamino)hafnium (TDMAH) was pulsed as the hafnium precursor followed by a pulse of water vapor. After the ALD process the HfO_2-coated pSi was covered with two metal layers. The bilayer metals were deposited in an Angstrom Engineering Evovac Evaporator. One system deposited Al followed by Pt, and the other system deposited Ti followed by Pt. The depositions were performed at a pressure of $4x10^{-6}$ torr and at a rate of 1Å/s. Each metal film was 5nm thick, so each bilayer film had a total metal thickness of 10nm. The samples were then diced into 13x13mm squares.

To characterize the fabricated materials scanning transmission electron microscopy (STEM) were performed on cross-sections of the pSi-HfO_2-Al-Pt and pSi-HfO_2-Ti-Pt samples.

Cross-sectional samples were prepared using an FEI Nova 200 Nanolab SEM/FIB. STEM imaging was performed on a JEOL 2100 Probe-Corrected Analytical Electron Microscope. Representative micrographs of pSi-HfO_2-Al-Pt and pSi-HfO_2-Ti-Pt samples are shown Fig. 5.2a and 5.2b respectively. The STEM images show well-defined layers of the pSi semiconductor, an amorphous HfO_2 insulator, and metal bilayers. By taking cross-sections of additional samples, the relationship between the insulator thickness and the number of ALD cycles can be characterized. Insulator thicknesses were measured using IMAGEJ software at points throughout the cross-sectional samples. This data is presented in Fig 5.2c and d for the pSi-HfO_2-Al-Pt and pSi-HfO_2-Ti-Pt samples respectively, the standard deviation reported in Fig. 5.2 represents thickness variation in the cross-sectional samples.

For each insulator thickness, the samples that were imaged and used in electrochemical experiments were derived from the same wafer (though different wafers were used for each metal bilayer system). Previous research involving the atomic layer deposition of insulators on monocrystalline Si wafers has shown an insulator thickness variation of ~0.1nm throughout the wafer[78], which would indicate that the thickness reported in Fig 5.2 are representative of all experimental samples.

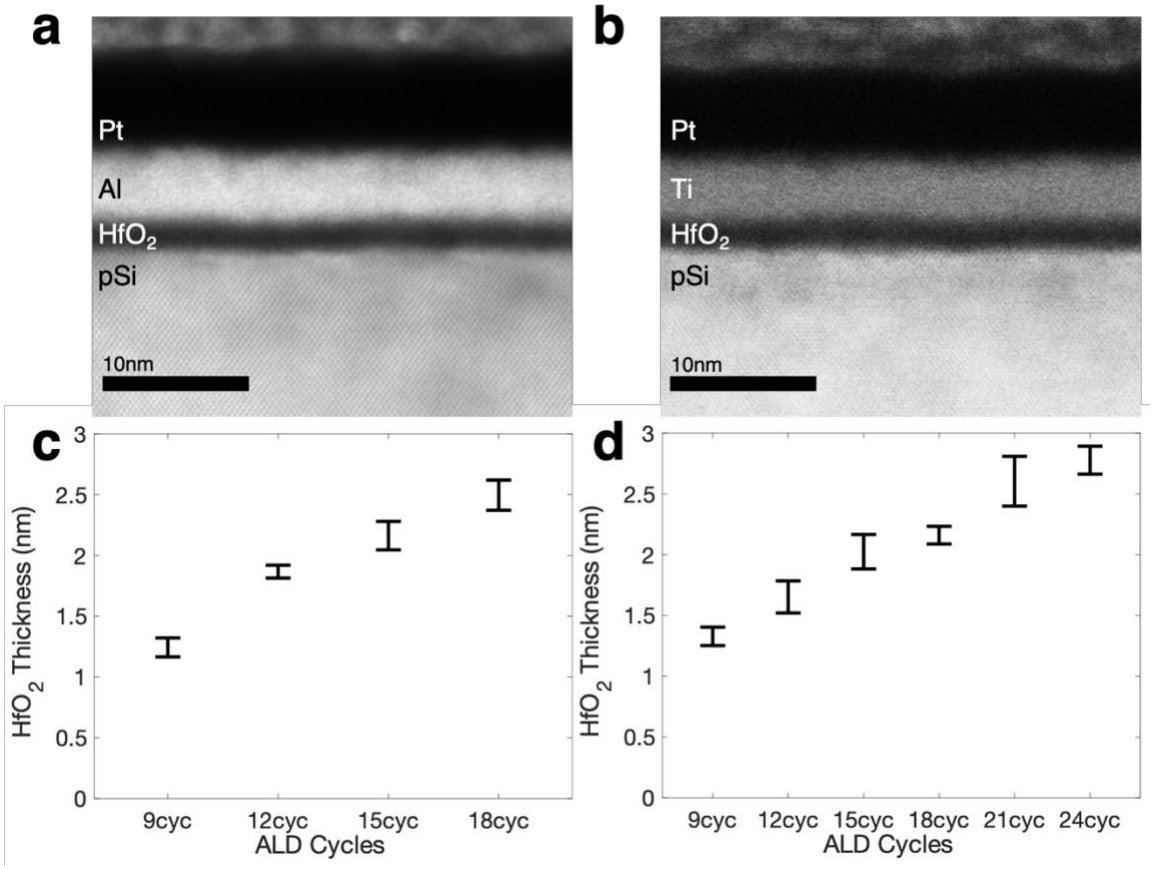

Figure 5.2 | STEM cross-sectional micrographs and insulator thicknesses of the photocathode systems. a) A STEM cross-section of the pSi-HfO_2-Al-Pt sample with 15 ALD cycles. **b**) A STEM cross-section of the pSi-HfO_2-Ti-Pt sample with 15 ALD cycles **c**) The insulator thickness-to-ALD cycle relationship for the pSi-HfO_2-Al-Pt samples. **d**) The insulator thickness-to-ALD cycle relationship for the pSi-HfO_2-Ti-Pt samples.

5.3 Electrochemical Methods for the pSi-HfO_2-Al-Pt and pSi-HfO_2-Ti-Pt Samples

The pSi-HfO_2-Ti-Pt and pSi-HfO_2-Al-Pt electrodes were tested in a three-electrode photoelectrochemical for the HER to determine the effect of the HfO_2 insulator thickness on the generated photovoltage. The samples were housed in a custom 3D printed photocathode. The back contact was scratched with a SiC scribe to remove native oxide and an InGa eutectic was brushed on the samples before being pressed against a copper plate for Ohmic contact. The front contact was exposed to electrolyte through an O-ring. The electrolyte consisted of 1M perchloric acid with H_2 bubbling into the electrolyte throughout the experiments. The samples were exposed to light

through a 0.264 cm_2 aperture and illuminated with a halogen lamp at an intensity of 100mW/cm_2 (~1 sun). A Pt wire counter electrode and an Hg/$HgSO_4$ reference electrode was used. The following equation was used to convert the reference potential from Hg/$HgSO_4$ to RHE.

$$(V\ vs\ RHE) = (V\ vs\ Hg/HgSO_4) + 0.65 + 0.0591 \times pH \qquad \text{EQ 5.1}$$

Electrochemical Mott-Schottky measurements were also performed under no illumination. For these experiments the electrolyte consisted of 10mM ferri/ferrocyanide and 1M KCl. A Pt wire was used as the reference/counter electrode. For the Mott-Schottky tests the voltage was modulated at an amplitude of 10mV and a frequency of 7-25kHz at various set potentials, and the capacitive and resistive components of the impedance were measured.

5.4 Electrochemical Performance for the Metal Bilayer Photocathode Systems

Fig 5.3 shows linear sweep voltammograms generated by the two photoelectrocatalyst systems for various HfO_2 thicknesses. In this work photovoltage was defined as the open circuit potential "V_{oc}" (the point where current density crosses zero) and measured between the working photocathode and 0 V vs RHE (corroborated by measuring the hydrogen evolution potential for a Pt wire). The data in Figure 5.3 show that for systems that do not contain the HfO_2 insulator, the Al-containing sample achieves a higher V_{oc} (285mV) and therefore a higher photovoltage compared to the Ti-containing sample (167mV). While both of these samples likely suffer from a high degree of Fermi level pinning associated with a direct metal-silicon contact, the larger photovoltage generated by the pSi-Al samples implies that they have a higher inherent barrier height compared to the pSi-Ti samples. This result is not unexpected considering that Al has an inherently lower work function than Ti by ~70-270meV[113,114]. The difference in the barrier heights between the pSi-HfO_2-Al-Pt and pSi-HfO_2-Ti-Pt systems was corroborated by a series of Mott-

Schottky experiments described in the Section 5.8, where the median barrier height for the Al-containing samples was ~100mV higher than the Ti-containing samples.

The data in Fig 5.3 also show that the presence of thin HfO_2 insulator layers improves the performance of both photoelectrocatalysts dramatically. For the pSi-HfO_2-Al-Pt electrodes, V_{oc} improves with an increasing HfO_2 insulator thickness from 0 to 1.9nm to a maximum of 517mV. After this point increasing insulator thickness decreases the generated photovoltage. This decrease is caused by impediments to minority carrier transport due to an increasing resistance to the charge carrier tunneling. Interestingly, the data also show that the insulator thickness tuning has an even stronger effect on the pSi-HfO_2-Ti-Pt system compared to the pSi-HfO_2-Al-Pt system. In this system, the V_{oc} increases with insulator thickness up to 2.6 nm, after which it starts declining. The V_{oc} of the optimized pSi-HfO_2-Ti-Pt sample was nearly identical to the Al-Pt sample.

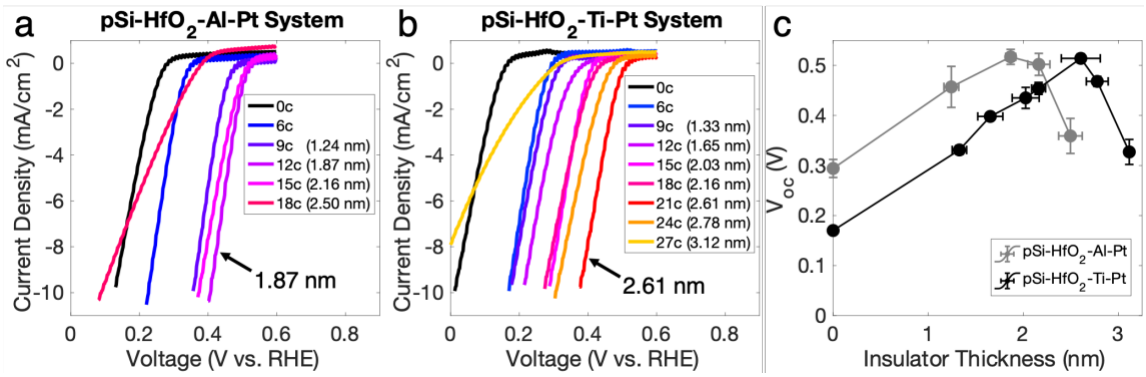

Figure 5.3 | Electrochemical performance of the photocathodes in light-driven HER. a-b) Linear sweep voltammograms of the pSi-HfO_2-Al-Pt and pSi-HfO_2-Ti-Pt electrodes at various insulator thicknesses. **a)** The photovoltage of the pSi-HfO_2-Al-Pt samples improves with insulator thickness up to 1.9nm and decreases thereafter. The photovoltage for the highest performing insulator thickness is 517mV. **b)** The pSi-HfO_2-Ti-Pt samples show improving photovoltage up to 2.6nm after which it decreases. The photovoltage for the highest performing insulator thickness is 514mV. **c)** V_{oc} for the pSi-HfO_2-Al-Pt and pSi-HfO_2-Ti-Pt samples are plotted as a function of increasing insulator thickness.

The data in Figure 5.3 show that while both metal bilayer systems (Al-Pt and Ti-Pt) benefit from the insulator thickness tuning, the performance of the system with a moderate barrier (pSi-

HfO_2-Ti-Pt) improves to a greater extent than the performance of the system with an inherently higher barrier (pSi-HfO_2-Al-Pt). The data show that the tuning of insulator thickness is able to improve the performance of a fundamentally poor barrier system so that it matches the optimized performance of the system with an inherently superior barrier height.

5.5 Modeling Insights in How Insulator Tuning Affects Various Barrier Height Systems

To further investigate the behavior of these systems the mathematical model discussed in Ch. 3 was used to describe the underlying physical processes taking place on layered MIS photoelectrocatalysts. In short, electrochemical reaction rates on the electrocatalyst is described by the Butler-Volmer equation. This determines the electric potential required for the electrocatalyst (in this case the top layer of Pt) to reach a specific current. The model captures the interaction of light with a semiconductor by solving Poisson's equation (which governs the semiconductor electrostatics) and charge carrier continuity equations for both charge carriers (electrons and holes). The boundary condition for the flux of charge carriers between the semiconductor and electrocatalyst is described using the following equations (combination of EQ 2.2, 2.3, and 3.11)[63,65,68,93]:

$$J_p = k_p(p_s - \bar{p}_s)exp\,(-\alpha d\sqrt{\phi_p});\; J_n = k_n(n_s - \bar{n}_s)exp\,(-\alpha d\sqrt{\phi_n}) \qquad \text{EQ 5.2}$$

The exponential terms represent the tunneling probabilities through the insulator for electrons and holes, which are dependent on a constant ($\propto$), insulator thickness (d), and the semiconductor-insulator energetic barrier for electrons and holes, (ϕ_n) and (ϕ_p), which are depicted in Fig 1c. Previous studies using HfO_2 films on silicon have shown a ϕ_n of 1.1eV[111]. This work assumes a symmetric barrier i.e. $\phi_n = \phi_p$, though the degree of symmetry is the subject of future studies. The model was used to determine the potential and charge carrier concentration profiles through

the semiconductor, which can be used to calculate the current-voltage relationship (i.e. the performance) of an MIS system.

By modifying physical design parameters of the system in the model, we can determine their effect on the overall performance. For this analysis the specific variables that were investigated were (1) inner metal effective work function (which adjusts the barrier height) and (2) insulator thickness. The insulator thickness (d) impacts charge carrier fluxes by exponentially decreasing the tunneling probability term (EQ 5.2). The effective inner metal work function directly affects $\bar{n}_s$ and $\bar{p}_s$, the semiconductor (interfacial) surface carrier concentrations in equilibrium in dark, as shown in the following equation[63,93]:

$$\bar{n}_s = n_{bulk} exp\left[\frac{-q(\phi_m - \phi_s)}{k_b T}\right];\ \bar{p}_s = p_{bulk} exp\left[\frac{q(\phi_m - \phi_s)}{k_b T}\right] \qquad \text{EQ 5.3}$$

n_{bulk} and p_{bulk} are the electron and hole concentrations in the bulk of the semiconductor, ϕ_m is the effective work function of the inner metal, and ϕ_s is the isolated semiconductor Fermi level. EQ 5.3 essentially captures the change in barrier height caused by the use of inner metals with different work functions. The terminology "effective work function" is used since, as discussed above, Schottky-based junctions often show a lower barrier height than expected (given the metal work function) due to imperfections at the interface.

To illustrate how these variables affect the performance, the dependence of increasing insulator thickness on V_{oc} was modeled for systems with different effective inner metal work functions. The data in Fig 5.4a show the modeled behavior of photoelectrocatalysts with inner metal effective work functions ranging from 4.1 to 4.5 eV. In the limit of a very low work function (in this case ~ 4.1eV), V_{oc} is high regardless of insulator thickness. (This analysis does not address performance losses at higher currents, where relatively high thickness insulators lead to minority charge carrier transport resistance losses). In these systems, due to an inherently high barrier

height, the open-circuit voltage cannot be improved significantly by the introduction of the insulator as it is already close to the maximum V_{oc} the semiconductor can generate. The data in Figure 5.4a show that systems with moderate work functions (4.2-4.4eV) can reach the near-maximum photovoltage that the system can provide by properly tuning the insulator thickness. Finally, the data also show that for inner metals with very poor work function, ≥4.5eV, the inherently poor performance cannot be completely overcome by an introduction of insulators due to high recombination losses for any insulator thickness.

The modeling results shed light on some of the performance differences between the Al-Pt and Ti-Pt bilayer systems. The data in Fig 5.4a show that high barrier systems (work functions <4.3eV) reach near-maximum open-circuit voltage at lower insulator thicknesses compared to moderate barrier systems (work functions >4.3eV). This is consistent with the experimental results which are also shown in Fig 5.4a (labelled at distinct data points) for comparison, where the Al-Pt samples show an optimized performance at an HfO_2 thickness of 1.9nm, while the Ti-Pt samples show optimal performance at 2.6nm. For very thick insulators, the model cannot be applied to experimental systems, where charge carriers no longer transfer via a direct tunneling mechanism.

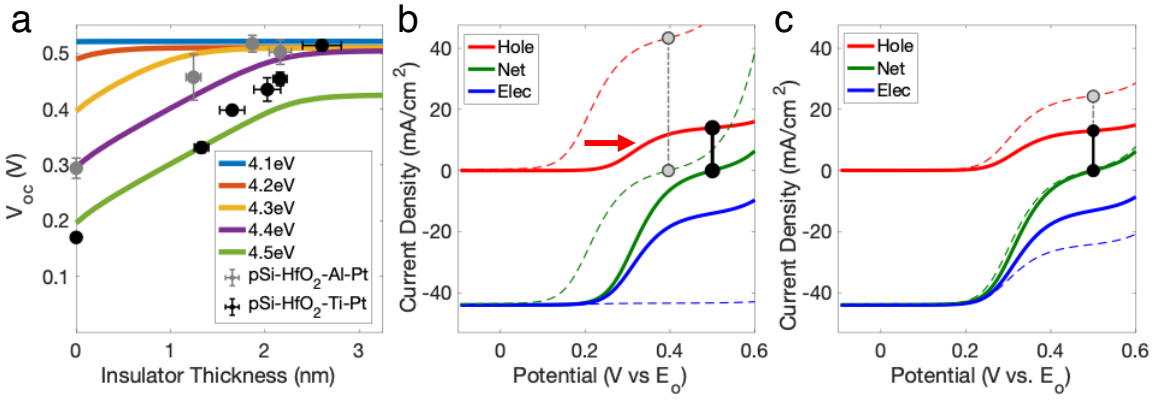

Figure 5.4 | Modeled open-circuit voltage V_{oc} and charge carrier flux diagrams for a pSi-HfO_2-metal system. a) The modeled V_{oc} as a function of insulator thickness for MIS systems with various effective metal work functions. The experimental results of the pSi-HfO_2-Al-Pt and pSi-HfO_2-Ti-Pt electrodes are also provided for comparison. **b-c**) Individual charge carrier fluxes for (**b**) a low barrier (high effective metal work function of 4.3eV) and (**c**) a high barrier (low

effective metal work function of 4.2eV). The red, green, and blue lines represent hole, net, and electron currents respectively. The dashed lines are calculated for a zero-thickness insulator, while the solid lines represent an insulator thickness that provides a near optimum V_{oc} of 500mV. For (**b**) a 1.3nm insulator raises V_{oc} from 400mV to 500mV. For (**c**) an insulator of 0.26nm raises V_{oc} from 490 to 500mV. The applied voltage is referenced vs the solution redox potential, E_o. The gray and black vertical lines indicate majority carrier currents at V_{oc} for the zero-thickness and optimized cases respectively, which lead directly to recombination.

To determine the underlying factors that govern the relationships between the insulator thickness and V_{oc}, the impact of insulator thickness on the fluxes of minority (electrons) and majority (holes) charge carriers was investigated. Fig 5.4b shows the charge carrier fluxes for a MIS system with a lower inherent barrier height (the inner metal work function of 4.3 eV). The dashed lines show the fluxes of individual charge carriers calculated for an unoptimized case (zero-insulator thickness), while solid shows the fluxes for an optimized insulator thickness case (insulator thickness that lead to a near maximum V_{oc} at 500mV). The data show that for a zero-thickness insulator there are high fluxes for both charge carriers at open-circuit voltage (400mV). The high majority carrier current is caused by a smaller electric field driving majority carriers away from the interface (i.e., $\bar{p}_s$ from EQ 5.3 is low resulting in a high J_p from EQ 5.2). In this case, essentially the band bending in the semiconductor is small. The high flux of majority carriers leads to a high degree of the electron-hole recombination (depicted by the gray line in Fig 5.4b) at V_{oc}. By introducing the insulator and tuning its thickness, the losses due to the electron-hole recombination in the electrocatalyst are minimized. This is accomplished by creating an additional barrier for the flow of charge between the semiconductor and electrocatalyst (i.e. the energetic barrier of the insulator) whose thickness allows for the tuning of the flow of charge carriers. The data in Fig 5.4c shows that for this case, an insulator thickness of 1.3nm results near maximum photovoltage at 500mV.

Fig 5.4c shows the charge carrier fluxes for a higher barrier system (low effective work function metal, 4.2 eV). For this system the zero-insulator thickness case (dashed lines) already has very low majority carrier fluxes due to a high electric field. This leads to a high V_{oc} of 490mV. These electrodes, with inherently desirable barrier heights require lower insulator thicknesses (0.26nm) to minimize majority carrier recombination and reach the maximum V_{oc} of 500mV.

5.6 Mott-Schottky Analysis

To support these results a series of Mott-Schottky tests were performed to measure the barrier heights of the experimental pSi-HfO_2-Al-Pt and pSi-HfO_2-Ti-Pt systems in order to corroborate that the Al containing samples have a higher barrier than the Ti containing samples. While it is expected that a pSi-Al based junction would have a higher barrier height than a pSi-Ti based junction, various non-idealities can affect this. For instance, surface states could lead to Fermi level pinning, or midgap states within the insulator could lead to the formation of a direct junction between the semiconductor and insulator. The basis of this technique is to measure the capacitance of the system at various set potentials. By assuming the dominant capacitive and resistive components of the system occur in the space charge region of the semiconductor, one can assume that the electrochemical system is directly analogous to the equivalent circuit in Fig 5.5a. The Mott-Schottky equation (EQ 5.4) can be applied to determine the flat band potential V_{bi} in Fig 1a, which is the potential required flatten the conduction and valence bands. This can be used to calculate the barrier height of the system (EQ 5.5).

$$C^{-2} = \frac{2}{qA^2\varepsilon N_D}\left(V_{bi} + V - \frac{k_B T}{q}\right) \qquad \text{EQ 5.4}$$

$$\phi_{BH} = k_b T \ln\frac{N_D}{N_v} + V_{bi} \qquad \text{EQ 5.5}$$

where C is the capacitance of the system and N_D is the doping density (determined by the Si resistivity), and N_v is the Si valence band density of states. Since the output of a typical Mott-Schottky test is one capacitive and one resistive component, the equivalent circuit in Fig. 5.5a is assumed to be equivalent to a resistor/capacitor in series or in parallel[116] (Fig. 5.5b or Fig. 5.5c).

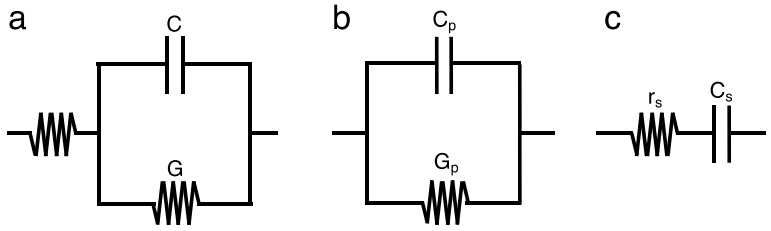

Figure 5.5 | Equivalent circuits for Mott-Schottky analysis. (**a**) represents an equivalent circuit for an electrochemical system assuming the dominant capacitive and resistive components occur in the space charge region of the semiconductor. (**b**) represents a resister/capacitor in parallel and (**c**) represents a resister/capacitor circuit in series.

In Fig 5.5 C and G represents the capacitance and conductance of the equivalent circuit of an electrochemical system, C_p and G_p and represents capacitance/conductance assuming a parallel system, and C_s and r_s are the capacitance/resistance of a circuit assuming a system in series. The true capacitance of the system can be shown to fit the following relations[116]: $C_s > C > C_p$ and $C_s = C_p(1 + G_p^2/\omega^2 C_p^2)$ where $C_s = C_p$ if $G_p^2/\omega^2 C_p^2 \ll 1$. An accurate measure of $1/C^2$ used in the Mott Schottky equation should not vary with frequency and $C_s = C_p$. In this work C_s and C_p of the pSi-HfO_2-Al-Pt and pSi-HfO_2-Ti-Pt systems were relatively close and V_{bi} was estimated from the mean, which did not appear to be frequency dependent. The error bars in Fig. 5.8 correspond to the range between C_s and C_p. Example Mott-Schottky plots of the various bilayer samples are shown below in Fig 5.6 and Fig 5.7 for the pSi-HfO_2-Al-Pt and pSi-HfO_2-Ti-Pt systems respectively.

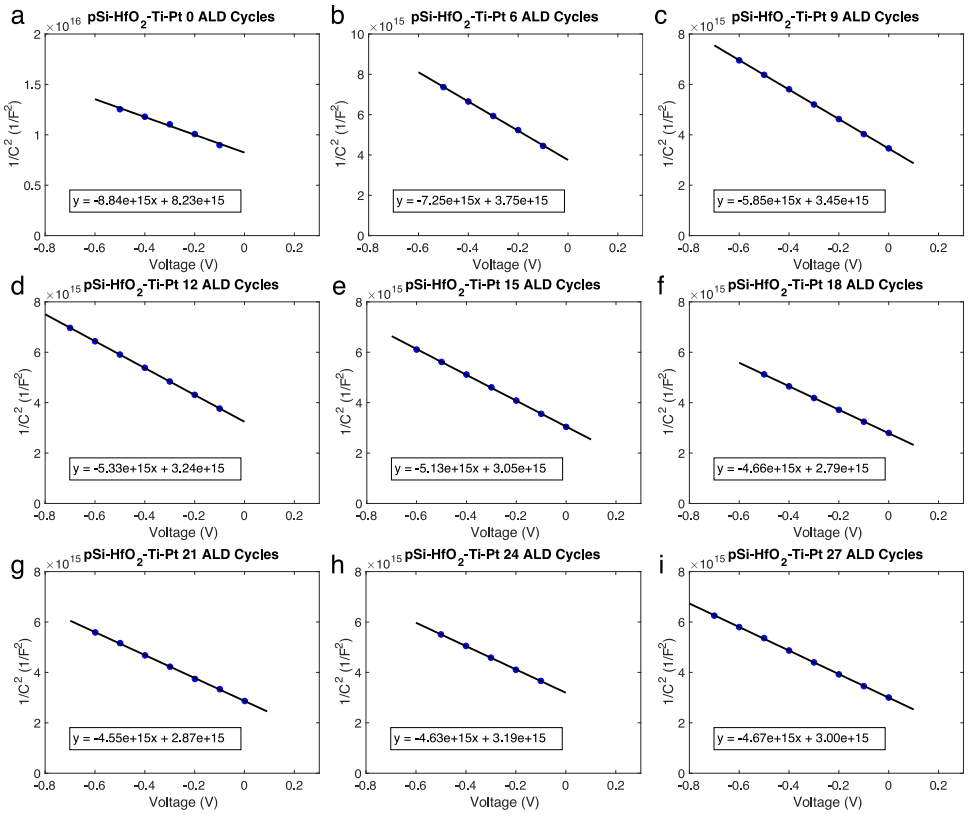

Figure 5.6 | Mott-Schottky plots of the pSi-HfO2-Ti-Pt system for various insulator thicknesses. Mott-Schottky plots for the pSi-HfO2-Ti-Pt samples with plots for (**a**) 0, (**b**) 6, (**c**) 9, (**d**) 12, (**e**) 15, (**f**) 18, (**g**) 21, (**h**) 24, and (**i**) 27 ALD cycles.

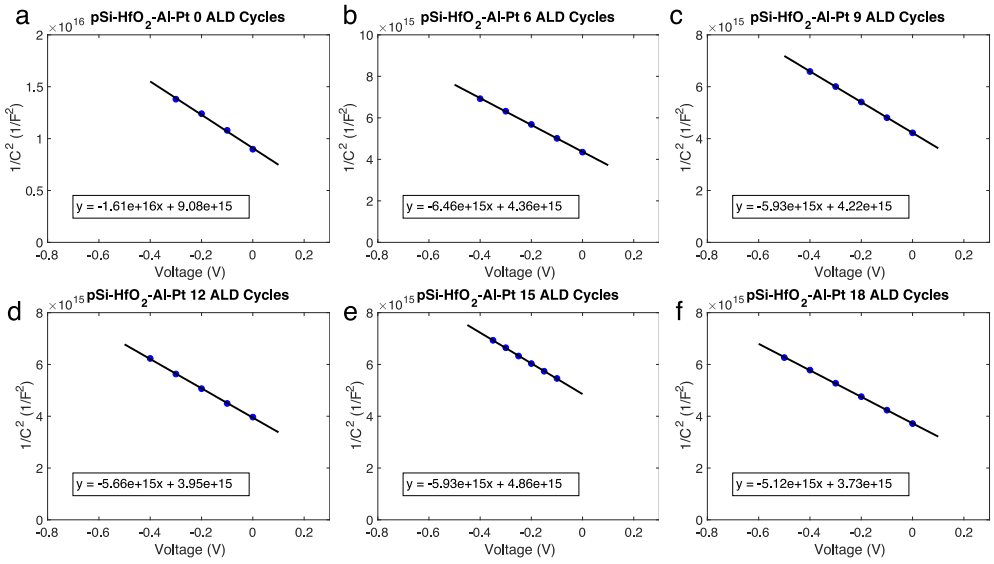

Figure 5.7 | Mott-Schottky plots of the pSi-HfO2-Al-Pt system for various insulator thicknesses. Mott-Schottky plots for the pSi-HfO2-Al-Pt samples with (**a**) 0, (**b**) 6, (**c**) 9, (**d**) 12, (**e**) 15, and (**f**) 18 ALD cycles.

In Fig 5.8 the barrier heights for the Al-containing samples (median 0.97eV) was ~100meV larger than the barrier heights for the Ti-containing samples (median 0.86eV). The barrier heights do not appear to vary significantly with insulator thickness. The data corroborates the results in the main manuscript, which suggest that the inner metal (Al and Ti) plays a fundamental role in setting the barrier height of the electrodes.

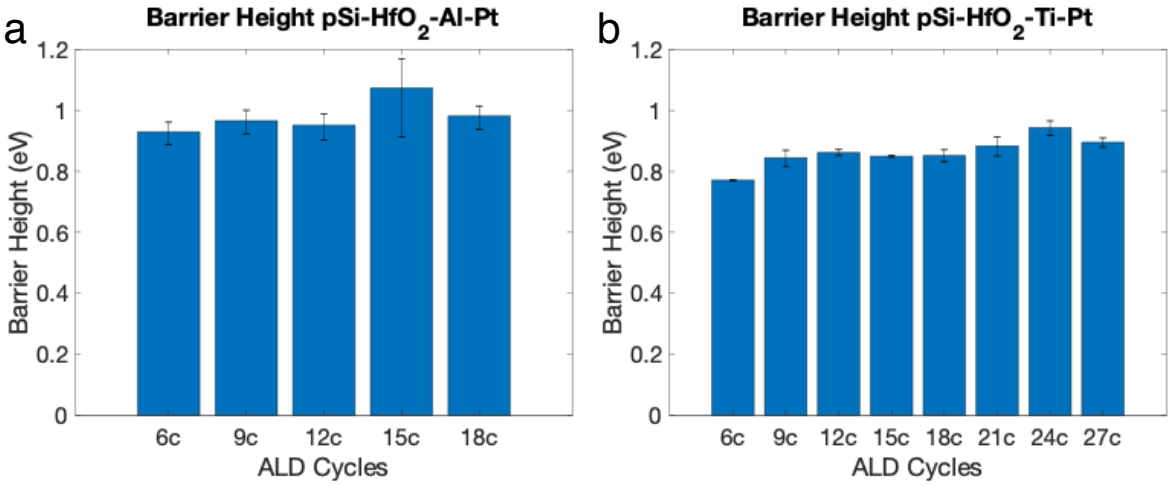

Figure 5.8 | Barrier heights for the (a) pSi-HfO2-Al-Pt and (b) pSi-HfO2-Ti-Pt systems. The barrier heights for the Al-containing samples (median 0.97eV) was ~100meV larger than the barrier heights for the Ti-containing samples (median 0.86eV). The error bars correspond to the range in V_{bi} due to differences between C_s and C_p.

5.7 Conclusion

The results discussed in this chapter show that insulator tuning enabled a low barrier system (pSi-HfO2-Ti-Pt) to achieve a photovoltage of 514mV, which was similar to the performance of a higher barrier system (pSi-HfO2-Al-Pt) that had a photovoltage of 517mV. The insulator thickness optimization was different for the various metal bilayer systems with the Ti-Pt system achieving an optimized performance at 2.6nm, while the Al-Pt system had an optimized thickness at 1.9nm. A model was developed to provide a physical description of the MIS interface. The modeling

results suggest that the optimized insulator thickness and overall performance of the system is a function of the initial barrier height. The variance in insulator thickness optimization is due to differences in the level of majority carrier recombination at low insulator thickness. The low barrier systems require a thicker insulator to minimize majority carrier recombination currents compared to a higher barrier system. The work suggests that a simultaneous analysis of the barrier height and insulator thickness can be leveraged to optimize performance in the design of MIS structures. These results could be particularly useful for semiconductors that have difficulties forming high barriers (e.g. high band gap metal oxide semiconductors that cannot form p-n junctions). These systems could implement the use of metal bilayers to create barriers as high as possible, while mitigating remaining majority carrier recombination with insulator thickness optimization.

Chapter 6

Conclusions and Future Outlook

6.1 Conclusions from Previous Chapters

Photoelectrochemical water splitting is a promising route towards the development of clean hydrogen production. Chapter 1 discussed the general solar-to-hydrogen conversion process for semiconductor/electrocatalyst systems. This process involves (1) solar absorption, (2) charge carrier migration to the interface where photovoltage is generated, and (3) chemical transformations at electrocatalytic sites. The chapter discussed analyses showing that reactor type and STH conversion efficiency per area will ultimately dictate hydrogen production cost and economic viability. Semiconductors with a 1-2eV band gap were shown to be necessary to improve STH conversion efficiency, but these require protection layers from a corrosive aqueous environment. MIS structures were described as one of the promising protection strategies for ideal but unstable semiconductors.

Chapter 2 discussed the physical characteristics of MIS systems. It addressed how photovoltage is generated via a Schottky barrier, which is caused by the intrinsic Fermi level difference between a semiconductor and metal. Under illumination these junctions cause energetic minority carriers to move to the interface and drive the electrochemical reaction, while majority carriers are shuttled away from the interface. The chapter discusses several key design criteria that affect the energetics of these junctions and ultimately the photovoltage it produces. Chapter 3 describes a comprehensive mathematical model of the semiconductor-insulator-metal

interface. Poisson's equation, charge carrier continuity equations, and the Butler-Volmer equation were used to describe the underlying physical mechanisms that governs performance. With this model physical design parameters can be modulated to determine their effect on the current-voltage relationship of a system and corresponding band diagrams. This information allows the model to determine what design criteria have the largest impact on performance, and the underlying mechanisms behind the performance improvement.

Chapter 4 discusses an experimental system where a design parameter, the thickness of a tunnel insulator, was identified as a tunable experimental property that could be used to optimize photovoltage. This was shown experimentally using an nSi-HfO_2-Ni photoanode. The results showed that moderate insulator thicknesses maximized performance. The comprehensive model was used to provide mechanistic insight and showed that by using moderate insulator thickness it's possible to minimize majority charge carrier fluxes (that lead to recombination and poor photovoltage) without creating an overly large impediment for minority carriers used in the reaction.

Chapter 5 investigates the insulator tuning mechanism (discussed in Ch. 4) in order to quantify the degree to which insulator tuning affects photovoltage. The effects of insulator tuning were shown to be highly dependent on the barrier height of the system. High barrier systems were moderately improved with small insulator thicknesses, while lower barrier systems showed a higher degree of improvement with thicker insulators. This was shown experimentally with bilayer metal systems where various barrier height structures could be made with the selection of the inner metal layer. The lower barrier pSi-HfO_2-Ti-Pt system had a much higher degree of photovoltage improvement than the higher barrier pSi-HfO_2-Al-Pt system, though both performances were optimized at ~515mV.

6.2 Future Outlook: Semiconductor Electrocatalyst Pairings

A major conclusion of this work is that low-to-moderate barrier systems can greatly benefit from insulator thickness tuning. This strategy might be particularly useful for semiconductors such as Cu_2O that have difficulties in forming high Schottky barriers[104,117–119]. In these systems one could use bilayer metals to make a barrier height as good as possible for given the semiconductor Fermi level and band edge positions. Any remaining majority carrier recombination could be addressed with insulator thickness tuning to provide a high photovoltage. In this strategy the selection of the semiconductor/metallic materials and the analysis of the corresponding barrier height is critical for (1) ensuring that a high barrier is synthesized and (2) enable further improvements with insulator thickness tuning (the optimization of which is a function of barrier height). Tabulating semiconductors and metals in order to select promising semiconductor/electrocatalyst pairs could assist in material selection. An example of this is shown in Fig 6.1 where semiconductor band edge positions are shown next to the metal work functions (estimated on the same potential scale relative to NHE).

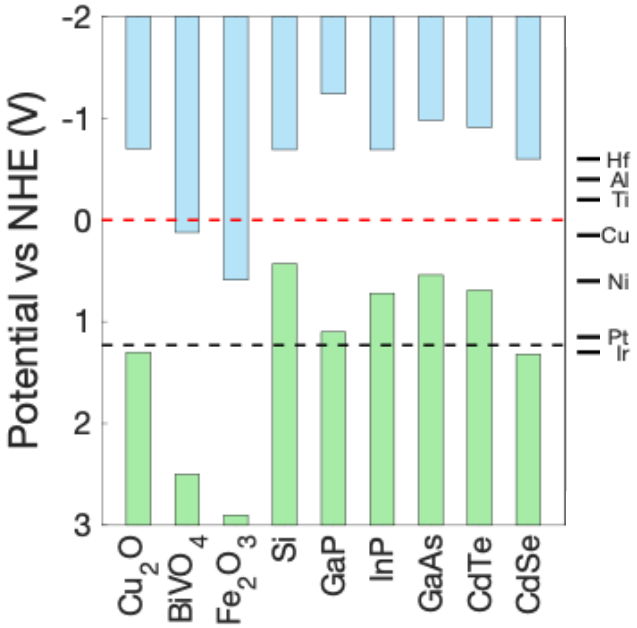

Figure 6.1 | Semiconductor band gaps, band edge positions, and metal work functions. Semiconductor band gaps, band edge positions, and metal work functions are plotted on the same potential scale (estimated vs NHE)[22,99,113,114]. The photovoltage of a MIS system could be improved with the selection of semiconductor/metal pairings to make the barrier height as high as possible while mitigating any remaining majority carrier recombination with insulator tuning.

6.3 Future Outlook: Island Systems to Improve Optical Absorption.

The photoelectrochemical systems discussed in this work could also benefit by integrating optical absorption strategies to maximize solar absorption within the semiconductor-electrocatalyst system[72,96–98,118,120–124]. Minimizing the parasitic absorption caused by the electrocatalyst or bilayer metals is critical in order to develop high efficiency systems. An example of an optical absorption design strategy is shown in Hernley et al.[72] where electrocatalytic nanoparticles were embedded within a semiconductor rather than adhering to the semiconductor surface. This reduced semiconductor reflection as well as parasitic absorption of the electrocatalytic material. It is particularly important to mitigate the high parasitic optical absorption of metal films, which were often used in this work. The nSi-HfO_2-Ni island samples shown in Fig 4.3 were fabricated for HfO_2 stability testing, but they show as a proof-of-concept that a metal island system on an HfO_2-protected semiconductor can be used for water splitting applications. Developing island or nanoparticle-based electrocatalytic systems that simultaneously maximize optical absorption, photovoltage generation, electrocatalytic activity, and stability could improve overall solar-to-hydrogen conversion.

Appendix

Code Instructions

In order to run the code open the SensitivityDriverMettalic.m file on MATLAB. The code can be easily modified to determine the effects of varying the design parameter of the system. The code requires the download of the 1.5 AM solar spectrum data, which is provided by NREL and can be downloaded in the following link. This should be saved in the same folder as a text file. https://rredc.nrel.gov/solar//spectra/am1.5/ASTMG173/ASTMG173.html

```
% Joseph Quinn, Nov 27, 2019
%
% SensitivityDriverMettalic
%
% Description: This is the primary driver to run the model. In this model
% you input a various design parameters for a semiconductor-electrocatalyst
% system. The model then uses finite differences to iteratively solve
% Poisson's equation and charge carrier continuity equation to describe
% potential and charge carrier concentration profiles across the
% semiconductor interface. With this data it calculates and outputs text
% files with current-voltage relationships. The model can be used to vary
% one design parameter at a time in order to examine its affect on the
% current-voltage curves.
%
% Usage: SensitivityDriverMettalic
%
% Instructions: The affect of the system design parameters on current
% voltage relationships can be determined inserting the values of any
% parameters into lines 88-89. Lines 94-96 will also have to
% be updated to reflect the design parameter. The voltage range in lines
% 98-99 may also need to be updated to reflect the modeled system. If the
% code does not converge try a smaller voltage range. Lastly "Vchange" can
% be modified to change the voltage "resolution" at the expense
% of computing time.
%
% Variables:
%     jocat = electrocatalyst exchange current (mA/cm^2)
%     valrelher = semiconductor valence band edge relative to HER (V)
%     bandgap = semiconductor band gap (eV)
%     WFcat = workfunction of electrocatalyst (relative to HER)
%     Vrangestart = start of the applied voltage range to be calculated (V)
%     Vrangeend = end of the range of applied voltages to be calculated (V)
%     Vrange = vector of the range of voltages to be calculated (V)
%     Vchange = the change between the voltage points the model will
calculate;
%     the "resolution" of the current-voltage curve.
%     Esol = redox potential of the solution (eV)
```

```
%     Nc = density of states in the semiconductor for electrons (cm^-3)
%     Nv = density of states in the semiconductor for holes (cm^-3)
%     d = doping density of the majority charge carrier (cm^-3)
%     nbulk = bulk concentration of the electrons (cm^-3)
%     pbulk = bulk concentration of the holes (cm^-3)
%     eps = dielectric constant of the semiconductor
%     vacperm = vacuum permitivity (C/Vcm)
%     q = charge of an electron (C)
%     kb = Boltzmann constant (J/K)
%     kbev = Boltzmann constant (eV/K)
%     T = Temperature (K)
%     B = recombination rate (cm^3s^-1)
%     alpha = %semiconductor optical absorption coefficient (cm^-1)
%     nun = mobility of electrons (cm^2/Vs)
%     nup = mobility of holes (cm^2/Vs)
%     kn = charge transfer coefficient at the semiconductor electrocatalyst
%     interface for electrons (mAcm)
%     kp = charge transfer coefficient at the semiconductor electrocatalyst
%     interface for holes (mAcm)
%     indexes = number of nodes in the semiconductor that will be used in the
%     finite difference calculation for potential and charge carrier
%     concentrations
%     Vbi = the built-in voltage of the semiconductor-electrocatalyst system
(V)
%     IsoValB = the energy of the valence band of the isolated semiconductor
%     relative to the H/H2 redox couple (V)
%     IsoCondB = the energy of the conduction band of the isolated
semiconductor
%     relative to the H/H2 redox couple (V)
%     IsoFermi = the energy of the fermi level of the isolated semiconductor
%     relative to the H/H2 redox couple (V)
%     EquibValB = the energy of the valence band of the equilibrated with a
%     metallic electrocatalyst with a set work function (V)
%     EquibCondB = the energy of the conduction band of the equilibrated with
a
%     metallic electrocatalyst with a set work function (V)
%     EquibFermi = the energy of the fermi level of the equilibrated with a
%     metallic electrocatalyst with a set work function (V)
%     Equib2ValB = the energy of the valence band of the equilibrated with a
%     metallic electrocatalyst and the solution (V)
%     Equib2CondB = the energy of the conduction band of the equilibrated
with a
%     metallic electrocatalyst and the solution (V)
%     Equib2ValB = the energy of the fermilevel of the equilibrated with a
%     metallic electrocatalyst and the solution (V)
%     photonflux is the number of photons from the 1.5AM solar spectrum that
the
%     semiconductor can absorb given its bandgap (photons.cm^2)
%     reflectance = the factor of how much light is not reflected by the
%     semiconductor surface
%     Data = a cell of the data calculated in the model

function SensitivityDriverMettalic


%kn2 = [1e-16];
```

```
%kp2 = kn2;



dd = [1e16];
% The following for loop will solve current-voltage relationships for each
% of the varying design parameters.
for s = 1:length(kn2)

    kp = -kp2(s); %each of the variable designed parameters are solved one at
a time
    kn = -kn2(s);
    d = dd;
%     kn = -kn2;
%     kp = -kp2;

    WF = WF2(s); % the work function of the electrocatalyst
    WFcat = 4.5-WF; % the work function of the electrocatalyst
    %title = ['kn-kp = ' num2str(-kn) ' (mAc) WF = ' num2str(WF) ' (eV)'];
    title = ['Knkp =' num2str(-kn) ' (mAc) WF = ' num2str(WF) 'hole (eV)'];

    %Vrangestart = Vrangestart2(s);
    Vrangestart = .6; %start of the applied voltage range to be calculated
    Vrangeend = .1; %end of the applied voltage range to be calculated
    Vchange = .001; %the "resolution" of the voltage range to be calculated

    Vrange = Vrangeend:.05:Vrangestart;%creates an initial voltage range to
be calcuated
    Esol = 0; %solution potential (eV)
    jocat = 1; %electrocatalyst exchange current
    valrelher = -.73; %valence band of teh semiconductor relative to the H/H2
redox couple
    bandgap = 1.12; %semiconductor bandgap
    Nc = 2.8e19; %DOS constants (cm^-3)
    Nv = 2.65e19; %DOS contant
    %Nv = 1.83e19otherref;
    %d = 1e16; %concentration of dopant
    pbulk = d; %bulk electron concentration (cm^-3)
    eps = 11.9; %sc dielectric constant (unitlessG)
    vacperm = 8.85e-12/100; %vacuum permitivity (C/Vcm)
    q = 1.60218e-19; %charge on carrier (C)
    kb = 1.38065e-23; %boltzmann constant (J/K)
    kbev = 8.61733e-5; %boltzmann constant (ev/K)
    T = 298.15; %temperature (K)
    B = 1e-15; %surface recombination rate (cm^3s^-1)
    alpha = 1e5; %semiconductor optical absorption (cm^-1)
    nun = 1450; %electron/hole mobility (cm^2/Vs)
    %nup = nun;
    nup = 500;
    indexes = 4000; %the number of nodes in the system
    %kp = 1e-13; %charge transfer coefficient for holes (mAcm)
    %kn = kp; %charge transfer coefficient for electrons (mAcm)

    IsoValB = valrelher; %isolated valence band (eV)
```

```
    IsoCondB = IsoValB+bandgap; %isolated conduction band (eV)
    %IsoFermi = IsoValB + kbev*T*log(pbulk/Nv); %isolated fermi level (eV)
    IsoFermi = IsoValB -kbev*T*log(pbulk/Nv); %isolated fermi level (eV)

    nbulk = Nc*exp(-(IsoCondB-IsoFermi)/(kbev*T)); %bulk concentration of
holes

    Vbi = IsoFermi-WFcat; %system built-in voltage
    nsurf = nbulk*exp(-q*Vbi/(kb*T)); %electron surface charge concentrations
(cm^-3)
    psurf = pbulk*exp(q*Vbi/(kb*T)); %hole surface charge concentrations
(cm^-3)

    EquibValB = IsoValB-Vbi; %equilibrated valence band to electrocatalyst
    EquibCondB = IsoCondB-Vbi; %equilibrated conduction band to
electrocatalyst
    EquibFermi = IsoFermi-Vbi; %equilibrated fermi level to electrocatalyst
    Equib2ValB = IsoValB-Vbi-(WFcat-Esol); %equilibrated valence to soln
    Equib2CondB = IsoCondB-Vbi-(WFcat-Esol); %equilibrated conduction band to
soln
    Equib2Fermi = IsoFermi-Vbi-(WFcat-Esol); %equilibrated fermi level to
soln



    %Function SolarIrradiance calculates the photon flux a semiconductor
    %can absorb given its band gap.
    [photonfluxm2, ~] = SolarIrradiance(bandgap,valrelher);
    photonflux = photonfluxm2/10000;%Places the photon flux in units of
phontons/cm^2
    reflectance = 1; %ratio of absorbed photons to total photons
    photonflux = photonflux*reflectance; %unreflected photons absorbed in
semiconductor



    figure(1)
    % The function datacruncher provides the systems design parameters and
    % returns the calculated data from the model in the Data cell
    [Data,leg] =
datacruncher(Vrange,Vchange,jocat,Esol,Vbi,nbulk,pbulk,nsurf,psurf,d,eps,vacp
erm,q,kb,kbev,T,photonflux,B,alpha,nun,nup,kn,kp,indexes,title);
    % The function videowriter creates a videofile of the energy bands and
    % current-voltage relationships as a function of applied voltage

videowriter(Data{4},Data{5},Data{6},Data{7},Data{3},Data{1},Data{2},Nc,Nv,d,e
ps,vacperm,q,kb,kbev,T,IsoValB-(WFcat-Esol),IsoCondB-(WFcat-
Esol),Esol,WFcat,kn,kp,alpha,jocat,title)
    % plotCVs plots the current-voltage relationship of the system
    plotCVs(Data{1},Data{2},Data{3},leg)

end
end


% datacruncher
%
```

```
% Description: This function uses the system design parameters of the
% semiconductor and electrocatalyst and calls various functions and returns
% the calculated model data. It uses an algorithm to add applied voltage
% points to the original voltage range specifically in the area of interest
% when current is low.
%
% Usage: [Data, leg] =
datacruncher(Vrange,Vchange,jocat,Esol,Vbi,nbulk,pbulk,nsurf,psurf,d,eps,vacp
erm,q,kb,kbev,T,photonflux,B,alpha,nun,nup,kn,kp,indexes)
%
% Variables
%
% Data = cell of data calculated in the model
% delx = the differences between the applied voltage data points
% orig = voltage range before added voltage points
% voltadder = additional voltage points to increase resolution in the area of
interest

function [Data, leg] =
datacruncher(Vrange,Vchange,jocat,Esol,Vbi,nbulk,pbulk,nsurf,psurf,d,eps,vacp
erm,q,kb,kbev,T,photonflux,B,alpha,nun,nup,kn,kp,indexes,title)

Data = cell(1,10); %creates an empty cell for the model data
%CVsolver2 uses the model parameters to calculate the model data
%This data is for the initial voltage range specified in
SensitivityDriverMettalic
for j = 1:1:length(Vrange)
    %The try catch ensure the range is bound by where the system converges
    try

[Data{1}(j),Data{2}(j),Data{3}(j),Data{4}(:,j),Data{5}(:,j),Data{6}(:,j),Data
{7}(:,j),Data{9}(:,j),Data{10}(:,j)] =
CVsolver2(Vrange(j),jocat,Esol,Vbi,nsurf,psurf,nbulk,pbulk,d,eps,vacperm,q,kb
,kbev,T,photonflux,B,alpha,nun,nup,kn,kp,indexes);
        Data{8}(1,j) = Vrange(j);
    catch
        break
    end

end
%Data{8}(1,:) = Vrange;

%The applied voltage points are affected by the specified initial voltage
%range and the calculated electrocatalyst voltage. This for loop looks at
%the differences between the applied voltage points
for ii = 1:length(Data{1}(:))-1
    delx(ii) = abs(Data{1}(ii+1)-Data{1}(ii));
end

%This while loop adds voltage points in between the applied voltage data
%points in order to get a high number voltage resolution, without adding
%unnecessary calculation time.
while max(delx) >= Vchange %this while loop adds points as when the voltage
spacings are greater than Vchange
    voltadder = [];
    for w = 1:length(Data{1}(:))-1
```

```
        if abs(Data{1}(w+1)-Data{1}(w)) >= Vchange && abs(Data{2}(w)) <= 50
            voltadder = [voltadder (Data{8}(w+1)+ Data{8}(w))/2]; %adds
points in the initial voltage range where there are large spacings
        end
    end

    %the following for loop calculates model data for the added voltage
    %points
    orig = length(Data{1}(:));
    for j = orig+1:1:orig+length(voltadder)

[Data{1}(j),Data{2}(j),Data{3}(j),Data{4}(:,j),Data{5}(:,j),Data{6}(:,j),Data
{7}(:,j),Data{9}(:,j),Data{10}(:,j)] = CVsolver2(voltadder(j-
orig),jocat,Esol,Vbi,nsurf,psurf,nbulk,pbulk,d,eps,vacperm,q,kb,kbev,T,photon
flux,B,alpha,nun,nup,kn,kp,indexes);
    end

    Data{8} = [Data{8}(1,:) voltadder];
    [Data{1}(1,:), sortind] = sort(Data{1}(:)); %this function resorts the
cell data with increasing voltage (according to

    %the following for loop resorts the rest of the data in order of
    %increasing applied voltage
    for c = 2:10
        temp = Data{c};
        for b = 1:length(Data{1}(:))
            Data{c}(:,b) = temp(:,sortind(b));
        end
    end

    %The following for loop recalculates the spacing between applied
    %voltage points.
    delx = [];
    for ii = 1:length(Data{1}(:))-1
        if abs(Data{2}(ii)) <= 50 &&  abs(Data{2}(ii+1)) <= 50
            delx = [delx abs(Data{1}(ii+1)-Data{1}(ii))];
        end

    end
% %
%     if length(Data{1}(:)) >= 500
%         break
%     end
end


%The following lines calls the write files function in order to create text
%files with the calculated voltage, current, electrocatalyst voltage, and
%the values in the variable design parameter.
parameter = zeros(1,length(Data{1}));
parameter(1,:) = kn;
leg = title;
writefiles(title,Data{2}(:),Data{1}(:),Data{3}(:),parameter(:))
writefiles(strcat(title,'Hole
Current'),Data{9}(:),Data{1}(:),Data{3}(:),parameter(:))
```

```
writefiles(strcat(title,'Elec
Current'),Data{10}(:),Data{1}(:),Data{3}(:),parameter(:))
%leg = ['kn-kp = ' num2str(kn) ' (mAcm)'];
%writefiles(['kn-kp = ' num2str(kn) '
(mAc)'],Data{2}(:),Data{1}(:),Data{3}(:),parameter(:))
end



% videowriter
%
% Description: This code uses the data acquired in datacruncher in order to
% write video files which record band diagrams and current as function of
% voltage, which provides insight into how experimental design parameters
% affect the interfacial mechanisms that governs performance.
%
% Usage:
videowriter(phi,n,p,xaxis,Vcat,TotalV,Crange,Nc,Nv,d,eps,vacperm,q,kb,kbev,T,
Equib2ValB,Equib2CondB,Esol,WF,kn,kp,alpha,jocat)
%
% Variables:
%     unredphi = potential (V) calculated from reduced potential
%     Econd = energy of the conduction band
%     Eval = energy of the valence band
%     Efn = quasi-fermi level of electrons
%     Efp = quasi-fermi level of holes
%     F = format for data to write video files

function
videowriter(phi,n,p,xaxis,Vcat,TotalV,Crange,Nc,Nv,d,eps,vacperm,q,kb,kbev,T,
Equib2ValB,Equib2CondB,Esol,WF,kn,kp,alpha,jocat,title)

unredphi = phi(1,:)*kb*T/q; %converts the calculated reduced potential into
potential in units of volts
Econd = (Equib2CondB)-unredphi-Vcat; %energy of the conduction band
Eval = (Equib2ValB)-unredphi-Vcat; %energy of the valence band
Efn = kbev*T*log(n(1,:)*d/Nc)+Econd; %quasi-fermi level of electrons
calculated from electron concentration
Efp = Eval-kbev*T*log(p(1,:)*d/Nv); %quasi-fermi level of holes calculated
from hole concentration

[minMA, I] = min(abs(Crange));
figure(15)
plot(TotalV(I),Crange(I),'.r','markersize',40); %provides a marker to track
the voltage for the calulated band diagram
hold on
CV(TotalV(:),Crange(:))
hold off
figure(16)
plotvoltagedrops(phi(:,I),n(:,I),p(:,I),xaxis(:,I),Vcat(I),TotalV(I),Equib2Va
lB,Equib2CondB,Esol,WF,Nc,Nv,d,eps,vacperm,q,kb,kbev,T)


F(length(TotalV(:,1))) = struct('cdata',[],'colormap',[]); %creates the
format to write videos
%writerObj = VideoWriter(['Bandbend' num2str(kn) '.avi']);
```

```
writerObj = VideoWriter(strcat(title,'.avi'));

open(writerObj)

%This for loops graphs the band diagrams, current, etc. as a function of
%voltage, and records these graphs into frames which are used to create the
%videos
for j = length(TotalV):-1:1
    fig = figure(2);
    scrsz = get(0,'ScreenSize'); %sets the size of the graphs
    set(fig,'Position',[1 scrsz(4)*.75 scrsz(3)*.75 scrsz(4)*.75])
    subplot(1,2,1)
    %plotvoltagedrops plots the band diagrams for a specific applied
    %voltage

plotvoltagedrops(phi(:,j),n(:,j),p(:,j),xaxis(:,j),Vcat(j),TotalV(j),Equib2Va
lB,Equib2CondB,Esol,WF,Nc,Nv,d,eps,vacperm,q,kb,kbev,T)
    subplot(1,2,2)
    %CV plots the current as a function of voltage
    CV(TotalV(:),Crange(:))
    hold on
    plot(TotalV(j),Crange(j),'.r','markersize',40); %provides a marker to
track the voltage for the calculated band diagram

%The following lines of code can be used to add more data into the video
%files if to track specific values as a function of voltage. This is useful
%to see a variables affect on certain parameters that govern performance

%     set(fig,'Position',[1 scrsz(4)*.75 scrsz(3)*.75 scrsz(4)*.75])
%     subplot(2,2,1)
%
plotvoltagedrops(phi(:,j),n(:,j),p(:,j),xaxis(:,j),Vcat(j),TotalV(j),Equib2Va
lB,Equib2CondB,Esol,WF,Nc,Nv,d,eps,vacperm,q,kb,kbev,T)
%     ylim([-3 3]);
%     subplot(2,2,2)
%     CV(TotalV(:),Crange(:))
%     hold on
%     plot(TotalV(j),Crange(j),'.r','markersize',40);
%     subplot(2,2,3)
%     xindex = 1:1:length(phi);
%     plot(xaxis((1:500),j),n((1:500),j),'LineWidth',4)
%     hold on
%     set(gca,'fontsize',20)
%     title('Electron Concentration')
%     xlabel('Reduced Length')
%     ylabel('Reduced Electron Concentration')
%
%     subplot(2,2,3)
%     plot(xaxis((1:500),j),p((1:500),j),'LineWidth',4)
%     hold on
%     set(gca,'fontsize',20)
%     title('Hole Concentration')
%     xlabel('Reduced Length')
%     ylabel('Reduced Electron Concentration')
% %
```

```
% % This plots the energy between the conduction band an the quasi-fermi
level for electrons which affects electron transport
% %     subplot(2,2,3)
% %     plot(TotalV,Econd-Efn,'LineWidth',4)
% %     hold on
% %     plot(TotalV(j),Econd(j)-Efn(j),'.r','markersize',40)
% %     set(gca,'fontsize',20)
% %     title('Conduction Band-Efn vs Voltage')
% %     xlabel('Applied Voltage')
% %     ylabel('Conduction Band-Efn')
% %     hold off
% %
% % This plots the energy between the quasi fermi level for holes and the
% % electrocatalsyt voltage affects hole transport
% %     subplot(2,2,4)
% %     plot(TotalV,Efp+Vcat,'LineWidth',4)
% %     hold on
% %     plot(TotalV(j),Efp(j)+Vcat(j),'.r','markersize',40)
% %     set(gca,'fontsize',20)
% %     title('Hole Fermi Level-Vcat')
% %     xlabel('Applied Voltage')
% %     ylabel('Hole Fermi Level-Vcat')
% %     hold off
%The following lines formats and writes the frames into the video.
    set(gcf,'color','w')
    F(j) = getframe(fig);
    writeVideo(writerObj,F(j))
    clf
end
movie(F,1,1000)
close(writerObj)
% The following lines can be used to write miscellaneous data
% BB = [TotalV; Econd-Efn; Efp+Vcat; Vcat]';
% fileID = fopen(strcat('Activation Barriers',num2str(kn),'.txt'),'w');
% fprintf(fileID,'%s\t%s\t%s\t%s\n','Voltage(V)','Econd-
Efn(V)','Efp+Vcat(V)','Vcat(V)');
% fprintf(fileID,'%e\t%e\t%e\t%e\n',BB');
% fclose(fileID);

end



% Joseph Quinn, Nov 27, 2019
%
% SolarIrradiance
%
% Description: This this function calculates the photonflux a
% semiconductor can capture given its band gap for the 1.5AM solar
% spectrum. It measures the totalsolar irradiance for efficiency
% calculations. Lastly it plots the radiation the semiconductor can absorb
% of the total solar irradience.
%
% Usage: [photonfluxbg, totalsolarirrad] = SolarIrradiance(bandgap,valrelher)
%
% Variables:
%     files = calls the AM1.5 Solar spectrum text file
```

```
%     Data = categories of data of the calls the AM1.5 Solar spectrum text
%     c = speed of light
%     h = Plancks constant (eVs)
%     kev = Boltzmans constant (eV/K)
%     energies = Photon energies from the AM 1.5 Solar spectrum
%     totalsolarirrad = the total solar irradience of the solar spectrum
%     photonfluxbg = the photon flux the semiconductor can absorb
%     totphotonflux = the total photon flux of the 1.5AM solar spectrum
%     siabsratio = the ratio of radiation the semiconductor can absorb
relative
%     to the total irradience for a given wavelength
%     wavesi = the wavelengths of the 1.5AM solar spectrum
%     sirad = the radiation the semiconductor can absorb for a given
wavelength

function [photonfluxbg, totalsolarirrad] = SolarIrradiance(bandgap,valrelher)

files = dir('*.txt');
Data = cell(4,2); %creates a data cell for the AM 1.5 solar spectrum
Names = {'a';'b';'c';'d'};
tempdat = importdata(files(1).name);
for i=1:4
    Data(:,1) = Names;
    Data(i,2) = num2cell(tempdat.data(:,i),[1 2]);
end

c = 299792458; %speed of light (m/s)
h = 4.135667e-15; %planks constant (eVs)
hj = 6.62607e-34;%planks constang (kJs)
energies = h*c./(Data{1,2}(:)*(1e-9)); %energy of wavelengths
[bg index] = min(abs(energies-bandgap)); %finds the minimum photon energy the
semiconductor can absorb

%photon flux the semiconductor can absorb given its bandgap
photonfluxbg =
trapz(Data{1,2}(1:index),Data{3,2}(1:index).*Data{1,2}(1:index)*1e-9/(hj*c));
%total solar erradience of the 1.5AM solar spectrum
totalsolarirrad = trapz(Data{1,2}(:),Data{3,2}(:));
%total photonflux of the 1.5AM solar spectrum
%totphotonflux = trapz(Data{1,2}(:),Data{3,2}(:).*Data{1,2}(:)*1e-9/(hj*c));

%This for loop finds the solar irradiance the semiconductor can absorb
%given its band gap
siabsratio = 0; %Ratio to energy semiconductor can absorb to the total
wavesi = 0; %Wavelengths in the 1.5AM solar spectrum data
sirad = 0; %Solar irradiance the semiconductor can absorb at each wavelength
of the 1.5AM solar spectrum
for j = 1:length(energies)
    if energies(j) >= bandgap
        siabsratio(j,1) = bandgap/energies(j);
        sirad(j,1) = siabsratio(j)*Data{3,2}(j);
        wavesi(j,1) = Data{1,2}(j);
    else
        break
    end
end
```

```
%Plots the solar irradience the semiconductor can absorb given its band gap
figure(5)
sirad = [sirad; 0]; %format data
wavesi = [wavesi; Data{1,2}(length(wavesi)+1)];%format data for plot
hold on
area(Data{1,2}(:),Data{3,2}(:),'facecolor','r')%area plot of total solar
irradience
area(wavesi,sirad,'facecolor','b')%area plot of radiation semiconductor can
absorb
%sets format/title/labels
set(gca,'fontsize',20)
title('Solar Spectrum Captured by Silicon')
xlabel('Wavelength')
ylabel('Solar Irradiance (W/m^2nm)')
axis([Data{1,2}(1) Data{1,2}(end) 0 2])

figure(6)
%Plots the semiconductors band edge positions
plot([0 8],[0 0],'--r')
hold on
plot([3.5 4.5],[valrelher valrelher],'k')
plot([3.5 4.5],[valrelher+bandgap valrelher+bandgap],'k')
plot([4 4],[valrelher valrelher+bandgap],'k')
axis([0 8 valrelher-1 valrelher+bandgap+1])
set(gca, 'XTickLabelMode', 'Manual')
set(gca, 'XTick', [])
title('Band Position Relative to HER')
ylabel('Band Position (eV)')
set(gca,'fontsize',20)
hold off

end


% Joseph Quinn, Nov 27, 2019
%
% Poissons
%
% Description: Poisson's solver uses the Poisson equation to solve for a
% correction term to the potential profile. The function iterates until the
% correction is small and outputs the corrected potential profile.
%
% Usage: [delta,newphi,newn,newp] =
Poissons(delxwhole,delxhalf,phi,n,p,indexes)
%
% Variables:
%     Apoiss = a matrix of coefficients for equations derived from Poisson's
%     equation at each node
%     Cpoiss = a vector of the solutions for to Poisson's equation at each
node
%     delxwhole = the whole number indexes of nodes (central finite
difference)
%     delxhalf = the odd number indexes of nodes (central finite difference).
%     a = a coefficient used in to simplify the finite difference equations
%     b = a coefficient used in to simplify the finite difference equations
```

```
%     phi = reduced potential
%     n = reduced electron concentration
%     p = reduced hole concentration
%     indexes = total number of nodes
%     delta = the correction term for the potential profile
%     newphi = the corrected potential profile
%     newn = the corrected concentration of electrons
%     newp = the corrected concentration of holes

function [delta,newphi,newn,newp] =
Poissons(delxwhole,delxhalf,phi,n,p,indexes)

Apoiss = zeros(indexes/2,indexes/2); %sets up an empty matrices that will be
used for the equations at each node
Cpoiss = zeros(indexes/2,1);

%The following lines set the boundary Conditions listed in Mills S52
Apoiss(1,1) = 1;
Apoiss(end,end) = 1;
Cpoiss(1) = 0;
Cpoiss(end) = 0;

%This for loop inputs the coefficients for the equations that will be
%solved for each node
for i = 2:length(phi)-1
    a = delxwhole(i)/delxwhole(i-1); %the a value given in Mills S52
    b = delxwhole(i)*delxhalf(i); %the b value given in Mills S52
    Apoiss(i,i-1) = a; %Mills S52
    Apoiss(i,i) = -(1+a+b*(exp(phi(i)-(phi(i)-
log(n(i))))+exp(phi(i)+log(p(i))-phi(i)))); %Mills S52
    Apoiss(i,i+1) = 1; %Mills S52
    Cpoiss(i,1) = -(phi(i+1)-phi(i))+a*(phi(i)-phi(i-1))+b*(exp(phi(i)-
(phi(i)-log(n(i))))-exp((phi(i)+log(p(i)))-phi(i))+1); %Mills S52
end

delta = Apoiss\Cpoiss; %Solves for the delta correction term
delta = real(delta); %outputs real part (imaginary close to 0)
newphi = phi + delta; %corrects phi by the delta correction term
newn = n.*exp(delta); %updates e profile given by Mills S52
newp = p.*exp(-delta); %updates h profile given by Mills S52

end


% Joseph Quinn, Nov 27, 2019
%
% plotvoltagedrops
%
% Description: plotvoltage drops uses the model data in order to plot band
% diagrams a function of voltage.
%
% Usage:
plotvoltagedrops(phi,n,p,xaxis,Vcat,TotV,IsoValB,IsoCondB,Esol,WFcat,Nc,Nv,d,
eps,vacperm,q,kb,kbev,T)
%
```

```
% Variables:
%     phi = reduced potential
%     n = reduced electron concentration
%     xaxis = the reduced length along the semiconductor
%     Vcat = the electrocatalyst voltage (V)
%     TotB = the applied voltage (B)
%     debyeL = the debye length of the semiconductor (cm)
%     IsoValB = the isolated valence band energy (eV)
%     IsoCondB = the isolated conduction band energy (eV)
%     Esol = the energy of the redox couple in solution (eV)
%     WFcat = the electrocatalyst work function relative to H/H2 (eV)
%     Nc = the electron density of states (1/cm^3)
%     Nv = the hole density of states (1/cm^3)
%     d = the dopant density (1/cm^3)
%     eps = dielectric constant of the semiconductor
%     vacperm = vacuum permitivity (C/Vcm)
%     q = charge of an electron (C)
%     kb = Boltzmann constant (J/K)
%     kbev = Boltzmann constant (eV/K)
%     T = Temperature
%     unredxcm = the length of the semiconductor (cm)
%     unredx = the length of the semiconductor (nm)
%     xvplot = the length of the semiconductor (less deep into the
semiconductor
%     for a closer view of the interface
%     shift = shifts the band diagram to add lines to mark the
electrocatalyst/soln
%     Econd = the energy of the equilibrated conduction band
%     Eval = the energy of the equilibrated valence band
%     Efn = the quasi-Fermi level for electrons
%     Efp = the quasi-Fermi level for holes
%     vcatx/y = lines marking the placement of the elecgtrocatalyst
%     solx/y = lines marking the placement of the solution
%     boundxc/yc/xs/ys = plot boundaries
%     totalvy/vx = marks the applied voltage

function
plotvoltagedrops(phi,n,p,xaxis,Vcat,TotV,IsoValB,IsoCondB,Esol,WFcat,Nc,Nv,d,
eps,vacperm,q,kb,kbev,T)

debyeL = sqrt(eps*vacperm*kb*T/(q^2*d)); %debye length of teh semiconductor
unredxcm = xaxis*debyeL; %marks the length of the nodes along the
semiconductor (cm)
unredx = unredxcm*1e7; %marks the length of the nodes along the semiconductor
(nm)

xvplot = unredx(1:end/2); %only uses half the nodes of the semiconductor for
a closer view of teh interface
shift = .2*xvplot(end); %shifts the plot to mark where the electrocatalyst
and solution fit
xvplot = shift+xvplot;
unredphi = phi(1:end/2)*kb*T/q; %changes the reduced potential to potential
(V)
Econd = (IsoCondB)-unredphi-Vcat; %energy of the conduction band
Eval = (IsoValB)-unredphi-Vcat; %energy of the valence band
```

```
Efn = kbev*T*log(n(1:end/2)*d/Nc)+Econd; %quasi-Fermi level energy for
electrons
Efp = Eval-kbev*T*log(p(1:end/2)*d/Nv); %quasi-Fermi level energy for holes

vcaty = [-Vcat -Vcat]; %marks the electrocatalyst voltage
vcatx = [shift*.5 shift];
soly = [Esol Esol]; %marks the solution potential
solx = [0 shift*.5];
boundxc = [shift*.5 shift*.5]; %sets the bounds of the plot
boundyc = [-3 3];
boundxs = [shift shift];
boundys = [-3 3];
totalvy = [-TotV -TotV]; %marks the applied potential
totalvx = [0 xvplot(end)];
hold on
plot(totalvx,totalvy,'--r','LineWidth',3) %plots applied potential
plot(vcatx,vcaty,'k','LineWidth',3) %plots the electrocatalyst voltage
plot(solx,soly,'k','LineWidth',3) %plots the solution potential
plot(boundxc,boundyc,'--k') %sets the boundaries between the
solution/electrocatalyst/semiconductor
plot(boundxs,boundys,'--k')
plot(xvplot,Econd,'LineWidth',3) %plots the conduction band energy
plot(xvplot,Eval,'LineWidth',3) %plots the valence band energy
plot(xvplot,Efn,'LineWidth',3) %plots the quasi-Fermi level for electrons
plot(xvplot,Efp,'LineWidth',3) %plots the quasi-Fermi level for holes
set(gca,'fontsize',20) %formats and labels graph
title('Potential vs Distance')
xlabel('Distance (nm)')
ylabel('Potential (eV)')

end


% Joseph Quinn, Nov 27, 2019
%
% plotsCVs
%
% Description: This function plots the modeled current voltage
% relationships and the electrocatalyst voltage as a function of applied
% potential.
%
% Usage: plotCVs(TotalV,Crange,Vcat,leg)
%
% Variables
%     TotalV = applied potential (V)
%     Crange = the current (mA)
%     Vcat = the electrocatalyst voltage (V)
%     leg = the labels for the legend

function plotCVs(TotalV,Crange,Vcat,leg)

%plotCVs
figure(10)
plot(TotalV,Crange,'LineWidth',3) %plots current as a function of applied
potential
hold on
```

```
set(gca,'fontsize',20) %formats and lables graph
title('Current Voltage Curve')
xlabel('Voltage (V)')
ylabel('Current (mA/cm^2)')
legend(leg)

%Plots Vcat vs V
figure(11)
plot(TotalV,Vcat,'LineWidth',3) %plots electrocatalyst voltage as a function
of applied potential
hold on
set(gca,'fontsize',20) %formats and labels graph
title('Vcat vs Voltage ')
xlabel('Voltage (V)')
ylabel('Vcat (V)')
legend(leg)

end



% Joseph Quinn, Nov 27, 2019
%
% metallicVcat
%
% Discription: MetallicVcat determines Vcat by solving the Butler-Volmer
% equation using an intrinsic MATLAB function.
%
% Usage: writefiles(Name,Current,Voltage,Vcat,parameter)
%
% Variables:
%     q = charge of an electron (C)
%     kb = boltzmann constant (J/K)
%     T = temperature (K)
%     Vcat = electrocatlyst voltage (V)
%     jcat = current (mA/cm^2)
%     jocat = electrocatalyst exchange current (mA/cm^2)

function Vcat = metallicVcat(jcat,jocat)

q = 1.60218e-19; %charge on carrier (C)
kb = 1.38065e-23; %Boltzmann constant (J/K)
T = 298.15; %temperature (K)
syms Vc
Vcat = vpasolve(exp(q*Vc/(2*kb*T))-exp(-q*Vc/(2*kb*T))==jcat/jocat,Vc);
%solves Butler-Volmer equation with an intrinsic MATLAB function
Vcat = double(Vcat);%Removes imaginary artifacts
end



% Joseph Quinn, Nov 27, 2019
%
% holecon
%
% Description: holecon solves the continuity equations for holes using
% recombination, potential, and absorption terms. It outputs an updated
```

```
% hole concentration.
%
% Variables
%     delxwhole = the change in x distance between the whole number indexes
used
%     in the central difference equations
%     delxhalf = the change in x distance between the odd number indexes used
%     in the central difference equations
%     phi = reduced potential
%     p = reduced hole concentration
%     n = reduced electron concentration
%     Bred = reduced recombination coefficient
%     Ired = reduced intensity
%     alphared = the absorption coefficient
%     nend = the electron concentration of the final node (boundary
condition)
%     pend = the hole concentration of the final node (boundary condition)
%     p1 = the hole concentration of the first node
%     xaxis = the x length (depth) of each node along the semiconductor
%     kpred = the reduced charge transfer coefficient between the
semiconductor and metal
%     indexes = the total number of nodes the system is solving for
%     Ahole = a matrix of coefficients for equations derived from the hole
%     continuity equation at each node
%     Chole = a vector of the solutions for to the hole continuity equation
at
%     each node
%     newp = the solved hole concentration
%     pchange = the change between the updated and initial hole concentration

function [newp,pchange] =
holecon(delxwhole,delxhalf,phi,p,n,Bred,Ired,alphared,nend,pend,p1,xaxis,kpre
d,indexes)

%Sets up an empty matrices that will be used for the equations at each node
Ahole = zeros(indexes/2,indexes/2);
Chole = zeros(indexes/2,1);

%Boundary Conditions
Ahole(end,end) = 1; %sets final hole concentration to the bulk value
Chole(end) = pend;

%Sets flux boundary conditions (Mills et al.)
Ahole(1,1) = -((phi(2)-
phi(1))/2)+1+kpred*delxwhole(1)+delxwhole(1)*delxhalf(1)*Bred*n(1);
Ahole(1,2) = -((phi(2)-phi(1))/2+1);
Chole(1) =
delxwhole(1)*delxhalf(1)*(Bred*nend*pend+Ired*alphared)+kpred*p1*delxwhole(1)
;

for i = 2:length(phi)-1;
    a = delxwhole(i)/delxwhole(i-1); %the a value given in Boettcher S52
    b = delxwhole(i)*delxhalf(i); %the b value given in Boettcher S52
    Ahole(i,i-1) = a*((phi(i)-phi(i-1))/2-1); %sets coefficient 1
    Ahole(i,i) = -(phi(i+1)-phi(i))/2+1+a*((phi(i)-phi(i-
1))/2+1)+b*Bred*n(i); %sets coefficient 2
```

```
    Ahole(i,i+1) = -((phi(i+1)-phi(i))/2+1); %sets coefficient 3
    Chole(i,1) = b*(Bred*nend*pend+Ired*alphared*exp(-alphared*xaxis(i)));
%sets the solution to the continuity equations
end

newp = Ahole\Chole; %solves for the updated hole concentrations
pchange = max(abs(newp-p))/max(abs(p)); %records the change in hole
concentration
end

% Joseph Quinn, Nov 27, 2019
%
% eleccon
%
% Description: eleccon solves the continuity equations for electrons using
% recombination, potential, and absorption terms. It outputs an updated
% hole concentration.
%
% Variables
%     delxwhole = the change in x distance between the whole number indexes
used
%     in the central difference equations
%     delxhalf = the change in x distance between the odd number indexes used
%     in the central difference equations
%     phi = reduced potential
%     p = reduced hole concentration
%     n = reduced electron concentration
%     Bred = reduced recombination coefficient
%     Ired = reduced intensity
%     alphared = the absorption coefficient
%     nend = the electron concentration of the final node (boundary
condition)
%     pend = the hole concentration of the final node (boundary condition)
%     n1 = the hole concentration of the first node
%     xaxis = the x length (depth) of each node along the semiconductor
%     knred = the reduced charge transfer coefficient between the
semiconductor and metal
%     indexes = the total number of nodes the system is solving for
%     Aelec = a matrix of coefficients for equations derived from the
%     electron continuity equation at each node
%     Celec = a vector of the solutions for to the electron continuity
%     equation at each node
%     newn = the solved electron concentration
%     nchange = the change between the updated and initial electron
concentration

function [newn,nchange] =
eleccon(delxwhole,delxhalf,phi,p,n,Bred,Ired,alphared,nend,pend,n1,xaxis,knre
d,indexes)

%Sets up an empty matrices that will be used for the equations at each node
Aelec = zeros(indexes/2,indexes/2);
Celec = zeros(indexes/2,1);

%Boundary Conditions
Aelec(end,end) = 1; %sets final electron concentration to the bulk value
```

```
Celec(end) = nend;

%Sets flux boundary conditions
Aelec(1,1) = 1+(phi(2)+phi(1))/2-
delxwhole(1)*knred+delxwhole(1)*delxhalf(1)*Bred*p(1); %S59 Boettcher
Aelec(1,2) = (phi(2)-phi(1))/2-1; %S59 Boettcher
Celec(1) = delxwhole(1)*delxhalf(1)*(Bred*nend*pend+Ired*alphared)-
delxwhole(1)*knred*n1; %S59 Boettcher

for i = 2:length(phi)-1
    a = delxwhole(i)/delxwhole(i-1); %the a value given in Boettcher S52
    b = delxwhole(i)*delxhalf(i); %the b value given in Boettcher S52
    Aelec(i,i-1) = -a*((phi(i)-phi(i-1))/2+1); %sets the first coefficient
    Aelec(i,i) = 1+a+(phi(i+1)-phi(i))/2-a*(phi(i)-phi(i-1))/2+b*Bred*p(i);
%sets the second coefficient
    Aelec(i,i+1) = (phi(i+1)-phi(i))/2-1; %sets the third coefficient
    Celec(i,1) = b*(Bred*nend*pend+Ired*alphared*exp(-alphared*xaxis(i)));
%sets the solutions to the electron concentration
end

newn = Aelec\Celec; %solves for the updated electron concentrations
nchange = max(abs(newn-n))/max(abs(n)); %records the change in electron
concentration
end



% Joseph Quinn, Nov 27, 2019
%
% CVsolver2
%
% Description: CV solver takes a voltage and applies it to a semiconductor.
% it iterates between the Poisson's equation and continuity equations in
% order to converge on a solution for hole-electron concentrations and
% potential. Current is determined from this data.
%
% Usage: [delta,newphi,newn,newp] =
Poissons(delxwhole,delxhalf,phi,n,p,indexes)
%
% Variables:
%     voltage = voltage applied to the semiconductor (not including
%     electrocatalyt voltage, which is solved separately and added)
%     jocat = electrocatalyst exchange current (mA/cm^2)
%     Esol = redox potential of the solution
%     Vbi = built-in voltage of the system
%     nsurf =  concentration of electrons at the interface
%     psurf = concentration of holes at the interface
%     nbulk = bulk concentration of electrons
%     pbulk = bulk concentration of holes
%     d = dopant density
%     eps = dielectric constant of the semiconductor
%     vacperm = vacuum permittivity (C/Vcm)
%     q = charge of an electron (C)
%     kb = Boltzmann constant (J/K)
%     kbev = Boltzmann constant (eV/K)
%     T = Temperature (K)
%     B = recombination rate (cm^3s^-1)
```

```
%     alpha = %semiconductor optical absorption coefficient (cm^-1)
%     nun = mobility of electrons (cm^2/Vs)
%     nup = mobility of holes (cm^2/Vs)
%     kn = charge transfer coefficient at the semiconductor electrocatalyst
%     interface for electrons (mAcm)
%     kp = charge transfer coefficient at the semiconductor electrocatalyst
%     interface for holes (mAcm)
%     indexes = total number of nodes
%     TotalV = total applied potential
%     CurrentmA = current (mA)
%     Vcat = electrocatalyst voltage
%     phi = reduced potential
%     n = reduced electron concentration
%     p = reduced hole concentration
%     xaxis = reduced depth into the semiconductor
%     f = fine mesh grid spacing
%     c = course mesh grid spacing
%     r = rate of transition of mesh grid
%     trans = sets transition from fine to course mesh
%     delta = change in x distance (depth) as a function of index
%     x = depth in the semiconductor
%     lengthofsemi = sets the total length of the semiconductor
%     xred = reduced length in the semiconductor
%     xaxis = sets the xaxis with half the number of indices (used in central
difference)
%     wholeindex = xaxis with odd indices
%     delxhalf = change in x distance (depth) between the odd indices
%     delxwhole = change in x distance (depth) between the whole indices
%     scV = voltage drop at the semiconductor which is a combination of
built-in and applied voltage
%     reducedvoltage = reduced potential term
%     phi1 = potential of the first node
%     phiend = potential of the final node
%     guessfactor = factor used to algorithms to guess the initial potential
profile
%     n1 = electron concentration of first node
%     nend = electron concentration of final node
%     p1 = hole concentration of first node
%     pend = hole concentration of final node
%     phichange = maximum change in potential of between Gummel iterations
%     nchange = maximum change in electron concentration of between Gummel
iterations
%     pchange = maximum change in hole concentration of between Gummel
iterations
%     oldphi = the potential of the previous Poisson's equation iteration
%     unredcurrentp = reduced hole current
%     unredcurrentn = reduced electron current
%     Current = total current (A)

function [TotalV,CurrentmA,Vcat,phi,n,p,xaxis,HoleCmA,ElecCmA] =
CVsolver2(voltage,jocat,Esol,Vbi,nsurf,psurf,nbulk,pbulk,d,eps,vacperm,q,kb,k
bev,T,photonflux,B,alpha,nun,nup,kn,kp,indexes)

%Reduces important variables in code
debyeL = sqrt(eps*vacperm*kb*T/(q^2*d)); %debye length
Ired = q*debyeL*photonflux/(nun*kb*T*d); %Reduced photon flux
```

```
alphared = debyeL*alpha; %reduced absorption coefficient
knred = kn*debyeL/(nun*kb*T); %reduced charge transfer rate constant
kpred = kp*debyeL/(nup*kb*T); %reduced charge transfer rate constant
Bred = B*d*(debyeL^2)*q/(nun*kb*T); %reduced recombination rate

%Making the X Grid (for depth into the semiconductor
f = .001; %sets the fine mesh grid spacing given in Mills S47
c = .05; %sets the coarse mesh grid spacing given in Mills S47
r = .003; %sets the rate of transition given in Mills S47
trans = indexes/10; %sets where the transition from fine to coarse occurs

%Grid Function given in Mills S47
for j = 1:indexes
    delta(j,1) = f + (c-f)/(1+exp(-r*(j-trans)));
end

%Create unreduced x values from grid function
x = 0;
for j = 2:length(delta)
    x(j,1) = x(j-1,1) + delta(j-1,1);
end

%Creates reduced semiconductor length from the previous grid function
lengthofsemi = x/x(end)*5e-4; %x variable ranges from 0-1000nm (1e-4 cm)
xred = lengthofsemi/debyeL; %reduces the x variable
xaxis = xred(1:2:end); %sets an xaxis with half the indexes (used for central
differences)
%"Grid Function" (Mills S46) used in central differences
wholeindex = 3:2:length(xred); %this gives the odd indexes from 3 to the end
of the reduced x length
for j = 1:1:length(wholeindex)
    delxhalf(j,1) = xred(wholeindex(j))-xred(wholeindex(j)-2); %this gives
"grid function" (Mills S46) for the i+1/2 indexes
    delxwhole(j,1) = xred(wholeindex(j)+1)-xred(wholeindex(j)-1); %this gives
"grid function" (Mills S46) for the i+1 indexes
end

%Sets initial guesses for potential, electron and hole concentrations
scV = (voltage+Vbi); %scV sets the applied voltage (but not including
electrocatalst voltage) which is a combination of built-in and applied
voltage
reducedvoltage = scV/(kb*T/q); %reduces voltage term
phi1 = Esol/(kbev*T); %sets interfacial potential to given Esol
phiend = Esol/(kbev*T)+reducedvoltage; %sets bulk potential

%Sets a algorithm for a generic potential profile
guessfactor = 2;
phi = 1./(exp((xaxis-0)/guessfactor)+1); %makes a initial curve for a generic
potential profile
phi = phi*2*(phi1-phiend)+(phiend-phi(end));

%Defining initial electron concentration
n1 = nsurf/d; %reduces election conc at surface (equilibrium)
nend = nbulk/d; %reduces electron conc at bulk
n = ((nend-n1)/xaxis(end))*xaxis+n1; %sets an initial guess to be linear
```

```
%Defining initial hole concentration
p1 = psurf/d; %reduces hole conc. at surface (equilibrium)
pend = pbulk/d; %reduces hole conc. at bulk
p = ((pend-p1)/xaxis(end))*xaxis+p1; %sets an initial guess to be linear

%Gummel Iteration
%This section of the code alternates between the continuity and Poisson's
%equation until the model converges
phichange = 1; %just used to start the while loop
nchange = 1;
pchange = 1;
conv = .00001; %this is a factor that says how many iterations are necessary
for convergence, this number that seems to work but can be changed
while nchange > conv || pchange > conv || phichange > conv

    %Calls the continuity equation solvers to solve for e and h profiles
    [n,nchange] =
eleccon(delxwhole,delxhalf,phi,p,n,Bred,Ired,alphared,nend,pend,n1,xaxis,knre
d,indexes);
    [p,pchange] =
holecon(delxwhole,delxhalf,phi,p,n,Bred,Ired,alphared,nend,pend,p1,xaxis,kpre
d,indexes);
    delta = 1; %sets an initial delta for the while loop of Poisson's solver
    oldphi = phi;
    figure(1)
    while max(abs(delta)) >= 0.001 %Poisson's will solve until the potential
stops changing
        [delta,phi,n,p] = Poissons(delxwhole,delxhalf,phi,n,p,indexes);
%calls the poisson equation solver
        %plots the potential profile for each iteration, which is useful to
see if your in the right voltage range, but can be turned off for speed
        plot(xaxis,phi)
        drawnow
    end
    phichange = max(abs(oldphi-phi))/max(abs(phi));
end

% The following equation from Mills et al. determine current from electron
% and hole concentrations
unredcurrentp = kpred*(p(1)-p1);
unredcurrentn = -knred*(n(1)-n1);

Current = unredcurrentp*nup*kb*T*d/debyeL + unredcurrentn*nun*kb*T*d/debyeL;
%unreduced current
CurrentmA = Current*1000; %converts A to mA
Vcat = -metallicVcat(CurrentmA,jocat); %calls function to solve for
electrocatalyst voltage
% The following lines solves for metallicVcat a different way, which is
% can useful in certain systems for convergence/speed
%Vcatred = metallicVcat2(n,p,jocat,phi,CurrentmA);
%Vcat = Vcatred*(kb*T/q);
z = 1;
% When you want to return individual electron and hole currents use the
% following lines
ElecC = unredcurrentn*nun*kb*T*d/debyeL;
```

```
HoleC = unredcurrentp*nup*kb*T*d/debyeL;
HoleCmA = HoleC*1000; %converts A to mA
ElecCmA = ElecC*1000;
% The total applied voltage is a combination of the electrocatalyst voltage
% and the voltage appied specifically to the semiconductor
TotalV = Vcat+voltage;


end

% Joseph Quinn, Nov 27, 2019
%
% CV
%
% Description: This function plots the modeled current voltage
% relationships
%
% Usage: CV(TotalV,Crange)
%
% Variables
%     TotalV = applied potential (V)
%     Crange = the current (mA)

function CV(TotalV,Crange)

plot(TotalV,Crange,'LineWidth',3)
hold on
set(gca,'fontsize',20)
title('Current Voltage Curve')
xlabel('Voltage (V)')
ylabel('Current (mA/cm^2)')
ylim([-10 (max(Crange)+5)]) %ylimits for anodic curves
%ylim([-60 (max(Crange)+5)]) %ylimits for cathodic curves

end
```

Bibliography

(1) US EPA, O. Inventory of U.S. Greenhouse Gas Emissions and Sinks: 1990-2017 https://www.epa.gov/ghgemissions/inventory-us-greenhouse-gas-emissions-and-sinks-1990-2017 (accessed Jul 17, 2019).

(2) Fred Joseck, Tien Nguyen,; Benjamin Klahr, and Amit Talapatra. *Current U.S. Hydrogen Production*; DOE Hydrogen and Fuel Cells Program Record 16015; Department of Energy, 2016.

(3) Buttler, A.; Spliethoff, H. Current Status of Water Electrolysis for Energy Storage, Grid Balancing and Sector Coupling via Power-to-Gas and Power-to-Liquids: A Review. *Renew. Sustain. Energy Rev.* **2018**, *82*, 2440–2454. https://doi.org/10.1016/j.rser.2017.09.003.

(4) Fuel Cell Technologies Office Multi-Year Research, Development, and Demonstration Plan. **2012**, 378.

(5) Kroposki, B.; Levene, J.; Harrison, K.; Sen, P. K.; Novachek, F. *Electrolysis: Information and Opportunities for Electric Power Utilities*; NREL/TP-581-40605, 892998; 2006; p NREL/TP-581-40605, 892998. https://doi.org/10.2172/892998.

(6) Carmo, M.; Fritz, D. L.; Mergel, J.; Stolten, D. A Comprehensive Review on PEM Water Electrolysis. *Int. J. Hydrog. Energy* **2013**, *38* (12), 4901–4934. https://doi.org/10.1016/j.ijhydene.2013.01.151.

(7) DOE Technical Targets for Hydrogen Production from Photoelectrochemical Water Splitting | Department of Energy https://www.energy.gov/eere/fuelcells/doe-technical-targets-hydrogen-production-photoelectrochemical-water-splitting (accessed Mar 28, 2018).

(8) Walter, M. G.; Warren, E. L.; McKone, J. R.; Boettcher, S. W.; Mi, Q.; Santori, E. A.; Lewis, N. S. Solar Water Splitting Cells. *Chem. Rev.* **2010**, *110* (11), 6446–6473. https://doi.org/10.1021/cr1002326.

(9) Grätzel, M. Photoelectrochemical Cells. *Nature* **2001**, *414* (6861), 338–344.

(10) Fujishima, A.; Honda, K. Electrochemical Photolysis of Water at a Semiconductor Electrode. *Nature* **1972**, *238* (5358), 37–38. https://doi.org/10.1038/238037a0.

(11) Sathre, R.; Greenblatt, J.; Walczak, K.; Sharp, I. D.; Stevens, J. C.; Iii, J. W. A.; Houle, F. A. Opportunities to Improve the Net Energy Performance of Photoelectrochemical Water-Splitting Technology. *Energy Environ. Sci.* **2016**. https://doi.org/10.1039/C5EE03040D.

(12) Lewis, N. S. Research Opportunities to Advance Solar Energy Utilization. *Science* **2016**, *351* (6271), aad1920. https://doi.org/10.1126/science.aad1920.

(13) A. Pinaud, B.; D. Benck, J.; C. Seitz, L.; J. Forman, A.; Chen, Z.; G. Deutsch, T.; D. James, B.; N. Baum, K.; N. Baum, G.; Ardo, S.; et al. Technical and Economic Feasibility of Centralized Facilities for Solar Hydrogen Production via Photocatalysis and Photoelectrochemistry. *Energy Environ. Sci.* **2013**, *6* (7), 1983–2002. https://doi.org/10.1039/C3EE40831K.

(14) James, B. D.; Baum, G. N.; Perez, J.; Baum, K. N. *Technoeconomic Analysis of Photoelectrochemical (PEC) Hydrogen Production*; 1218403; 2009. https://doi.org/10.2172/1218403.

(15) Shockley, W.; Queisser, H. J. Detailed Balance Limit of Efficiency of P-n Junction Solar Cells. *J. Appl. Phys.* **1961**, *32* (3), 510–519. https://doi.org/10.1063/1.1736034.

(16) Solar Spectral Irradiance: Air Mass 1.5 http://rredc.nrel.gov/solar/spectra/am1.5/ (accessed May 10, 2015).

(17) Tan, C. S.; Kemp, K. W.; Braun, M. R.; Meng, A. C.; Tan, W.; Chidsey, C. E. D.; Ma, W.; Moghadam, F.; McIntyre, P. C. >10% Solar-to-Hydrogen Efficiency Unassisted Water Splitting on ALD-Protected Silicon Heterojunction Solar Cells. *Sustain. Energy Fuels* **2019**, 10.1039.C9SE00110G. https://doi.org/10.1039/C9SE00110G.

(18) Seger, B.; Castelli, I. E.; Vesborg, P. C. K.; Jacobsen, K. W.; Hansen, O.; Chorkendorff, I. 2-Photon Tandem Device for Water Splitting: Comparing Photocathode First versus Photoanode First Designs. *Energy Environ. Sci.* **2014**, *7* (8), 2397–2413. https://doi.org/10.1039/C4EE01335B.

(19) Chakthranont, P.; Hellstern, T. R.; McEnaney, J. M.; Jaramillo, T. F. Design and Fabrication of a Precious Metal-Free Tandem Core–Shell P+n Si/W-Doped BiVO4 Photoanode for Unassisted Water Splitting. *Adv. Energy Mater.* **2017**, *7* (22), n/a-n/a. https://doi.org/10.1002/aenm.201701515.

(20) Haussener, S.; Hu, S.; Xiang, C.; Weber, A. Z.; Lewis, N. S. Simulations of the Irradiation and Temperature Dependence of the Efficiency of Tandem Photoelectrochemical Water-Splitting Systems. *Energy Environ. Sci.* **2013**, *6* (12), 3605–3618. https://doi.org/10.1039/C3EE41302K.

(21) Seitz, L. C.; Chen, Z.; Forman, A. J.; Pinaud, B. A.; Benck, J. D.; Jaramillo, T. F. Modeling Practical Performance Limits of Photoelectrochemical Water Splitting Based on

the Current State of Materials Research. *ChemSusChem* **2014**, *7* (5), 1372–1385. https://doi.org/10.1002/cssc.201301030.

(22) Chen, S.; Wang, L.-W. Thermodynamic Oxidation and Reduction Potentials of Photocatalytic Semiconductors in Aqueous Solution. *Chem. Mater.* **2012**, *24* (18), 3659–3666. https://doi.org/10.1021/cm302533s.

(23) Boettcher, S. W.; Spurgeon, J. M.; Putnam, M. C.; Warren, E. L.; Turner-Evans, D. B.; Kelzenberg, M. D.; Maiolo, J. R.; Atwater, H. A.; Lewis, N. S. Energy-Conversion Properties of Vapor-Liquid-Solid–Grown Silicon Wire-Array Photocathodes. *Science* **2010**, *327* (5962), 185–187. https://doi.org/10.1126/science.1180783.

(24) Chen, Y. W.; Prange, J. D.; Dühnen, S.; Park, Y.; Gunji, M.; Chidsey, C. E. D.; McIntyre, P. C. Atomic Layer-Deposited Tunnel Oxide Stabilizes Silicon Photoanodes for Water Oxidation. *Nat. Mater.* **2011**, *10* (7), 539–544. https://doi.org/10.1038/nmat3047.

(25) Ji, L.; McDaniel, M. D.; Wang, S.; Posadas, A. B.; Li, X.; Huang, H.; Lee, J. C.; Demkov, A. A.; Bard, A. J.; Ekerdt, J. G.; et al. A Silicon-Based Photocathode for Water Reduction with an Epitaxial $SrTiO_3$ Protection Layer and a Nanostructured Catalyst. *Nat. Nanotechnol.* **2014**, *10* (1), 84–90. https://doi.org/10.1038/nnano.2014.277.

(26) Dominey, R. N.; Lewis, N. S.; Bruce, J. A.; Bookbinder, D. C.; Wrighton, M. S. Improvement of Photoelectrochemical Hydrogen Generation by Surface Modification of P-Type Silicon Semiconductor Photocathodes. *J. Am. Chem. Soc.* **1982**, *104* (2), 467–482.

(27) Sun, K.; McDowell, M. T.; Nielander, A. C.; Hu, S.; Shaner, M. R.; Yang, F.; Brunschwig, B. S.; Lewis, N. S. Stable Solar-Driven Water Oxidation to O2(g) by Ni-Oxide-Coated Silicon Photoanodes. *J. Phys. Chem. Lett.* **2015**, *6* (4), 592–598. https://doi.org/10.1021/jz5026195.

(28) Hou, Y.; Abrams, B. L.; Vesborg, P. C. K.; Björketun, M. E.; Herbst, K.; Bech, L.; Setti, A. M.; Damsgaard, C. D.; Pedersen, T.; Hansen, O.; et al. Bioinspired Molecular Co-Catalysts Bonded to a Silicon Photocathode for Solar Hydrogen Evolution. *Nat. Mater.* **2011**, *10* (6), 434–438. https://doi.org/10.1038/nmat3008.

(29) Kim, T. W.; Choi, K.-S. Nanoporous BiVO4 Photoanodes with Dual-Layer Oxygen Evolution Catalysts for Solar Water Splitting. *Science* **2014**, *343* (6174), 990–994. https://doi.org/10.1126/science.1246913.

(30) Lee, D. K.; Choi, K.-S. Enhancing Long-Term Photostability of BiVO 4 Photoanodes for Solar Water Splitting by Tuning Electrolyte Composition. *Nat. Energy* **2018**, *3* (1), 53–60. https://doi.org/10.1038/s41560-017-0057-0.

(31) Singh, A. P.; Kodan, N.; Mehta, B. R.; Held, A.; Mayrhofer, L.; Moseler, M. Band Edge Engineering in BiVO4/TiO2 Heterostructure: Enhanced Photoelectrochemical

Performance through Improved Charge Transfer. *ACS Catal.* **2016**, *6* (8), 5311–5318. https://doi.org/10.1021/acscatal.6b00956.

(32) Cesar, I.; Sivula, K.; Kay, A.; Zboril, R.; Grätzel, M. Influence of Feature Size, Film Thickness, and Silicon Doping on the Performance of Nanostructured Hematite Photoanodes for Solar Water Splitting. *J. Phys. Chem. C* **2009**, *113* (2), 772–782. https://doi.org/10.1021/jp809060p.

(33) Qiu, J.; Hajibabaei, H.; Nellist, M. R.; Laskowski, F. A. L.; Hamann, T. W.; Boettcher, S. W. Direct in Situ Measurement of Charge Transfer Processes During Photoelectrochemical Water Oxidation on Catalyzed Hematite. *ACS Cent. Sci.* **2017**, *3* (9), 1015–1025. https://doi.org/10.1021/acscentsci.7b00310.

(34) Hu, S.; Shaner, M. R.; Beardslee, J. A.; Lichterman, M.; Brunschwig, B. S.; Lewis, N. S. Amorphous TiO2 Coatings Stabilize Si, GaAs, and GaP Photoanodes for Efficient Water Oxidation. *Science* **2014**, *344* (6187), 1005–1009. https://doi.org/10.1126/science.1251428.

(35) Pan, L.; Kim, J. H.; Mayer, M. T.; Son, M.-K.; Ummadisingu, A.; Lee, J. S.; Hagfeldt, A.; Luo, J.; Grätzel, M. Boosting the Performance of Cu2O Photocathodes for Unassisted Solar Water Splitting Devices. *Nat. Catal.* **2018**, *1* (6), 412–420. https://doi.org/10.1038/s41929-018-0077-6.

(36) Bagal, I. V.; Chodankar, N. R.; Hassan, M. A.; Waseem, A.; Johar, M. A.; Kim, D.-H.; Ryu, S.-W. Cu2O as an Emerging Photocathode for Solar Water Splitting - A Status Review. *Int. J. Hydrog. Energy* **2019**, *44* (39), 21351–21378. https://doi.org/10.1016/j.ijhydene.2019.06.184.

(37) Hu, S.; Lewis, N. S.; Ager, J. W.; Yang, J.; McKone, J. R.; Strandwitz, N. C. Thin-Film Materials for the Protection of Semiconducting Photoelectrodes in Solar-Fuel Generators. *J. Phys. Chem. C* **2015**, *119* (43), 24201–24228. https://doi.org/10.1021/acs.jpcc.5b05976.

(38) Scheuermann, A. G.; McIntyre, P. C. Atomic Layer Deposited Corrosion Protection: A Path to Stable and Efficient Photoelectrochemical Cells. *J. Phys. Chem. Lett.* **2016**, *7* (14), 2867–2878. https://doi.org/10.1021/acs.jpclett.6b00631.

(39) Bae, D.; Seger, B.; Vesborg, P. C. K.; Hansen, O.; Chorkendorff, I. Strategies for Stable Water Splitting via Protected Photoelectrodes. *Chem. Soc. Rev.* **2017**, *46* (7), 1933–1954. https://doi.org/10.1039/C6CS00918B.

(40) Mei, B.; Pedersen, T.; Malacrida, P.; Bae, D.; Frydendal, R.; Hansen, O.; Vesborg, P. C. K.; Seger, B.; Chorkendorff, I. Crystalline TiO 2 : A Generic and Effective Electron-Conducting Protection Layer for Photoanodes and -Cathodes. *J. Phys. Chem. C* **2015**, *119* (27), 15019–15027. https://doi.org/10.1021/acs.jpcc.5b04407.

(41) Seger, B.; Pedersen, T.; Laursen, A. B.; Vesborg, P. C. K.; Hansen, O.; Chorkendorff, I. Using TiO2 as a Conductive Protective Layer for Photocathodic H2 Evolution. *J. Am. Chem. Soc.* **2013**, *135* (3), 1057–1064. https://doi.org/10.1021/ja309523t.

(42) Fan, R.; Dong, W.; Fang, L.; Zheng, F.; Shen, M. More than 10% Efficiency and One-Week Stability of Si Photocathodes for Water Splitting by Manipulating the Loading of the Pt Catalyst and TiO 2 Protective Layer. *J. Mater. Chem. A* **2017**, *5* (35), 18744–18751. https://doi.org/10.1039/C7TA04986B.

(43) Oh, S.; Oh, J. High Performance and Stability of Micropatterned Oxide-Passivated Photoanodes with Local Catalysts for Photoelectrochemical Water Splitting. *J. Phys. Chem. C* **2016**, *120* (1), 133–141. https://doi.org/10.1021/acs.jpcc.5b10859.

(44) Guo, B.; Batool, A.; Xie, G.; Boddula, R.; Tian, L.; Jan, S. U.; Gong, J. R. Facile Integration between Si and Catalyst for High-Performance Photoanodes by a Multifunctional Bridging Layer. *Nano Lett.* **2018**, *18* (2), 1516–1521. https://doi.org/10.1021/acs.nanolett.7b05314.

(45) Oh, S.; Song, H.; Oh, J. An Optically and Electrochemically Decoupled Monolithic Photoelectrochemical Cell for High-Performance Solar-Driven Water Splitting. *Nano Lett.* **2017**, *17* (9), 5416–5422. https://doi.org/10.1021/acs.nanolett.7b02023.

(46) Sun, K.; Park, N.; Sun, Z.; Zhou, J.; Wang, J.; Pang, X.; Shen, S.; Young Noh, S.; Jing, Y.; Jin, S.; et al. Nickel Oxide Functionalized Silicon for Efficient Photo-Oxidation of Water. *Energy Environ. Sci.* **2012**, *5* (7), 7872–7877. https://doi.org/10.1039/C2EE21708B.

(47) Jung, J.-Y.; Yu, J.-Y.; Shinde, S. S.; Kim, S.-H.; Kim, D.-H.; Lin, C.; Wehrspohn, R. B.; Lee, J.-H. Remarkable Improvements in the Performance and Stability of Si Photoanodes Adopting Nanocrystalline NiOx Electrocatalyst and Stoichiometric SiO2 Protection. *Appl. Surf. Sci.* **2019**, *493*, 1150–1158. https://doi.org/10.1016/j.apsusc.2019.07.128.

(48) McDowell, M. T.; Lichterman, M. F.; Carim, A. I.; Liu, R.; Hu, S.; Brunschwig, B. S.; Lewis, N. S. The Influence of Structure and Processing on the Behavior of TiO2 Protective Layers for Stabilization of N-Si/TiO2/Ni Photoanodes for Water Oxidation. *ACS Appl. Mater. Interfaces* **2015**, *7* (28), 15189–15199. https://doi.org/10.1021/acsami.5b00379.

(49) Lichterman, M. F.; Sun, K.; Hu, S.; Zhou, X.; McDowell, M. T.; Shaner, M. R.; Richter, M. H.; Crumlin, E. J.; Carim, A. I.; Saadi, F. H.; et al. Protection of Inorganic Semiconductors for Sustained, Efficient Photoelectrochemical Water Oxidation. *Catal. Today* **2016**, *262*, 11–23. https://doi.org/10.1016/j.cattod.2015.08.017.

(50) Scheuermann, A. G.; Lawrence, J. P.; Kemp, K. W.; Ito, T.; Walsh, A.; Chidsey, C. E. D.; Hurley, P. K.; McIntyre, P. C. Design Principles for Maximizing Photovoltage in Metal-

Oxide-Protected Water-Splitting Photoanodes. *Nat. Mater.* **2016**, *15* (1), 99–105. https://doi.org/10.1038/nmat4451.

(51) Cai, Q.; Hong, W.; Jian, C.; Li, J.; Liu, W. Insulator Layer Engineering toward Stable Si Photoanode for Efficient Water Oxidation. *ACS Catal.* **2018**, *8* (10), 9238–9244. https://doi.org/10.1021/acscatal.8b01398.

(52) Ji, L.; Hsu, H.-Y.; Li, X.; Huang, K.; Zhang, Y.; Lee, J. C.; Bard, A. J.; Yu, E. T. Localized Dielectric Breakdown and Antireflection Coating in Metal–Oxide–Semiconductor Photoelectrodes. *Nat. Mater.* **2017**, *16* (1), 127–131. https://doi.org/10.1038/nmat4801.

(53) Tilley, S. D. Recent Advances and Emerging Trends in Photo-Electrochemical Solar Energy Conversion. *Adv. Energy Mater.* **2019**, *9* (2), 1802877. https://doi.org/10.1002/aenm.201802877.

(54) Loget, G. Water Oxidation with Inhomogeneous Metal-Silicon Interfaces. *Curr. Opin. Colloid Interface Sci.* **2019**, *39*, 40–50. https://doi.org/10.1016/j.cocis.2019.01.001.

(55) Park, M.-J.; Jung, J.-Y.; Shin, S.-M.; Song, J.-W.; Nam, Y.-H.; Kim, D.-H.; Lee, J.-H. Photoelectrochemical Oxygen Evolution Improved by a Thin Al2O3 Interlayer in a NiOx/n-Si Photoanode. *Thin Solid Films* **2016**, *599*, 54–58. https://doi.org/10.1016/j.tsf.2015.12.062.

(56) Digdaya, I. A.; Adhyaksa, G. W. P.; Trześniewski, B. J.; Garnett, E. C.; Smith, W. A. Interfacial Engineering of Metal-Insulator-Semiconductor Junctions for Efficient and Stable Photoelectrochemical Water Oxidation. *Nat. Commun.* **2017**, *8*, 15968. https://doi.org/10.1038/ncomms15968.

(57) G. Scheuermann, A.; W. Kemp, K.; Tang, K.; Q. Lu, D.; F. Satterthwaite, P.; Ito, T.; D. Chidsey, C. E.; C. McIntyre, P. Conductance and Capacitance of Bilayer Protective Oxides for Silicon Water Splitting Anodes. *Energy Environ. Sci.* **2016**, *9* (2), 504–516. https://doi.org/10.1039/C5EE02484F.

(58) Digdaya, I. A.; Trześniewski, B. J.; Adhyaksa, G. W. P.; Garnett, E. C.; Smith, W. A. General Considerations for Improving Photovoltage in Metal-Insulator-Semicondutor Photoanodes http://pubs.acs.org/doi/abs/10.1021/acs.jpcc.7b11747 (accessed Feb 27, 2018). https://doi.org/10.1021/acs.jpcc.7b11747.

(59) Hu, S.; Shaner, M. R.; Beardslee, J. A.; Lichterman, M.; Brunschwig, B. S.; Lewis, N. S. Amorphous TiO2 Coatings Stabilize Si, GaAs, and GaP Photoanodes for Efficient Water Oxidation. *Science* **2014**, *344* (6187), 1005–1009. https://doi.org/10.1126/science.1251428.

(60) Scheuermann, A. G.; Lawrence, J. P.; Meng, A. C.; Tang, K.; Hendricks, O. L.; Chidsey, C. E. D.; McIntyre, P. C. Titanium Oxide Crystallization and Interface Defect Passivation

for High Performance Insulator-Protected Schottky Junction MIS Photoanodes. *ACS Appl. Mater. Interfaces* **2016**, *8* (23), 14596–14603. https://doi.org/10.1021/acsami.6b03688.

(61) McDowell, M. T.; Lichterman, M. F.; Carim, A. I.; Liu, R.; Hu, S.; Brunschwig, B. S.; Lewis, N. S. The Influence of Structure and Processing on the Behavior of TiO2 Protective Layers for Stabilization of N-Si/TiO2/Ni Photoanodes for Water Oxidation. *ACS Appl. Mater. Interfaces* **2015**, *7* (28), 15189–15199. https://doi.org/10.1021/acsami.5b00379.

(62) Quinn, J.; Hemmerling, J.; Linic, S. Guidelines for Optimizing the Performance of Metal–Insulator–Semiconductor (MIS) Photoelectrocatalytic Systems by Tuning the Insulator Thickness. *ACS Energy Lett.* **2019**, 2632–2638. https://doi.org/10.1021/acsenergylett.9b01609.

(63) Quinn, J.; Hemmerling, J.; Linic, S. Maximizing Solar Water Splitting Performance by Nanoscopic Control of the Charge Carrier Fluxes across Semiconductor–Electrocatalyst Junctions. *ACS Catal.* **2018**, 8545–8552. https://doi.org/10.1021/acscatal.8b01929.

(64) Singh, R.; Green, M. A.; Rajkanan, K. Review of Conductor-Insulator-Semiconductor (CIS) Solar Cells. *Sol. Cells* **1981**, *3* (2), 95–148. https://doi.org/10.1016/0379-6787(81)90088-0.

(65) Card, H. C.; Rhoderick, E. H. Studies of Tunnel MOS Diodes I. Interface Effects in Silicon Schottky Diodes. *J. Phys. Appl. Phys.* **1971**, *4* (10), 1589. https://doi.org/10.1088/0022-3727/4/10/319.

(66) Olsen, L. C. Model Calculations for Metal-Insulator-Semiconductor Solar Cells. *Solid-State Electron.* **1977**, *20* (9), 741–751. https://doi.org/10.1016/0038-1101(77)90002-8.

(67) Godfrey, R. B.; Green, M. A. 655 MV Open-circuit Voltage, 17.6% Efficient Silicon MIS Solar Cells. *Appl. Phys. Lett.* **1979**, *34* (11), 790–793. https://doi.org/10.1063/1.90646.

(68) Sze, S. M.; Ng, K. K. *Physics of Semiconductor Devices*, 3rd ed.; Wiley-Interscience: Hoboken, N.J, 2007.

(69) Zhang, Z.; Yates, J. T. Band Bending in Semiconductors: Chemical and Physical Consequences at Surfaces and Interfaces. *Chem. Rev.* **2012**, *112* (10), 5520–5551. https://doi.org/10.1021/cr3000626.

(70) Nozik, A. J.; Memming, R. Physical Chemistry of Semiconductor-Liquid Interfaces. *J. Phys. Chem.* **1996**, *100* (31), 13061–13078.

(71) Rossi, R. C.; Lewis, N. S. Investigation of the Size-Scaling Behavior of Spatially Nonuniform Barrier Height Contacts to Semiconductor Surfaces Using Ordered Nanometer-Scale Nickel Arrays on Silicon Electrodes. *J. Phys. Chem. B* **2001**, *105* (49), 12303–12318. https://doi.org/10.1021/jp011861c.

(72) Hernley, P. A.; Chavez, S. A.; Quinn, J. P.; Linic, S. Engineering the Optical and Catalytic Properties of Co-Catalyst/Semiconductor Photocatalysts. *ACS Photonics* **2017**, *4* (4), 979–985. https://doi.org/10.1021/acsphotonics.7b00047.

(73) McKone, J. R.; Warren, E. L.; Bierman, M. J.; Boettcher, S. W.; Brunschwig, B. S.; Lewis, N. S.; Gray, H. B. Evaluation of Pt, Ni, and Ni–Mo Electrocatalysts for Hydrogen Evolution on Crystalline Si Electrodes. *Energy Environ. Sci.* **2011**, *4* (9), 3573–3583. https://doi.org/10.1039/C1EE01488A.

(74) Kye, J.; Shin, M.; Lim, B.; Jang, J.-W.; Oh, I.; Hwang, S. Platinum Monolayer Electrocatalyst on Gold Nanostructures on Silicon for Photoelectrochemical Hydrogen Evolution. *ACS Nano* **2013**, *7* (7), 6017–6023. https://doi.org/10.1021/nn401720x.

(75) Nørskov, J. K.; Bligaard, T.; Logadottir, A.; Kitchin, J. R.; Chen, J. G.; Pandelov, S.; Stimming, U. Trends in the Exchange Current for Hydrogen Evolution. *J. Electrochem. Soc.* **2005**, *152* (3), J23–J26. https://doi.org/10.1149/1.1856988.

(76) Louie, M. W.; Bell, A. T. An Investigation of Thin-Film Ni–Fe Oxide Catalysts for the Electrochemical Evolution of Oxygen. *J. Am. Chem. Soc.* **2013**, *135* (33), 12329–12337. https://doi.org/10.1021/ja405351s.

(77) Qiu, J.; Hajibabaei, H.; Nellist, M. R.; Laskowski, F. A. L.; Oener, S. Z.; Hamann, T. W.; Boettcher, S. W. Catalyst Deposition on Photoanodes: The Roles of Intrinsic Catalytic Activity, Catalyst Electrical Conductivity, and Semiconductor Morphology. *ACS Energy Lett.* **2018**, *3* (4), 961–969. https://doi.org/10.1021/acsenergylett.8b00336.

(78) G. Scheuermann, A.; D. Prange, J.; Gunji, M.; D. Chidsey, C. E.; C. McIntyre, P. Effects of Catalyst Material and Atomic Layer Deposited TiO 2 Oxide Thickness on the Water Oxidation Performance of Metal–Insulator–Silicon Anodes. *Energy Environ. Sci.* **2013**, *6* (8), 2487–2496. https://doi.org/10.1039/C3EE41178H.

(79) Enman, L. J.; Burke, M. S.; Batchellor, A. S.; Boettcher, S. W. Effects of Intentionally Incorporated Metal Cations on the Oxygen Evolution Electrocatalytic Activity of Nickel (Oxy)Hydroxide in Alkaline Media. *ACS Catal.* **2016**, *6* (4), 2416–2423. https://doi.org/10.1021/acscatal.5b02924.

(80) Friebel, D.; Louie, M. W.; Bajdich, M.; Sanwald, K. E.; Cai, Y.; Wise, A. M.; Cheng, M.-J.; Sokaras, D.; Weng, T.-C.; Alonso-Mori, R.; et al. Identification of Highly Active Fe Sites in (Ni,Fe)OOH for Electrocatalytic Water Splitting. *J. Am. Chem. Soc.* **2015**, *137* (3), 1305–1313. https://doi.org/10.1021/ja511559d.

(81) Trotochaud, L.; Young, S. L.; Ranney, J. K.; Boettcher, S. W. Nickel–Iron Oxyhydroxide Oxygen-Evolution Electrocatalysts: The Role of Intentional and Incidental Iron Incorporation. *J. Am. Chem. Soc.* **2014**, *136* (18), 6744–6753. https://doi.org/10.1021/ja502379c.

(82) Burke, M. S.; Enman, L. J.; Batchellor, A. S.; Zou, S.; Boettcher, S. W. Oxygen Evolution Reaction Electrocatalysis on Transition Metal Oxides and (Oxy)Hydroxides: Activity Trends and Design Principles. *Chem. Mater.* **2015**. https://doi.org/10.1021/acs.chemmater.5b03148.

(83) Chen, Y.; Hu, S.; Xiang, C.; Lewis, N. S. A Sensitivity Analysis to Assess the Relative Importance of Improvements in Electrocatalysts, Light Absorbers, and System Geometry on the Efficiency of Solar-Fuels Generators. *Energy Environ. Sci.* **2015**, *8* (3), 876–886. https://doi.org/10.1039/C4EE02314E.

(84) Huang, Z.; McKone, J. R.; Xiang, C.; Grimm, R. L.; Warren, E. L.; Spurgeon, J. M.; Lewerenz, H.-J.; Brunschwig, B. S.; Lewis, N. S. Comparison between the Measured and Modeled Hydrogen-Evolution Activity of Ni- or Pt-Coated Silicon Photocathodes. *Int. J. Hydrog. Energy* **2014**, *39* (28), 16220–16226. https://doi.org/10.1016/j.ijhydene.2013.12.162.

(85) Cowley, A. M.; Sze, S. M. Surface States and Barrier Height of Metal-Semiconductor Systems. *J. Appl. Phys.* **1965**, *36* (10), 3212–3220.

(86) Rhoderick, E. H. Metal-Semiconductor Contacts. *IEE PROC* **1982**, *129* (1), 14.

(87) Dingemans, G.; Kessels, W. M. M. Status and Prospects of Al 2 O 3 -Based Surface Passivation Schemes for Silicon Solar Cells. *J. Vac. Sci. Technol. Vac. Surf. Films* **2012**, *30* (4), 040802. https://doi.org/10.1116/1.4728205.

(88) Simon, D. K.; Jordan, P. M.; Mikolajick, T.; Dirnstorfer, I. On the Control of the Fixed Charge Densities in Al 2 O 3 -Based Silicon Surface Passivation Schemes. *ACS Appl. Mater. Interfaces* **2015**, *7* (51), 28215–28222. https://doi.org/10.1021/acsami.5b06606.

(89) Plakhotnyuk, M. M.; Schüler, N.; Shkodin, E.; Vijayan, R. A.; Masilamani, S.; Varadharajaperumal, M.; Crovetto, A.; Hansen, O. Surface Passivation and Carrier Selectivity of the Thermal-Atomic-Layer-Deposited TiO2 on Crystalline Silicon. *Jpn. J. Appl. Phys.* **2017**, *56* (8S2), 08MA11. https://doi.org/10.7567/JJAP.56.08MA11.

(90) Mills, T. J.; Laskowski, F. A. L.; Dette, C.; Nellist, M. R.; Lin, F.; Boettcher, S. W. The Role of Surface States in Electrocatalyst-Modified Semiconductor Photoelectrodes: Theory and Simulations. *ArXiv170703112 Cond-Mat Physicsphysics* **2017**.

(91) Choi, M. J.; Jung, J.-Y.; Park, M.-J.; Song, J.-W.; Lee, J.-H.; Bang, J. H. Long-Term Durable Silicon Photocathode Protected by a Thin Al2O3/SiOx Layer for Photoelectrochemical Hydrogen Evolution. *J. Mater. Chem. A* **2014**, *2* (9), 2928–2933. https://doi.org/10.1039/C3TA14443G.

(92) Lin, F.; Boettcher, S. W. Adaptive Semiconductor/Electrocatalyst Junctions in Water-Splitting Photoanodes. *Nat. Mater.* **2014**, *13* (1), 81–86. https://doi.org/10.1038/nmat3811.

(93) Mills, T. J.; Lin, F.; Boettcher, S. W. Theory and Simulations of Electrocatalyst-Coated Semiconductor Electrodes for Solar Water Splitting. *Phys. Rev. Lett.* **2014**, *112* (14), 148304. https://doi.org/10.1103/PhysRevLett.112.148304.

(94) Lin, F.; Bachman, B. F.; Boettcher, S. W. Impact of Electrocatalyst Activity and Ion Permeability on Water-Splitting Photoanodes. *J. Phys. Chem. Lett.* **2015**, 2427–2433. https://doi.org/10.1021/acs.jpclett.5b00904.

(95) Seitz, L. C.; Chen, Z.; Forman, A. J.; Pinaud, B. A.; Benck, J. D.; Jaramillo, T. F. Modeling Practical Performance Limits of Photoelectrochemical Water Splitting Based on the Current State of Materials Research. *ChemSusChem* **2014**, *7* (5), 1372–1385. https://doi.org/10.1002/cssc.201301030.

(96) Ingram, D. B.; Linic, S. Water Splitting on Composite Plasmonic-Metal/Semiconductor Photoelectrodes: Evidence for Selective Plasmon-Induced Formation of Charge Carriers near the Semiconductor Surface. *J. Am. Chem. Soc.* **2011**, *133* (14), 5202–5205. https://doi.org/10.1021/ja200086g.

(97) Christopher, P.; Ingram, D. B.; Linic, S. Enhancing Photochemical Activity of Semiconductor Nanoparticles with Optically Active Ag Nanostructures: Photochemistry Mediated by Ag Surface Plasmons. *J. Phys. Chem. C* **2010**, *114* (19), 9173–9177. https://doi.org/10.1021/jp101633u.

(98) Ingram, D. B.; Christopher, P.; Bauer, J. L.; Linic, S. Predictive Model for the Design of Plasmonic Metal/Semiconductor Composite Photocatalysts. *ACS Catal.* **2011**, *1* (10), 1441–1447. https://doi.org/10.1021/cs200320h.

(99) Strayer, R. W.; Mackie, W.; Swanson, L. W. Work Function Measurements by the Field Emission Retarding Potential Method. *Surf. Sci.* **1973**, *34* (2), 225–248. https://doi.org/10.1016/0039-6028(73)90117-9.

(100) Kenney, M. J.; Gong, M.; Li, Y.; Wu, J. Z.; Feng, J.; Lanza, M.; Dai, H. High-Performance Silicon Photoanodes Passivated with Ultrathin Nickel Films for Water Oxidation. *Science* **2013**, *342* (6160), 836–840. https://doi.org/10.1126/science.1241327.

(101) L. Laskowski, F. A.; R. Nellist, M.; Venkatkarthick, R.; W. Boettcher, S. Junction Behavior of N-Si Photoanodes Protected by Thin Ni Elucidated from Dual Working Electrode Photoelectrochemistry. *Energy Environ. Sci.* **2017**, *10* (2), 570–579. https://doi.org/10.1039/C6EE03505A.

(102) Eastman, D. E. Photoelectric Work Functions of Transition, Rare-Earth, and Noble Metals. *Phys. Rev. B* **1970**, *2* (1), 1–2. https://doi.org/10.1103/PhysRevB.2.1.

(103) Esposito, D. V.; Levin, I.; Moffat, T. P.; Talin, A. A. H2 Evolution at Si-Based Metal–Insulator–Semiconductor Photoelectrodes Enhanced by Inversion Channel Charge

Collection and H Spillover. *Nat. Mater.* **2013**, *12* (6), 562–568. https://doi.org/10.1038/nmat3626.

(104) Wilson, S. S.; Bosco, J. P.; Tolstova, Y.; Scanlon, D. O.; Watson, G. W.; Atwater, H. A. Interface Stoichiometry Control to Improve Device Voltage and Modify Band Alignment in ZnO/Cu2O Heterojunction Solar Cells. *Energy Environ. Sci.* **2014**, *7* (11), 3606–3610. https://doi.org/10.1039/C4EE01956C.

(105) Ritala, M.; Leskelä, M. Atomic Layer Epitaxy - a Valuable Tool for Nanotechnology? *Nanotechnology* **1999**, *10* (1), 19. https://doi.org/10.1088/0957-4484/10/1/005.

(106) Marichy, C.; Bechelany, M.; Pinna, N. Atomic Layer Deposition of Nanostructured Materials for Energy and Environmental Applications. *Adv. Mater. 24* (8), 1017–1032. https://doi.org/10.1002/adma.201104129.

(107) Laursen, S.; Linic, S. Strong Chemical Interactions Between Au and Off-Stoichiometric Defects on TiO2 as a Possible Source of Chemical Activity of Nanosized Au Supported on the Oxide. *J. Phys. Chem. C* **2009**, *113* (16), 6689–6693. https://doi.org/10.1021/jp810603u.

(108) Mukherjee, J.; Linic, S. First-Principles Investigations of Electrochemical Oxidation of Hydrogen at Solid Oxide Fuel Cell Operating Conditions. *J. Electrochem. Soc.* **2007**, *154* (9), B919–B924. https://doi.org/10.1149/1.2752983.

(109) Ingram, D. B.; Linic, S. First-Principles Analysis of the Activity of Transition and Noble Metals in the Direct Utilization of Hydrocarbon Fuels at Solid Oxide Fuel Cell Operating Conditions. *J. Electrochem. Soc.* **2009**, *156* (12), B1457–B1465. https://doi.org/10.1149/1.3240101.

(110) Pourbaix, M. *Atlas of Electrochemical Equilibria in Aqueous Solutions*, 2nd edition.; National Association of Corrosion: Houston, Tex., 1974.

(111) Zhu, W. J.; Ma, T.-P.; Tamagawa, T.; Kim, J.; Di, Y. Current Transport in Metal/Hafnium Oxide/Silicon Structure. *IEEE Electron Device Lett.* **2002**, *23* (2), 97–99. https://doi.org/10.1109/55.981318.

(112) Digdaya, I. A.; Trześniewski, B. J.; Adhyaksa, G. W. P.; Garnett, E. C.; Smith, W. A. General Considerations for Improving Photovoltage in Metal–Insulator–Semiconductor Photoanodes. *J. Phys. Chem. C* **2018**, *122* (10), 5462–5471. https://doi.org/10.1021/acs.jpcc.7b11747.

(113) Eastment, R. M.; Mee, C. H. B. Work Function Measurements on (100), (110) and (111) Surfaces of Aluminium. *J. Phys. F Met. Phys.* **1973**, *3* (9), 1738–1745. https://doi.org/10.1088/0305-4608/3/9/016.

(114) Eastman, D. E. Photoelectric Work Functions of Transition, Rare-Earth, and Noble Metals. *Phys. Rev. B* **1970**, *2* (1), 1–2. https://doi.org/10.1103/PhysRevB.2.1.

(115) Wang, Y.; Yu, Z.; Zahid, F.; Liu, L.; Zhu, Y.; Wang, J.; Guo, H. Direct Tunneling through High- κ Amorphous HfO_2 : Effects of Chemical Modification. *J. Appl. Phys.* **2014**, *116* (2), 023703. https://doi.org/10.1063/1.4890010.

(116) Newman, N.; van Schilfgaarde, M.; Kendelwicz, T.; Williams, M. D.; Spicer, W. E. Electrical Study of Schottky Barriers on Atomically Clean GaAs(110) Surfaces. *Phys. Rev. B* **1986**, *33* (2), 1146–1159. https://doi.org/10.1103/PhysRevB.33.1146.

(117) Pan, L.; Kim, J. H.; Mayer, M. T.; Son, M.-K.; Ummadisingu, A.; Lee, J. S.; Hagfeldt, A.; Luo, J.; Grätzel, M. Boosting the Performance of Cu 2 O Photocathodes for Unassisted Solar Water Splitting Devices. *Nat. Catal.* **2018**, 1. https://doi.org/10.1038/s41929-018-0077-6.

(118) Luo, J.; Steier, L.; Son, M.-K.; Schreier, M.; Mayer, M. T.; Grätzel, M. Cu 2 O Nanowire Photocathodes for Efficient and Durable Solar Water Splitting. *Nano Lett.* **2016**, *16* (3), 1848–1857. https://doi.org/10.1021/acs.nanolett.5b04929.

(119) Tolstova, Y.; Omelchenko, S. T.; Blackwell, R. E.; Shing, A. M.; Atwater, H. A. Polycrystalline Cu 2 O Photovoltaic Devices Incorporating Zn(O,S) Window Layers. *Sol. Energy Mater. Sol. Cells* **2017**, *160*, 340–345. https://doi.org/10.1016/j.solmat.2016.10.049.

(120) Hernley, P. A.; Linic, S. Modeling the Impact of Metallic Plasmonic Resonators on the Solar Conversion Efficiencies of Semiconductor Photoelectrodes: When Does Introducing Buried Plasmonic Nanostructures Make Sense? *J. Phys. Chem. C* **2018**, *122* (42), 24279–24286. https://doi.org/10.1021/acs.jpcc.8b07214.

(121) Warren, E. L.; Atwater, H. A.; Lewis, N. S. Silicon Microwire Arrays for Solar Energy-Conversion Applications. *J. Phys. Chem. C* **2014**, *118* (2), 747–759. https://doi.org/10.1021/jp406280x.

(122) Boettcher, S. W.; Warren, E. L.; Putnam, M. C.; Santori, E. A.; Turner-Evans, D.; Kelzenberg, M. D.; Walter, M. G.; McKone, J. R.; Brunschwig, B. S.; Atwater, H. A.; et al. Photoelectrochemical Hydrogen Evolution Using Si Microwire Arrays. *J. Am. Chem. Soc.* **2011**, *133* (5), 1216–1219. https://doi.org/10.1021/ja108801m.

(123) Oh, J.; Deutsch, T. G.; Yuan, H.-C.; Branz, H. M. Nanoporous Black Silicon Photocathode for H2 Production by Photoelectrochemical Water Splitting. *Energy Environ. Sci.* **2011**, *4* (5), 1690–1694. https://doi.org/10.1039/C1EE01124C.

(124) Chen, C.-J.; Chen, M.-G.; Chen, C. K.; Wu, P. C.; Chen, P.-T.; Basu, M.; Hu, S.-F.; Tsai, D. P.; Liu, R.-S. Ag–Si Artificial Microflowers for Plasmon-Enhanced Solar Water Splitting. *Chem. Commun.* **2014**, *51* (3), 549–552. https://doi.org/10.1039/C4CC07935C.